DIPLOMARBEIT

Purely electrical power stabilization of photovoltaic technologies

zur Erlangung des akademischen Grades

Diplom-Ingenieurin

im Rahmen des Studiums

Physikalische Energie- und Messtechnik

eingereicht von

Nicole Ulrike Zechner, BSc

Matrikelnummer 01125645

ausgeführt am Institut für Angewandte Physik der Fakultät für Physik der Technischen Universität Wien

in Zusammenarbeit mit dem Austrian Institute of Technology Energy Department Photovoltaic Systems

Betreuung

Betreuer: Mag. Dr. Marcus **RENNHOFER**

Begutachter: Ao.Univ.Prof. Dipl.-Ing. Dr.techn. Martin **GRÖSCHL**

Wien, 31.08.2021

(Unterschrift Verfasserin) (Unterschrift Betreuer)

Abstract

With the increasing world energy demand, renewable power sources like photovoltaics will become more and more important for our future. The accurate estimation of output power of photovoltaic modules is crucial for the correct sizing of photovoltaic power plants.
One approach to improve pre-standardization methods in the field of thin film photovoltaic devices is dark bias stabilization. While the idea has been out for decades, there has been little research in the recent past. For this thesis, I made a literature research in dark bias stabilization, followed by dark biasing experiments on photovoltaic modules.
In accordance with the Pearl-TF PV report that sparked this thesis, I found favorable results in dark biasing of CZTS minimodules with biasing currents smaller than the short circuit current of the biased module.
For the full scale CIGS and mono-c-Si modules the results were less promising, most likely due to bad choice of bias parameters.

It can be concluded that dark bias stabilization may in fact be a valid, more economic alternative to more traditional stabilization techniques and should be investigated further in the future.

Zusammenfassung

Mit dem steigenden weltweiten Energiebedarf werden erneuerbare Energieträger wie Photovoltaik in Zukunft immer mehr an Bedeutung gewinnen. Die präzise Schätzung der Ausgangsleistung von Photovoltaikmodulen ist wesentlich für die korrekte Bemessung von Photovoltaikanlagen.
Eine Herangehensweise um die Prä-Standardisierung von Dünnschicht-Photovoltaikmodulen zu verbessern, ist die Dunkelstrom-Stabilisierung (dark bias stabilization). Obwohl es die Grundidee schon seit Jahrzehnten gibt, ist in der näheren Vergangenheit wenig zu dem Thema geforscht worden. Im Zuge dieser Diplomarbeit habe ich zunächst eine Literaturrecherche zum Thema Dunkelstrom-Stabilisierung durchgeführt, gefolgt von Dunkelstrom-Stabilisierungs-Experimenten an verschiedenen Photovoltaikmodultypen.
Nach dem Pearl-TF PV Report, der den Ausschlag für den Beginn dieser Arbeit gab, fand ich positive Ergebnisse für Dunkelstrom-Stabilisierung von CZTS Minimodulen unter der Verwendung von Vorströmen kleiner als die Kurzschlussströme der betrachteten Module. Für die großen CIGS und mono-c-Si Module waren die Ergebnisse weniger vielversprechend, vermutlich aufgrund schlecht gewählter Parameter für die Stabilisierung.

Zusammenfassend wurde beobachtet, dass Dunkelstrom-Stabilisierung tatsächlich eine gültige, kostengünstigere Alternative zu den traditionellen Stabilisierungsmethoden bieten kann, und in Zukunft weiter an dem Thema geforscht werden sollte.

Danksagung

An dieser Stelle möchte ich mir die Zeit nehmen, mich bei all denen zu bedanken, die sich während des Verfassens dieser Arbeit im Speziellen und während meines Studiums im Allgemeinen für *mich* Zeit genommen haben.
Zuerst bei meinem direkten Betreuer am AIT, Marcus Rennhofer, für die Hilfe und Denkanstöße bei der Durchführung der experimentellen Teile und der Interpretation der Ergebnisse. Außerdem für seine Begutachtung und konstruktive Kritik zu dieser schriftlichen Arbeit.
Herrn Dr. Martin Gröschl danke ich für die Begutachtung seitens der TU Wien, und die freundliche Betreuung.
Weiters bedanke ich mich beim gesamten Team des AIT im Bereich Photovoltaik für die freundliche Aufnahme dort. Besonders ohne Ankit Mittal und Wisnu Ananda wäre die Durchführung der notwendigen Messungen und somit diese Arbeit nicht möglich gewesen.
In diesem Zusammenhang geht ein weiterer besonderer Dank an Diana Krainer, einerseits für die Outdoor Exposure Daten, die hier verwendet wurden, aber vor allem für die schönen Mittags- und Kaffee-Pausen während der Arbeit am AIT.
Ein zusätzlicher Dank geht an meine Freunde und Studienkollegen Dominic, Luki und Sebastian, dafür dass sie sich meine dummen Fragen und meine Nörgelei angehört und mir wann und wo immer möglich geholfen haben, im Bezug auf Studium, Arbeit und das Leben an sich.
Vielen lieben Dank auch an Alice und Sonja, die mich am AIT aufgegabelt und dann nicht mehr in Frieden gelassen, und die mich vor allem moralisch immer unterstützt haben.
Einen besonders herzlichen Dank schulde ich natürlich meinem Lebensgefährten Lukas, der mich während des Verfassens dieser Arbeit, im Lockdown und in Freiheit, bei Tag und bei Nacht aushalten musste. Danke, dass du mir Mut gemacht und immer an mich geglaubt hast, ohne dich wäre diese Arbeit vermutlich nie vollendet worden.
Abschließend danke ich aus vollem Herzen meinen Eltern Edith und Fritz, die mich von klein auf in allen meinen Entscheidungen bestärkt und motiviert haben, und wegen denen ich so bin, wie ich bin. Ohne ihre Unterstützung wären dieses Studium und dieser Abschluss niemals möglich gewesen.
Ein letztes Danke geht noch an Emmy, die den Abschluss meiner Arbeit leider nicht mehr erlebt, aber deren schnurrende Unterstützung mir sehr geholfen hat.

Nicole Zechner, August 2021

Contents

1 Introduction

Until the end of the 18th century all of humanity's energy needs were covered by firewood and air- and water-powered mills. Only with the beginning of industrialization and the widespread use of steam and combustion engines did mineral oil and coal gain importance. Especially after the economic crisis of 1929 energy demand soared. Since the 1960s natural gas and nuclear power joined oil and coal as primary energy sources. Even today oil, coal and natural gas account for roughly 85% of the world energy demand [1].
Energy demand is rising steadily worldwide and will continue to rise in the near future. Especially large emerging economies like China and India will increase their consumption of energy (both per capita and in total numbers) [1]. Energy generation is of large importance for the development of any society, making the ways energy is produced and used vital issues of humanity [2]. 68% of all greenhouse gas emissions can be attributed to the use of fossil fuels [3], making it the main driving force of the anthropogenous greenhouse effect [1]. To meet global ambitions in taking action against climate change, the deployment of renewable energy systems on large scales is an important step [4].

Of the many different options for power generation with reduced emission of greenhouse gases, this work will be dealing with photovoltaics (PV), the direct generation of energy from sunlight.

Photovoltaics has been described as the most versatile of all renewable energies due to its modular setup from single cells and modules. It can be sized to accomodate any use from systems generating a few milliwatts in handheld devices to huge multi-megawatt powerplants [1]. In countries with well established electricity grids, the energy produced by photovoltaic systems is mostly fed directly into the grid. For this application an accurate estimation for the expected power at any given time is the most important parameter of the power plant [5]. Photovoltaic devices exhibit changes in electrical parameters during light exposure, complicating estimations for power output [6].

Even though crystalline silicon photovoltaic modules still account for 95% of all manufactured photovoltaic devices [7], accurate estimations for the power output of all types of solar cells and modules is important for production and certification [8].
To accurately model outdoor performance of photovoltaic devices, the state reached in outdoor deployment must be well represented in indoor power measurements with simulated sunlight [9]. To generate this outdoor exposed state, prolonged light exposure by natural or artificial light (also referred to as „Light Soaking (LS)“) is the standard procedure according to the international standard IEC 61215/1-1-x [10]. But the standard also allows for the use of other stabilizing procedures, as long as the given standardized specifications are met [10].
One approach to alternative methods of stabilization for thin film photovoltaic devices is the application of a forward bias without light exposure („dark bias“) as proposed

by [6], [11] and [12]. Even though this purely electrical stabilization procedure yielded favorable results throughout literature ([6], [8], [9], [12]), little was published on the topic in the last five years.

The theoretical groundwork for this diploma thesis presented in chapter 2 consists of a brief review of the physical principles of photovoltaic power generation, followed by research of literature on purely electrical bias as an alternative method for power stabilization in thin film photovoltaic devices, taking into account publications from the last 15 years.

The experimental part of the thesis was conducted at the laboratories of the Austrian Institute of Technology (AIT) in Vienna. It consisted of applying dark bias to different types of photovoltaic (thin film) modules and measuring the electrical output over time in dependency on bias current and temperature. All measurement specifics and a detailed description of procedures can be found in chapter 3.

Chapter 4 contains the results of these measurements, which will be discussed in chapter 5, also giving an outlook on future prospects for the applied methods.

1.1 Motivation

The most important parameters for sizing a photovoltaic power plant are the exposure to sunlight in the location of the power plant andthe power output of the solar modules used [5, 13].
Nearly all photovoltaic devices exhibit performance changes when exposed to light, but the scale of these changes varies widely between different technologies [14]. While crystalline silicon devices are relatively stable on medium time intervals (minutes to days) and mostly suffer from long term degradation [14], thin film photovoltaic devices experience metastable effects (timed from seconds to days) that interfere with performance measurements [12].
Because of these metastabilities, norm IEC 61215-1 prescribes light soaking of thin film devices before their power is measured [10]. The procedure was introduced for amorphous silicon, historically the first thin film photovoltaic technology [14]. Other thin film technologies are currently subjected to the same stabilization procedure before power measurements, even though the method is not optimized for them [8].
In [11] electrical forward bias was proposed as an alternative to light soaking for stabilization of thin film photovoltaic devices.

In 2017 the Pearl TF-PV (Thin Film photovoltaic) project started, in a collaboration of German, Dutch and Austrian research and industry partners, including the Austrian Insitute of Technology. The project aimed to reduce cost of electricity produced by thin film photovoltaic powerplants. Among the goals of the project was to experimentally look into improved standardized measurements and technology specific preconditioning

methods [15].
One of the preconditioning methods was dark bias with a comparatively low biasing current of $\frac{1}{3}$ of the short circuit current. Somewhat surprisingly, this method yielded good results that had not been found in any previous experiments where much higher currents had been used. Since all four different modules types (CdTe, CIGS, CZTS) tested gave good results for dark bias, it was decided to look into the method further. This was the initiative for the experimental part of this master thesis.

1.2 Photovoltaic Power Generation

The sun is vital for life as we know it. The gaseous nuclear fusion reactor at the star's center emits electromagnetic radiation, determining the surface temperature of our planet and supplying virtually all energy for the natural processes of the earth's surface and atmosphere [16]. The amount of solar energy impinging on the planet each year is so large that far less than a percent of it could satisfy all of humanity's energy needs [1]. But this number means little to nothing, since we can only tap into a very small part of this energy potential for technical reasons [17]. One way to harness this energy is photovoltaic power conversion.
To generate electricity from primary energy, most processes we use today need at least two steps of energy conversion (wind turbines, tidal power plants) and fossil fuels even need three steps. Fossil fuels for example need to be burned, the generated heat is then used to drive an engine, and the rotational energy of the engine is finally converted to electricity in a turbine. [18]
Solar cells and fuel cells are the only technologies we have today that directly convert primary energy into electricity. For solar cells the primary energy is solar radiation [18]. They transform the energy of incident photons directly into electrical energy by use of semiconductor material characteristics [16].

The subsequent chapter provides a very quick overview of the historical development of photovoltaics, the potential of photovoltaic technologies for future development and takes a closer look at photovoltaic power generation in the European Union.

1.2.1 A brief history of photovoltaics

The interaction of light with matter has always been a topic of scientific interest [19]. The history of photovoltaics begins with the discovery of the photovoltaic effect by Edmond Becquerel in 1839 [1]. Becquerel was looking into the interaction of light and matter and found that selenium, but not copper, would exhibit increased conductivity under insolation [19]. In 1885 Charles Fritts built the very first photoelectric module from plates of pure selenium, trying to use the sun to generate electricity. The efficiency of the module was far smaller than 1%, so a use in energy generation was not tangible yet. [5]
With the works of Max Planck in 1900 [20] and Albert Einstein 1905 [21], the scientific

community started gaining some understanding for the underlying processes of these effects [5] [19] . But real solar cells were only feasible after the invention of the diode with a semiconductor junction by Walter Schottky in 1938 [19].
In 1948 the first light-sensitive silicon component was patented by Bell Labs, in 1954 they presented the first working silicon solar cell [19]. The early solar cells had an efficiency of around 5% and where far too inefficient for everyday use. Their only application in the early days was in spaceflight [1]. In 1958 the second American satellite Vanguard I was launched into orbit, equipped with photovoltaic cells that would reload the internal battery. The satellite's other batteries were empty after 19 days of use, but the photovoltaic cells kept recharging their battery and thus the mission going for over seven years [5].
Terrestrial use of photovoltaic modules was first evaluated for economic efficiency during the oil crisis in the mid-1970s and in the 1980s the first large pilot facilities were built [5]. Until the begin of the 1990s, photovoltaic energy production remained a niche mostly applicable for remote, off-grid locations. When Germany launched their "Tausend Dächer Programm" ("One thousand roofs initiative") this marked the start of bringing photovoltaic energy systems into economic use on a large scale [1].

1.2.2 Photovoltaics in the European Union

As of 2019, one fifth of global photovoltaic capacity is installed in the European Union [3]. The capacity was increased from 1.9 Gigawatts in 2010 to 133 GW in 2019, generating around 150 TWh of electricity or around 5.2% of the final electricity demand of the whole union [22].
In 2020 the new European Commission adopted a climate and energy package with three main targets: reduction of GHG levels; increase of renewable energy share; increase in energy efficiency [23]. To achieve these goals, it is estimated that the cummulative solar capacity of the EU must go up to around 440 GW until 2050 (for the baseline scenario) and up to 825 GW until 2035 for the more ambitious 1.5 degree goal [3].
To match the growing demand for PV installations in the European Union, and guarantee safe supply, regional production should also be ramped up. Until 2006 PV production was dominated by Japan and Europe, since then manufacturing has been scaled up especially in China, Taiwan and other Asian countries [3], with China now the major manufacturer of photovoltaic technology with a market share of 66% [7].
The current production capacity for solar cells and modules in the EU is about a third of a GW per annum [22]. A study by the Fraunhofer Institute has shown that European PV manufacturing can even be competitive, if an output of 5-10 GW per year can be realized [3], fueled by the recent fast decrease of costs and increase in demand [22].

1.2.3 Potential of photovoltaics

According to [24] solar energy has the potential to play a central role in the future of global energy systems, since it is highly predictable and ubiquitous. Apart from emissions caused

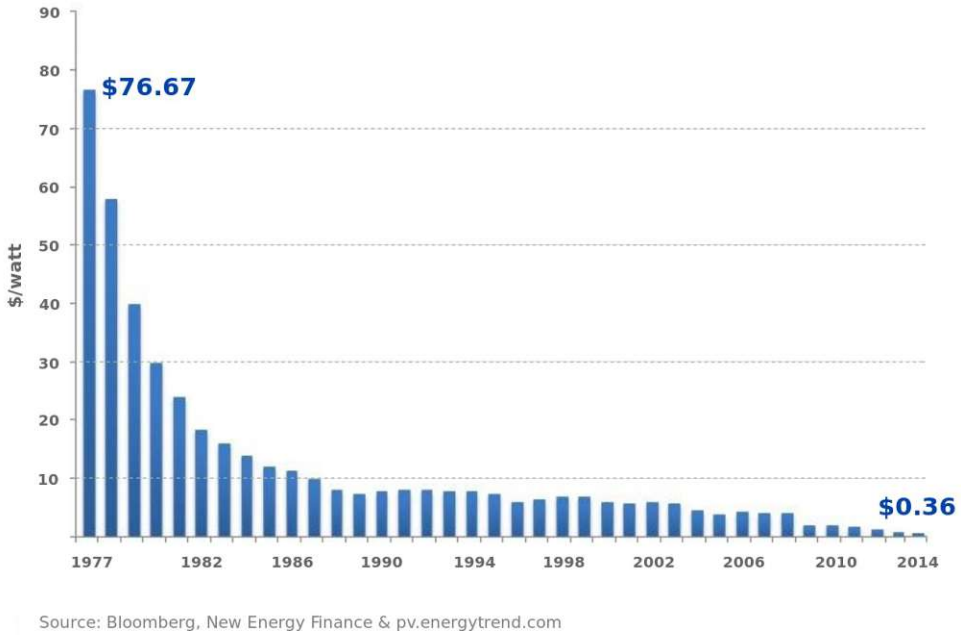

Figure 1.1: Price history of silicon PV cells, in US$ per Watt from 1977 to 2014 [25].

during production and decommissioning, photovoltaic modules do not contribute to the greenhouse effect during operation [17]. They also need no fuel other than sunlight [22].

In the United Nation's 'World Energy Assessment' from the year 2000 [17], it was stated that the potential of photovoltaics depends on cost reduction. In the past, PV had been associated with technical challenges, lack of manufacturing scale and economic barriers (especially the high initial costs for a PV system) [26].

Taking a look at figure 1.1, we see the price of silicon photovoltaic cells has fallen from 76.67 US$ in 1977 to less than half a percent of that in 2014 [25].

This falling of prices followed an empirical law for the last four decades: With every doubling of installed photovoltaic capacity, the average price of modules fell by an average of 20% [3]. This trend is named 'Swanson's Law' and expected to continue in the future [24].

This rapid cost reduction made photovoltaic power generation far more competitive [26]. It is now among the most cost-efficient technologies for electricity generation. The Joint Research Centre of the European Union (JRC) even expects the price for electricity from residential photovoltaics in combination with storage to fall below the retail price soon [22].

In [22] photovoltaics is fittingly named the 'no-regret option', because the technology

is ready to be deployed on a large scale in a short time. To meet the energy demand of the near future, even assuming a scenario with continued intensive use of fossil fuels, a large increase in renewable energy sources is predicted [1]. This means that no matter what, the total amount of PV energy will increase in the coming years.

2 Theoretical Background

This chapter will shortly revisit the theoretical background necessary to understand photovoltaic power generation and the effects observed in modules in the presented experiments. Starting with basic semiconductor properties (section 2.1) and light-matter interactions (section 2.2), this chapter then takes a closer look at the most essential part of a solar cell - the p-n-junction in section 2.3. Section 2.4 contains a review of methods for characterization of solar cells. A short overview of the basics for solar cell technology can be found in section 2.5 followed by an introduction of the most relevant types of solar cells for this thesis (c-Si, CZTS and CIGS) in section 2.6.
This overview of general theory of photovoltaic devices is then followed by the most integral part of this thesis in section 2.7 - the stabilization of solar cells and modules, as well as dark bias stabilization in section 2.8.

For the analysis of my experimental results I utilized (among other things) a fit via the Johnson-Mehl-Avrami-Kolmogorow (JMAK) equation and an Arrhenius fit, the basics of which are briefly discussed in section 2.9.

2.1 Semiconductor properties

To describe semiconductors and their properties, as well as their usefulness for photovoltaic technology, introducing the energy band model is important.

2.1.1 The energy-band model

Free electrons have an almost continuous range of energies. Electrons in isolated atoms have a well defined set of discrete energy levels they can occupy. And in an arrangement with several physically close atoms (e.g. a solid), these energy levels are spread into bands of allowed energies. These so called "energy bands" are either separated by bands of "forbidden" (meaning unobtainable) energies or overlap into each other, forming a continuum of allowed energies (as in a metal). [16] For a visualization of the concept (in a metal, magnesium), consider figure 2.1.

There are usually a large number of energy bands present in a material, but the two most important ones are the valence band (VB) and conduction band (CB). At absolute zero (T=0K) the valence band is the energy band of the highest energy that is filled [1] up to a certain energy level, the Fermi level E_F [16]. The energy band of the next highest energy is called the conduction band and is completely empty at 0K. [28, 29]

[1] "filled" meaning fully occupied by electrons in accordance with the Pauli principle.

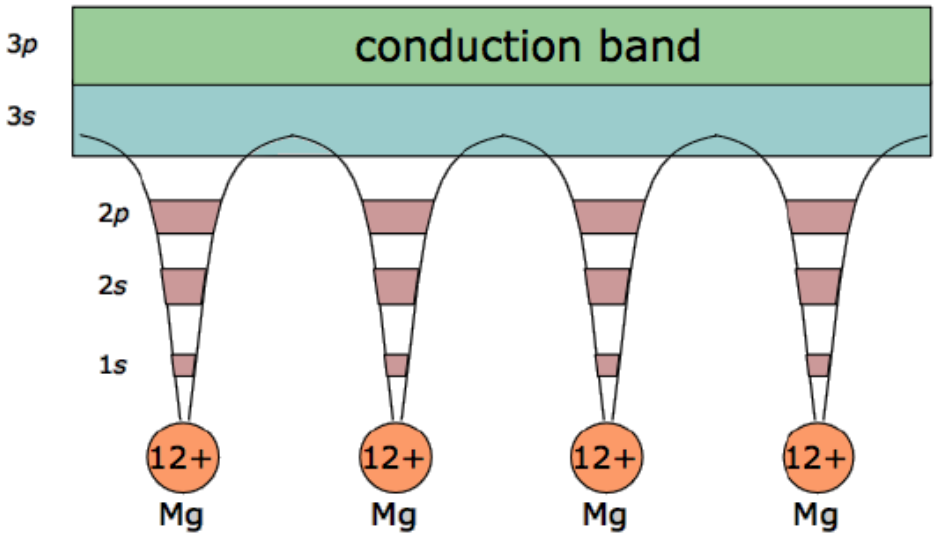

Figure 2.1: Energy levels and potential wells in a solid (magnesium). 1s, 2s and 2p states are not overlapping, electrons in these states are kept in the potential well. 3s states form the valence band. 3p states form a conduction band, overlapping 3s states, contributing to a possible flow of electrons.Adapted from [27].

The energy difference between valence and conduction is called the (energy) band gap E_g [29].
When temperature rises $T > 0K$, electrons gain energy and rise to the conduction band, leading to a higher concentration of charge carriers there, and to electric conductivity. The electrons also leave behind an empty spot in the valence band, called a hole, that can be described as a positive charge [28]. The occupation of any energy state E is calculated via Fermi-Dirac distribution

$$f(E) = \frac{1}{e^{\frac{E-E_F}{k_B T}} - 1} \tag{2.1}$$

with E_F the Fermi-energy, k_B Boltzmann's constant and T the absolute temperature [16].

The difference between insulators, semiconductors and metals can be described in energy band theory as such [16]:

- **metals:** E_F within a valence band, that band is only partly filled and transport of electrons is possible
- **insulators:** fully occupied valence band, empty conduction band, E_F between these two bands; neither a completely empty nor a completely full energy band can contribute to current flow
- **semiconductor:** an insulator with a very narrow band gap, such that at temperature $T > 0K$ the Fermi-Dirac distribution of electrons smears out so much that

some electrons enter the conduction band, leading to current flow [16]

2.1.2 Doping and impurities

To increase the number of electrons and holes contributing to current flow in semiconductors, one can introduce impurities in the form of foreign atoms into the material (doping) [30]. Impurities generally introduce states of allowed energies within the band gap, degenerating semiconductor properties [16].
In silicon, which has four valence electrons in a pure Si lattice, the introduction of atoms with either three or five valence electrons destabilizes the crystal structure, making it easier for charge carriers to be excited. [16] More generally speaking: Additional electrons (n-type doping[2], introduction of electron donators) experience only the Coulomb force and are not covalently bound to neighboring atoms [28], resulting in smaller binding energies of these electrons; the energy to free impurities is $E_{imp} \approx 0.02\text{eV}$ and thus much smaller than the band gap (e.g. $E_{Si} \approx 1.1\text{eV}$ for silicon) [16]. „Missing“ electrons leave positively charged holes (p-type doping, introduction of electron acceptors), where other electrons can be easily captured. [28]
The Fermi-levels of doped semiconductors move farther away from the middle of the band gap towards either the conduction band (n-type doping) or the valence band (p-type doping) [16].

2.1.3 Carrier density and transport

Due to the Fermi-Dirac distribution, most electrons are clustered near the band edges. The number of electrons n per crystal volume for a given energy E is calculated by the integral

$$n = \int_{E_C}^{E_{C_{max}}} f(E)N(E)dE \tag{2.2}$$

with E_C the minimum energy of a state in the conduction band, $E_{C,max}$ the maximum energy of a state in the conduction band, $f(E)$ the Fermi-Dirac distribution and $N(E)$ the energy density of allowed states (with $N(E) \propto (E - E_C)^{\frac{1}{2}}$).
This leads to an electron density

$$n = N_C \cdot e^{\frac{E_F - E_C}{k_B T}} \tag{2.3}$$

and the hole density

$$p = N_V \cdot e^{\frac{E_V - E_F}{k_B T}} \tag{2.4}$$

with $N_C \propto (m_e \cdot k_B T)^{\frac{3}{2}}$ and $N_V \propto (m_h \cdot k_B T)^{\frac{3}{2}}$ the densities of electrons/holes with mass m_e/m_h in the conduction/valence band. For a perfect semiconductor $n = p$. [16]

[2] n-type since current flow is carried primarily by negatively charged particles, in contrast to p-type doping; [30]

The product $n \cdot p$ is a constant for a material at given temperature T, called the intrinsic carrier density n_i [29]:

$$n \cdot p := n_i^2 \tag{2.5}$$

The two main ways of transport of charge carriers in a semiconductor are diffusion and drift. Both are caused by a gradient in charge carrier density. Diffusion is directly fueled by this gradient, while drift is caused by the electric field induced by the charge carrier gradient. [29]

2.2 Interaction of light and matter

The following section will summarize the most important interaction of light and matter for photovoltaic power generation - the inner photoelectric effect, followed by a short discussion of absorption and recombination of charge carriers in semiconductors.

2.2.1 Photoelectric effect

If a negatively charged, isolated metal sheet is illuminated with ultraviolet light, its charge decreases. This means that negative charge carriers (=electrons) must have been emitted from the sheet. Experiments in 1902 led to the empirical observations that kinetic energy of emitted electrons depended only on the wavelength and not on the intensity of the incoming light and that the number of emitted electrons is proportional to the intensity of the light. The theoretical explanation came from Albert Einstein in 1905, for which he received the Nobel Prize in physics sixteen years later. Einstein postulated the existence of light quantums (=photons). Via this explanation, each absorbed photon transfers its entire energy to an electron in the metal sheet, so that its kinetic energy is

$$E_{kin}^{max} = h\nu - W_a \tag{2.6}$$

with h Planck's constant, ν the frequency of incoming light and W_a the work needed to free electrons from their binding in the metal. [28]
One can distinguish between outer and inner photoelectric effect:

- The outer photoelectric effect describes the emission of electrons from the nucleus by high-energy incident photons. [1]
- The inner photoelectric effect requires lower photon energies, but is limited to semiconductors. It is the basis for photovoltaic power generation. [13]

2.2.2 Absorption and recombination

Light impinging on a semiconductor with photons of energies $h\nu$ larger than the energy gap E_g between VB and CB can create an electron/hole pair in the material. We distinguish between two different kinds of material in respect to their absorption of photons:

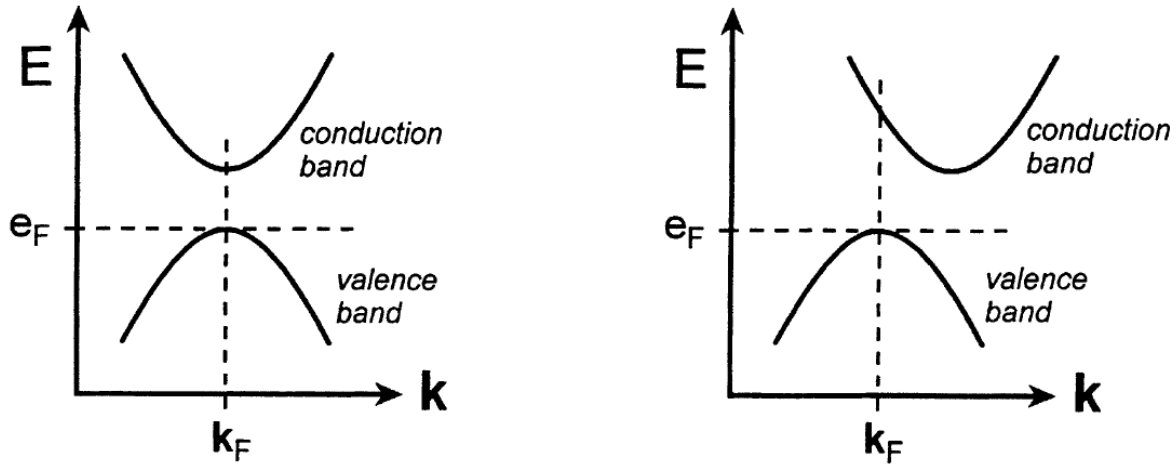

Figure 2.2: Comparison of indirect and direct band gap in a wave vector k/energy E graph with Fermi energy e_F and Fermi wave vector k_F. As described above, for indirect band gaps, the maximum energy of the valence band and minimum energy of the conduction band are shifted against each other, whereas the two extreme points are aligned naturally in direct band gaps. Adapted from [31].

direct and indirect band gap materials. Absorption here means the absorption of a photon by excitation of an electron from the valence band to the conduction band, leaving a hole in the valence band. [16]

Direct band gap materials are characterized by the quick absorption of photons. The probability of absorption depends on electron density in the VB and the density of empty states in the CB, both of which increase quickly with increased energy above the band gap edge E_g. [16]

Indirect band gap materials either need photon energies much higher than the band gap energy E_g or the involvement of a phonon to create an electron/hole pair. Since an additional condition (the existence of the phonon) is required, the probability of light absorption is much smaller than in direct band gap materials. [16] This means that rather thick sheets of semiconductor are needed for high absorption [1].

For a better understanding of in-/direct band gap semiconductors, consider figure 2.2.

Recombination of excess charge carriers occurs through one of three processes, all of which run in parallel [16]:

1. radiative recombination: the reversal of light absorption, excited electron falls back into relaxed state by emission of excess energy as light, important for direct band gap semiconductors

2. Auger recombination: energy from recombination of electron and hole is given to a

second electron, important at high doping concentrations

3. trap recombination: two state recombination process with relaxation from CB to a defect state within the band gap, and from there to the VB; important in indirect band gap semiconductors

2.3 p-n junctions

Bringing a p-doped semiconductor in direct physical contact with an n-doped semiconductor creates a so called p-n-junction [1]. Against the immediate intuition (that electrons would flow from regions of high electron concentration to regions of lower electron concentration until equilibrium is reached), electrons leaving the n-type region create a charge imbalance by leaving behind a surplus of positive charges in the form of exposed, ionized donor atoms. These atoms in turn create an electric field opposing the natural diffusion tendency of charge carriers, until an equilibrium between the two modes of carrier transport is reached. [16]

The charge distribution according to diffusion and drift current shows the existence of a so called Space Charge Region (SCR) or depletion region at the interface of p- and n-doped materials, an insulating region with no charge carriers and high electric field [32]. Any system in thermodynamic equilibrium can have only one Fermi-level [3] [32]. As described in section 2.1.2, the Fermi-levels of p- and n-doped semiconductors of the same material [4] are different from each other. So in order for a p-n-junction to have both one continuous Fermi-level and different Fermi-levels for n- and p-region, the conduction and valence band must *bend* near the p-n-junction [32].

Electrons are energetically excited by incoming photons and raised to the conduction band in the p-region. Those electrons which diffuse to the SCR without recombination are then forced into the n-region by the electric field (the process will also be described with more detail in section 2.4). They get collected and are then available as electric power, and can also be re-transfered to the p-region via an electric load, completing the electric circuit powered by incident light [29].

The most basic solar cells are essentially large area pn-junction diodes [16]. This idea will be exploredin a little more detail in section 2.6.

[3] the Fermi-level can also be defined as total electrochemical potential of electrons
[4] as well as Fermi-levels of different materials

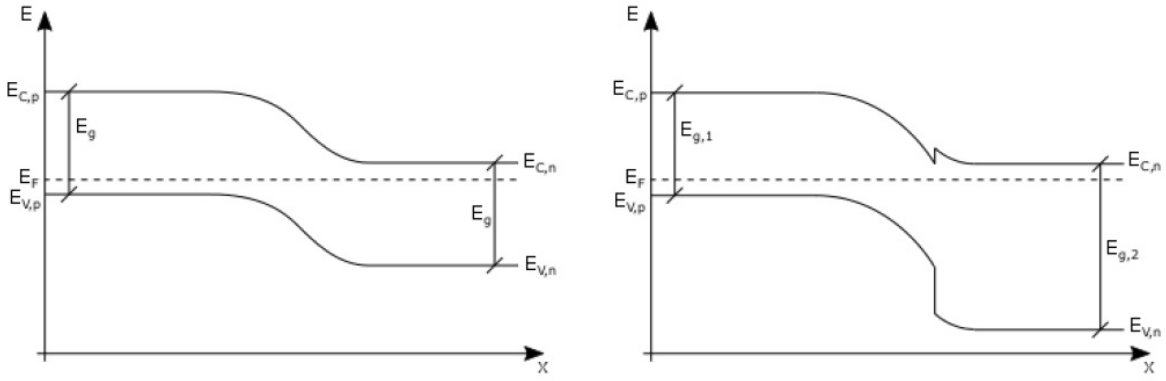

Figure 2.3: Schematic overview of a pn homojunction (left) and heterojunction (right), showing the bending of energy bands to accomodate a constant Fermi energy E_F. Note that for the heterojunction there is a jump on the right side of the junction for the conduction band. Figure adopted from [29].

2.4 Characterization of solar cells and modules

For proper understanding of the characteristics of illuminated solar cells, it is advisable to first take a look at the dark characteristics of solar cells without the presence of light. The accompanying graphic for the following derivation for carrier distributions inside a pn-junction can be found in figure 2.4.

In [16] three reasonable approximations are made to help find the density and current of minority carriers in a pn-junction:

1. sharp division of the diode into a depletion region, and the quasi-neutral zone (with charge density $\rho = 0$)
2. minority carrier concentration at the edge of the depletion region depends exponentially on the applied voltage
3. minority carriers in quasi-neutral regions flow by diffusion rather than drift, because their small number effectively shields them from the electric field

In the n-side of a diode, the current density for holes is

$$J_h = -qD_h \frac{dp}{dx} \tag{2.7}$$

with charge q, diffusion constant D_h and hole concentration p (derived simply from the fact that particle flux is proportional to the negative of the concentration gradient). Using the continuity equation for holes in a semiconductor

$$\frac{1}{q}\frac{dJ_h}{dx} = -(U - G) \tag{2.8}$$

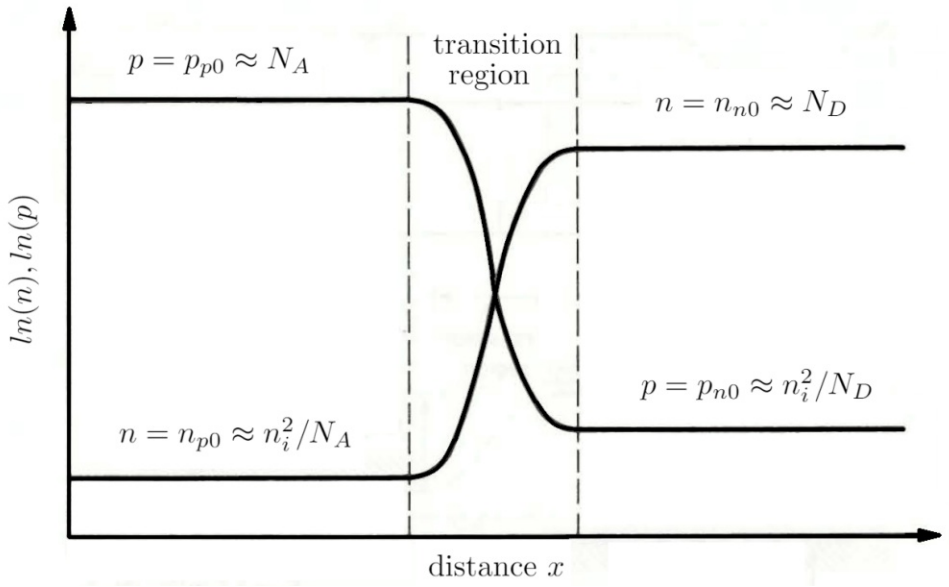

Figure 2.4: Distribution of charge carriers in a pn-junction. Hole density p, electron density n, with specific points of interest $p_{n,b}$ and $n_{p,a}$ the minority carrier concentrations at the edges of the junction that spans from point a to point b. Adapted from [16].

where G is the generation rate of electron-hole-pairs (for any diode in the dark, $G = 0$) and U is their recombination rate, as well as the identity

$$U = \frac{\Delta p}{\tau_h} \tag{2.9}$$

leads to the differential equation

$$D_h \frac{d^2 p_h}{dx^2} = \frac{\Delta p}{\tau_h} \tag{2.10}$$

with p_h...hole density, Δp...deviation of carriers from equilibrium and τ_h...carrier lifetime.

After using an exponential ansatz and applying appropriate boundaries, the carrier density is found to be

$$p_h(x) = p_{n,0} + p_{n,0}\left(e^{\frac{qV}{k_B T}} - 1\right) e^{\frac{-x}{L_h}} \tag{2.11}$$

with $p_{n,0}$... hole density in n-type region in thermal equilibrium, V...applied voltage, k_B... Boltzmann's constant, T...temperature, x...expansion in x-dimension and L_h... diffusion length ($L_h = \sqrt{D_h \tau_h}$). The same can be done for the minority carrier in the p-type region (electrons) and leads to an analogous outcome for electron density $n_p(x')$.

Using the carrier density $p_h(x)$ from equation 2.11 in combination with equation 2.7 for current flow follows a version of the ideal diode law:

$$I = I_0\left(e^{\frac{qV}{k_B T}} - 1\right) \tag{2.12}$$

with the saturation current density

$$I_0 = A\Big(\frac{qD_e n_i^2}{L_e N_A} + \frac{qD_h n_i^2}{L_h N_D}\Big) \tag{2.13}$$

with A...diameter of the diode (area) and N_A and N_D number of acceptors and donors. [16] The saturation current density is generally a thermally activated property that can also be written as:

$$I_0 = I_{00} e^{\frac{-E_a}{k_B T}}$$

where E_a is the activation energy and the factor I_{00} is all but independent from temperature. [33]

2.4.1 Current-voltage-characteristic

For an illuminated p-n junction, there is an additional current generated by electron-hole pairs [32]. To find the characteristics of this p-n junction such that the generation rate G is constant throughout the device, following the same thought process as in the previous section, but keeping in mind that $G \neq 0$ leads to a differential equation similar to equation 2.10:

$$D_h \frac{d^2 p_h}{dx^2} = \frac{\Delta p}{\tau_h} - G \tag{2.14}$$

Again using an exponential ansatz and the same boundary conditions as before, the current flow density becomes

$$J_h(x) = \frac{qD_h p_{n_0}}{L_h}\Big(e^{\frac{qV}{k_B T}} - 1\Big)e^{\frac{-x}{L_h}} - qGL_h e^{\frac{-x}{L_h}} \tag{2.15}$$

which is *almost* the same as for dark characteristics, but with an additional factor depending on the generation rate G. This allows to formulate the adapted diode law as

$$I = I_0\big(e^{\frac{qV}{k_B T}} - 1\big) - I_L \tag{2.16}$$

with the additional light generated current I_L defined via diffusion lengths of charge carriers (L_h and L_e) as well as the width of the space charge region W:

$$I_L = qAG(L_e + W + L_h) \tag{2.17}$$

This means that the characteristic relation of current I and voltage V in an illuminated diode, is just the ideal diode law tuned down by the light-generated current I_L, under the assumption that I_L includes in fact all light-generated carriers (meaning there are no losses to recombination etc.). [16]

From here one can go on to define the most interesting electrical parameters of solar cells:

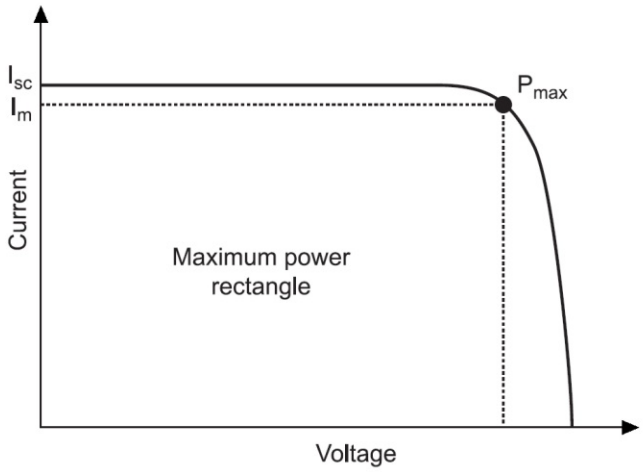

Figure 2.5: Current-voltage curve of a solar cell, with voltage open circuit voltage on one axis and current short circuit current (I_{SC}) on the other. The maximum power (P_{max}) is also denoted. Adapted from [33].

Short-circuit current (I_{sc})

In a short circuit ($V = 0$) evaluating equation 2.16 shows that the current in the diode is

$$I_{sc} = I(V = 0) = -I_L \tag{2.18}$$

. Under ideal circumstances, the short-circuit current of a solar cell is equal to the generated photocurrent I_L. [16] In equation 2.17 it can be seen that I_L and thus I_{sc} depends directly and linearly on the generation rate G and because of that also on irradiation. Properties L_e, L_h and W are material dependent and practically independent of both irradiance and temperature. Using the linearity of the relation between irradiation and short-circuit current allows the usage of highly stable (mostly c-Si) reference cells to measure irradiation instead of a much more expensive pyranometer [5] [29].

Open-circuit voltage (V_{oc})

Plugging $I = 0$ into equation 2.16 and solving for V gives us

$$V_{OC} = \frac{k_B T}{q} ln\left(\frac{I_L}{I_0} - 1\right) \tag{2.19}$$

the open-circuit voltage [16]. V_{oc} is heavily dependent on the semiconductor characteristics of the solar cell material via both I_L and even more via I_0 (see equation 2.13, I_0 depends directly on diffusion constants, intrinsic carrier density and the number of acceptors and donors).

[5] As is also mentioned in section 3.2.1 discussing the small solar simulator, the setup included a reference cell based on this principle.

Fill Factor (FF)

The fill factor is defined as

$$FF := \frac{V_{mp} I_{mp}}{V_{OC} I_{sc}} \tag{2.20}$$

with V_{mp} and I_{mp} the voltage and current in the maximum power point (MPP). The fill factor is a measure of the "squareness" of an I-V curve. [16] It is an indicator of solar cell performance [32].

Maximum Power (P_{max})

Since the focus of this thesis is the power output, maximum output power P_{max} (also often called MPP maximum power point in literature) is also included as a parameter here. It is defined as

$$P_{max} = I_{mp} V_{mp} \tag{2.21}$$

[29]

Figure 2.5 depicts a idealized IV curve for a solar cell.

Resistances R_{shunt} and R_{series}

Solar cells experience two kinds of parasitic resistances, shunt and series resistance. shunt resistance (R_{shunt}) comes mostly from the bulk resistance of the semiconductor material, the bulk resistance of metallic contacts and connections as well the contact resistance between metallic contacts and the semiconducting material. series resistance (R_{series}) is caused by leakage across the pn-junction on cell edges and other peripheral areas. The leakage arises from crystal defects and foreign, unwanted impurities in the junction region.

Both R_{series} and R_{shunt} reduce fill factor. A very high series resistance can even reduce I_{sc} and a low shunt resistance can decrease V_{oc}. These influences can also be seen in the IV characteristic, like in figure 2.6. [16]

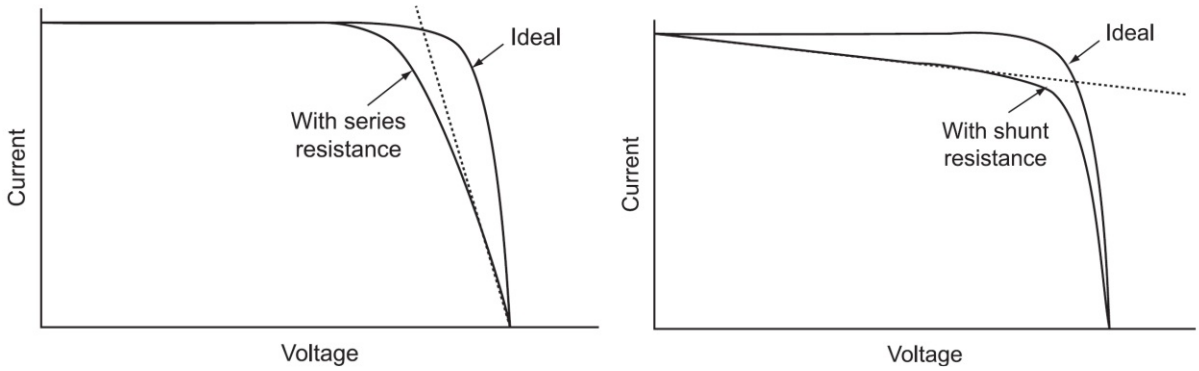

Figure 2.6: Influence of series (a) and shunt (b) resistances on the IV characteristic of a solar cell. A large R_{series} reduces the slope of the characteristic on the V_{oc} side, and a small R_{shunt} decreases the slope on the I_{sc} side. Adapted from [33].

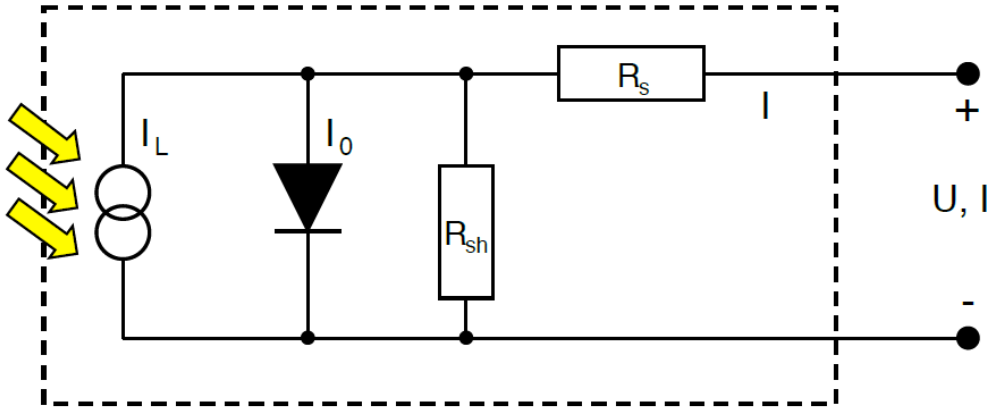

Figure 2.7: The most basic equivalent circuit of a solar cell, compiled using simple electronic components. Most important are the photocurrent I_L, in parallel to a diode with current I_0 and the parallel shunt resistance, and a series resistance. Adapted from [32].

The complete electrical behavior of a solar cell can be described by an equivalent circuit like the one in figure 2.7. It consists of a diode with diode current I_0, connected in parallel with a constant current source I_L (the photocurrent). Both sources are again connected in parallel to a shunt resistance R_{shunt} and in series to a series resistance R_{series}. [32]

2.4.2 Electroluminescence Imaging

In order to ensure the intactness of full scale modules throughout the biasing procedures, Electroluminescence (EL) imaging was performed on them. This section goes on to briefly explain the theory behind EL imaging.
Electroluminescence imaging is a non-destructive measurement technique that gives fast, high-resolution, two-dimensional images. The method is applied in quality control and important in research and industry. [34] When a photovoltaic module is operated in reverse, it functions as a light emitting diode (LED), emitting radiation rather than absorbing it. The radiation emitted by recombination of excited charge carriers can then be detected by a sensitive Si-CCD camera with wavelengths from 300-1000nm. Modules are usually supplied with an external current $I_{ext} \leq I_{sc}$. Damaged areas will look darker, less radiant than fully operational areas. [34]

2.5 Basics of solar cell technology

This section contains a description the basic structure of solar cells with the help of the example of crystalline and amorphous silicon and CIGS solar cells in order to understand the technological principles. In varying degrees of modifications, this design is the same for all solar cells.

A single solar cell is simply put nothing but a large area diode with a junction that is exposed to incoming light. The area facing the light (usually negatively doped silicon n-Si) has to be very thin ($< 0.5\mu m$) so that as many photons as possible can get sufficiently close to the junction. This also means that front contacts must be as small as possible and not shade too much of the cell. To reduce losses due to reflexion on the surface, an anti-reflective coating is usually applied. [13]

The equivalent circuit of a solar cell in the dark is a normal semiconductor diode with a forward current from p to n region. Under insolation an additional power source of photocurrent I_{sc} is introduced into the circuit. [1, 13]

Using a photodiode as a source of voltage requires the addition of a resistance R parallel to the photodiode. R needs to be small enough that the resulting voltage induced by the photocurrent is always smaller than the diffusion voltage U_D. This setup is used in solar cells to transform incoming solar radiation into electrical power. The used load needs to be adjusted to allow the solar cell to work in its maximum power point (MPP). [28]

2.6 Types of solar cells

While the main part of the experiments featured in this work have been conducted on thin film solar cells (CZTS mini modules, CIGS full scale modules), crystalline Silicon (c-Si) solar cells (mono-cSi) were also investigated for reference. Moreover, since c-Si cells were historically the first ones and are still today the majority of all solar cells produced [7], they are included in this brief overview of types and technologies of solar cells.

2.6.1 Crystalline silicon solar cells

As mentioned above, crystalline silicon is the most used material in solar cells today and is a good way to understand the build of solar cells. For a structural sketch of a typical c-Si cell see figure 2.8. In varying degrees, this built is valid for all solar cells.

Pure silicon is derived from naturally occurring minerals like quartz sand (SiO_2) via several steps of chemical processes and purifications. The output consists of long, cylindrical silicon rods, that are then sawed in slices of 150 to 350 μm thickness. These slices are called wafers. The wafers are then cleaned, doped with gas diffusion using phosphorus or boron, screen printed with contacts and coated with an anti-reflective layer. [1]

c-Si modules

Individual, unprotected c-Si cells are very prone to withering. The solution is to combine single cells to modules. The front cover is usually a sheet of glass, the back cover is either glass or plastic. The cells are usually themselves embedded in plastic and connected to

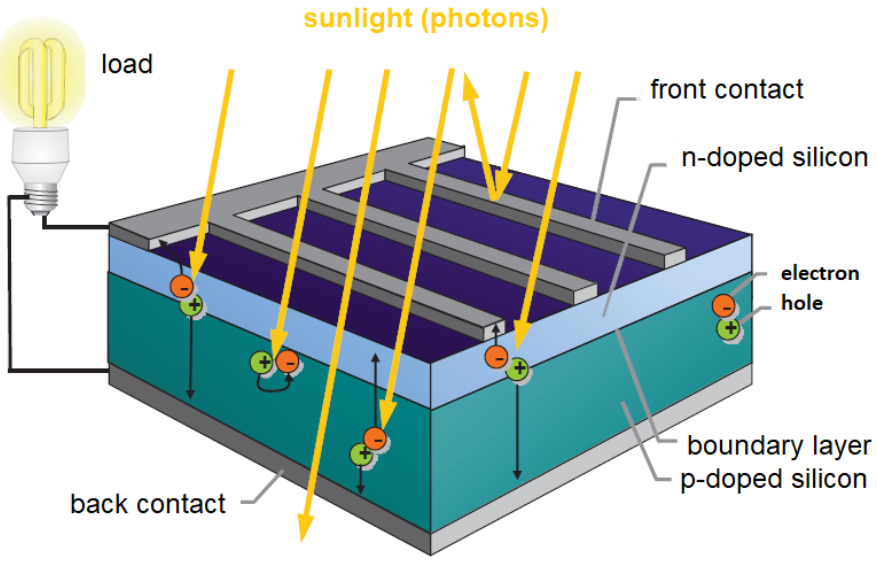

Figure 2.8: Structure of a c-Si solar cell, with incoming sunlight and charge carriers, as well as all integral parts of the cell, from front contact and n-doped silicon layer to p-doped silicon layer and back contact. Includes a schematic load connected to front and back contacts, closing the electric circuit.
Adapted from [1].

each other and an external plug. [1]

2.6.2 Thin-film solar cells: a-Si

Again taking historical development into account, Amorphous Silicon (a-Si) cells were the first type of thin film solar cells. All other thin film photovoltaic devices are similar in structure to a-Si cells.
The basis of an a-Si cell is a carrier, usually glass. A thin layer of zinc peroxide (ZnO_2) is sprayed onto the glass. Then silicon and its doping agents are added via evaporation deposition: First a 10nm p-doped layer, followed by a 10nm buffer layer, followed by the main 500nm layer of amorphous silicon. On the other side of the silicon, a 20nm n-doped layer is applied. Then front and backside are contacted (mostly with aluminium or silver contacts). [1]

Amorphous means that there is no long range order in the arrangement of silicon atoms, and not each silicon atom is necessarily connected with four others. This also means that there are small voids in the structure, leaving so called 'dangling bonds'. These dangling bonds together with the highly aperiodic arrangement lead to large densities of allowed states in the 'forbidden' energy area. [16]. Because of these many allowed states, the indirect semiconducting crystalline silicon turns into direct semiconducting amorphous silicon, where no additional phonon is required to absorb a photon [19] (for

in-/direct semiconductors, see also section 2.2.2).
One immediate impact of the direct band gap in amorphous silicon is a much stronger absorption, and thus a significant reduction of solar cell thickness [16]. This is the basis of thin film photovoltaic technology, requiring a thickness of around $1\mu m$ [16], around a factor 100 thinner than traditional c-Si cells [1], reducing material use and costs [19].
The problem with a-Si cells is the Staebler-Wronski effect. It is a light-induced degradation effect that lowers efficiencies of cells between 10% and 30% after initial deployment. The mechanism behind the effect is connected to a breaking of weak silicon-silicon bonds by optically excited carriers, producing defects that lower carrier lifetime (although the exact microscopic mechanism is not yet fully understood). [14].

Another issue with thin film PV devices was their historically lower efficiency [13, 16]. The National Renewable Energy Laboratory (NREL) in the US reported the best c-Si research cell efficiency (for single crystal c-Si, plus a concentrator) at 27.6%, while the best a-Si (a-Si:H stabilized) was lagging behind at only 14% [35]. But, in the same publication, efficiencies for non-a-Si thin film cells were much higher: 23.4% for CIGS, 22.1% for CdTe and 29.1% for GaAs. So this historical disadvantage is no longer as distinct today.

2.6.3 Thin-film solar cells: CIGS

Copper Indium Gallium (Di-)Selenide (CIGS) solar cells are based on the semiconducting mineral chalcopyrite and can function as photovoltaic material in a large variety of compositions due to its defect rich nature. The most common CIGS cells consist of five layers, typically grown on a substrate (glass or flexible) in consecutive steps. First molybdenum is sputtered onto the substrate as Ohmic back contact, followed by evaporation of the main layer of absorption, p-type Cu(In,Ga)Se_2. Using a chemical bath, an n-type CdS buffer layer is applied next, completing the heterojunction of the solar cell. This is then followed by sputtering of two layers of zinc oxide, once weakly, then heavily doped, forming the "window" layer and also acting as the front contact. Figure 2.9 contains a schematic intersection of a CIGS solar cell, including the thickness of each layer. [32].

2.6.4 Thin-film solar cells: CZTS

Copper Zinc Tin Sulfide (CZTS) solar cells (also often referred to as kesterites) are seen by some as promising candidates for the next generation of thin film PV, replacing CIGS cells [36, 37]. The metastable effects of CIGS solar cells are quite well researched by now, and known to be reversible (more on metastable effects in section 2.7). Since CZTS cells have the same architecture as CIGS, it stands to reason that these effects will be quite similar. [37]. CZTS cells have high absorption coefficients and a tuneable direct band gap between 1 and 1.5eV [36].

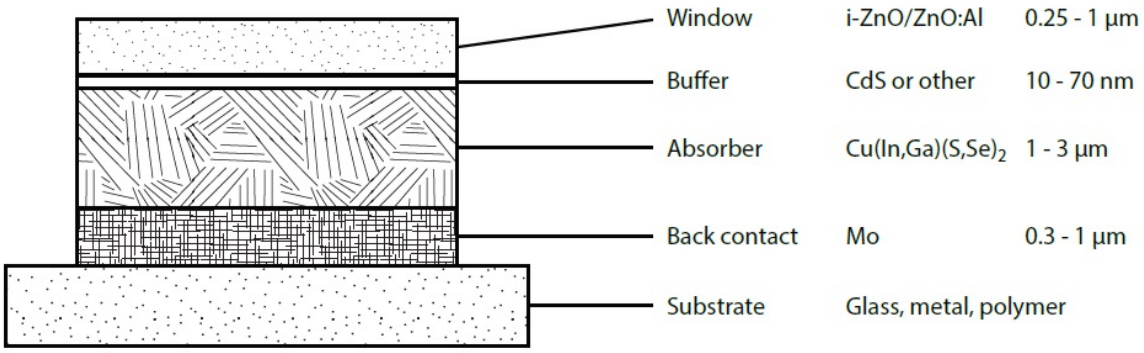

Figure 2.9: Structure of CIGS cell layers in intersection. Starting with the substrate layer, the contact, absorber, buffer and window layers are sputtered or evaporated onto the layer beneath it. On the right side typical thicknesses for all layers are listed. Figure from [32].

2.6.5 Other thin film solar cells

There is a growing variety of thin film solar cells, both in laboratories worldwide and on the market. There will be no closer inspection of these types of cells in this thesis, since they were not included in my experiments, but for the sake of completeness a short list and description is added here. For more information on them, consider any recent book on photovoltaic engineering, for example [33].

- **GaAs:** Gallium Arsenide (GaAs), direct band gap semiconductor with a very close to the ideal band gap for energy conversion (GaAs band gap: 1.42 eV [13]), similar in structure to c-Si, major limitation is the high material cost [16]

- **CdTe:** Cadmium Telluride (CdTe) is a group II-VI semiconductor and an ideal PV material, with high optical absorption and a near ideal direct band gap of 1.44 eV [32]. While CdTe solar cells are about as efficient as CIGS cells [32] and show all the benefits of thin film photvotoltaic technology, they do have an important downside: The use of the highly toxic cadmium. Some sources show concern over this matter ([13]), while others gloss over it, citing strictly controlled factories with workers that are not exposed to any cadmium ([33]), the end-of-life treatment does seem to raise problems, since no company can ever guarantee that every CdTe cell will be treated appropriately when it is decomissioned [13].

- **organic material:** organic solar cells are being researched worldwide, but face the difficulty of finding good donor/acceptor materials. They do not produce free charge carriers, but rather excited electrons and holes that are not bound together. Their largest advantage is their operability at low temperatures and a good output to cost ratio, while their main disadvantages for now are low efficiencies and low lifetime. [29]

2.7 Metastable effects in solar cells and modules

Almost all photovoltaic devices exhibit performance changes during light soaking, although the scale of these changes varies significantly between technologies; thin film PV devices are especially prone to them. The changes during light soaking include long-term changes in device performance as well as reversible metastable effects. The letter lead to a device performance depending on history of illumination, electrical bias, temperature and a number of other outside influences [14]. While thin film PV devices have been in production for decades, their performance characterization is still a topic of ongoing research. This results partly from the fact that while all thin film cells exhibit some sort of metastable behavior, the technologies used are diverse and each is physically very different from the well established crystalline silicon cell [38]. Precise measurements are hindered by reversible metastable changes. These changes range in time scale from a few seconds to a few days. Another problem is the possiblity that metastable effects are confused with permanent degradations [12]. Understanding of metastabilities will lead to more accurate characterization of PV devices [39].

Some problems of the characterization of thin film photovoltaics come from differences in simulator performance. Depending on the technology of the PV device scattering can differ substantially when measuring the same module in different ways or at different facilities. This has lead to endeavors for repeatability of indoor measurements via a number of international studies. These studies use round-robin tests to compare results from different labs worldwide. While they found a spread of maximum power of $\pm 1.5\%$ for c-Si modules, it was $\pm 3 - 6\%$ for thin film round-robin tests. Significantly better results were achieved in the second round of round-robin tests on thin film devices, after they had undergone harmonizing stabilization procedures before measurement. [38]

Over the years, many techniques have been proposed to ensure stabilization of module power before measurements, addressing the many underlying physical processes to varying degrees [38].

Amorphous silicon photovoltaic devices and the Staebler-Wronski effect were historically the first metastable effects to be noted and 'explained' (see also section 2.6.2). The degradation in performance in the first few hundred hours of operation can lead to a loss of efficiency of 10-30% (on average 16%) according to [38]. The international IEC standard IEC-61215 prescribes light soaking until stabilization before power measurements, but this technique was designed specifically for a-Si modules and is not optimal for other thin film PV [8, 10].
In a-Si PV devices the loss of power comes from the Staebler-Wronski effect and is associated with dangling bonds and defect centers limiting carrier lifetime. The degradation has been shown to be depended on light exposure, while current injection and other methods lead to different results. To account for this effect, prolonged exposure to light in a light soaking process was deemed a good solution to standardize power measurements in a-Si devices [14]. Currently, this procedure is the one specified explicitly by IEC-61215-1,

stating that stabilization is assumed when the change in output power is smaller than 2% for three consecutive power measurements ($\Delta P_{max} \leq 2\%$) [10]. This procedure takes into account the large degradation of a-Si devices during light exposure and the very slow recovery rate at room temperature [38]

Copper Indium Gallium (Di-)Selenide PV devices exhibit metastabilities of electrical parameters due to illumination or bias. They consist of temporary increases or decreases of voltage V_{OC} or fill factor, and usually relax in dark storage. [32]
Early work was done on CIGS metastable behavior by Ruberto and Rothwarf in 1986 [40], indicating that the effect was induced by voltage rather than illumination. Today there are very different metastable behaviors in CIGS devices depending on the material, stack design and film quality [32], but there is still no consensus about the exact physical nature of the underlying effect(s) [39].
The effects on CIGS PV devices are subdivided in most research into light- and bias-induced metastabilities, with light-induced metastabilities further divided into red and blue light effects [14]. Red illumination appears to increase the acceptor concentration in the absorber (from persistent photoconductivity), metastably increasing V_{OC} and the capacitance of the heterojunction. Blue illumination seems to be absorbed mainly in the CdS buffer layer, decreasing junction capacitance. Finally reverse bias increases junction capacitance (much like red illumination), but not net acceptor density. While the blue light effect acts to the benefit of cell behavior, it only counteracts but does not cancel the deterioting effects of red light and reverse bias that are also present in white light soaking (for preconditioning according to IEC-61215) [41].
There are still a number of explanations for the exact mechanisms of CIGS metastabilities; the most recent ones suggest a common origin of all metastable effects in an amphoteric Selenium-Copper divacancy complex ($V_{Se} - V_{Cu}$) that converts between acceptor and donor configurations during light absorption [14, 41].
There are some factors that should always be taken into consideration when interpreting experimental results of metastabilities in CIGS devices [39]:

- module state due to (accidental) previous light exposure
- effects on time scales $< 1s$ that are usually not shown due to slower measurements

While **crystalline Silicon** has no known *metastable* behavior, light soaking still induces degradation. In boron-doped monocrystalline silicon solar cells there is an initial light induced degradation effect with a power loss of around 4% that is reversible in dark annealing or storage. The effect is most likely ascribed to a light-induced activation of a boron-oxygen defect in the material. [14]

2.8 Dark Bias stabilization

This section relays the basic idea behind a power stabilization induced by application of forward current bias with small currents while the module is in the dark - the main concept pursued in this thesis.

year	authors	modules	bias	temperature	time
1993	Sasala et al. [11]	CIS, CdTe	10.47 $\frac{mA}{cm^2}$	not reported	2h
2010	Del Cueto et al. [8]	CIGS, CdTe	V_{MPP}-V_{OC}	65±5°C	48h
2012	Deline et al. [6]	CIGS	I_{MPP}	25°C	96h
2014	Silverman et al. [12]	CdTe	V_{MPP}	55°C	1.5h
2015	Deceglie et al. [9]	CIGS	$< V_{OC}$	not reported	not reported

Table 2.1: Overview of previous dark bias publications considered before the experiments featured in this work were conducted.

2.8.1 Basic idea

As mentioned extensively already, the official IEC standard for power stabilization of photovoltaic modules (IEC 61215-1 MQT 19 [10]) was designed for a-Si modules and is not optimal for other thin film photovoltaic devices, since the reason for metastable behaviors of a-Si and other devices clearly differ from each other, see section 2.7 .
The idea to utilize an external bias rather than direct illumination was proposed in the 1990s ([11]) and a number of publications came from it in the time from 2010 to 2015, mainly from the NREL ([8] in 2010, [6] in 2012, [12] in 2014 and [9] in 2015), for an overview also consider table 2.1.

Basic work on dark biasing of thin film devices was done in the frame of the European project PEARL-TF PV [15]. There, dark biasing as a tool for power stabilization was investigated and unexpectedly found favorable. On basis of this data the presented work investigated in depth the influence of important parameters on the dark bias behavior. The parameters used in the Pearl TF-PV project for current bias in the dark was **1/3 $\mathbf{I}_{sc}$ at 45°C** for at least two cycles of **30 minutes** and used as a baseline for the conducted experiments (for details, see chapter 3).

2.8.2 Literature review of previous experiments worldwide

The first notable mention of dark (voltage and current) bias comes from Sasala and Sites of Colorado State University in their 1993 paper "Time dependent voltage in CIGS and CdTe solar cells" [11]. They found that the application of pre-measurement bias in the dark significantly reduces the voltage shift they observed in light exposure of CIGS and CdTe cells. However they applied a very high constant current bias (10.47 $\frac{mA}{cm^2}$ [6]). The discussion of [11] concludes that placing a cell in forward bias prior to illumination negates the increase in V_{OC} seen in all investigated cells and suggest that the voltage increase is triggered by the bias itself rather than a direct result of illumination.
In their 2010 "Progress toward a stabilization and preconditioning protocol for polycrystalline thin-film photovoltaic modules" del Cueto et al. [8] from the NREL report on

[6] for comparison, calculating the current bias per area for some of my own measurements, found that for a bias of 1/3 I_{sc} the applied bias was around 0.25$\frac{mA}{cm^2}$, for 2/3 I_{sc} 0.54$\frac{mA}{cm^2}$ and for 1 I_{sc} 1.7$\frac{mA}{cm^2}$

traditional light soaking compared to dark biasing and long term outdoor exposure of CIGS and CdTe modules. They applied a bias voltage between V_{MPP}-V_{OC} at around 65°C for 48 hours. In their paper they find the data on whether indoor light soaking or dark bias brings faster stabilization was inconclusive, but that both methods appear to bring nearly equal results for stability, albeit they report that both methods sorely lack behind the accuracy of outdoor deployment. They also observed that higher currents (near I_{MPP}) bring faster stabilization. Finally, they distinguish between two types of metastable effects:

1. **short term** metastable effects:
   minutes to hours, saturated by outdoor preconditioning

2. **long term** metastable effects:
   for time frames larger than 100 hours, requiring elevated temperature and bias to stabilize

Two years after the publication of del Cueto et al., Deline et al. at the NREL published their findings on "Electrical bias as an alternate method for reproducible measurement of Copper Indium Gallium (Di-)Selenide photovoltaic modules" [6]. Their methods included dark storage with a forward current bias of I_{MPP} at 25°C for 96 hours after outdoor deployment, in comparison to unbiased dark storage after the same outdoor exposure. They report that biased modules maintain their performance within a margin of $< \pm 1\%$ of the outdoor performance and are completely stabilized within a few hours, finding that bias has definite benefits. In another sub-experiment they find that while a module stored unbiased degenerates fast after outdoor exposure, with a decrease of $\approx 14\%$ in performance in the first 24 hours, while the biased module's performance drops only by 4-5%, all of which is recovered within 1 hour after bringing the module indoors.
Deline et al. also note that the primary IV parameter showing losses is the fill factor, followed by V_{OC}, which they find to be conclusive with the proposed defect mechanism by Lany and Zunger [41] that was already discussed in section 2.7.

It is once again the NREL that reports on "Performance stabilization of CdTe photovoltaic modules using bias and light" by Silverman et al. in 2014 [12]. Among other experiments, they investigated CdTe modules that had previously been in outdoor exposure and annealed to a bias stabilization at a voltage bias V_{MPP} at 55°C for 1.5 hours. They conclude that for outdoor comparability light soaking is preferable over dark bias.

Finally in 2015 Deceglie, Silverman et al. from the NREL published "Validated method for repeatable power measurement of CIGS modules exhibiting light induced metastabilites" [9]. In their experiments, forward bias in the dark was used only to "preserve" the light exposed state, not to bring stabilization by itself and thus their findings are not too relevant for this work.

The biasing current used was much smaller than that used in the other cited literature, only 1/3 I_{sc}, and the time of exposure was also shorter at 30 minutes. As reported above, the results appeared promising and led to a closer investigation of the possibilities by the

author.
The biasing parameters here were oriented on the parameters of those in the Pearl project, and tuned both temperature and applied current during bias, while keeping the exposure time at 30 minutes before each IV measurement. For details on methods see chapter 3.
The lower bias current was chosen to avoid degradation and to reduce the possibility of convoluting stabilization changes with systemic degradation of modules (systemic degradation would not stabilize, but continue).

2.9 Johnson-Mehl-Avrami-Kolmogorow equation

To gain better understanding of the experimental results, a fit following the Johnson-Mehl-Avrami-Kolmogorow (JMAK) equation was applied. The JMAK equation shall be discussed shortly in this section, as well as the origins and applications of it.
The JMAK equation is at the heart of a theory of the kinetics of transforming phase volume $V(t)$ under consideration of nucleation and growth rates [42]. It is applied widely for the interpretation of crystallisation processes in many fields and can be universally applied to any type of material [43]. For the derivation of the equation, consider for example [43]. For fitting, the final finding of the JMAK equation is utilized, a behavior of the transformed volume $V(t)$ according to:

$$V(t) = 1 - e^{-V_{ext}(t)} = 1 - e^{(-kt)^n} \tag{2.22}$$

with t...time, $V_{ext}(t)$...the already transformed volume at time t, typically proportional to kt^n with an unspecific, temperature dependant constant k and Avrami-exponent n. [42] This was adapted to equation 3.2 in section 3.5.1 for fitting of the data presented in this thesis.
This gives a sigmoidal or s-shaped curve with "slow" beginning and ending and a fast transformation in between (consider figure 4.12 in chapter 4 for a visualization). The Avrami exponent n gives information about the dimensionality of the underlying process, with n=4 for a 3-dimensional growth. [43].

2.9.1 Arrhenius behavior

Arrhenius' equation gives a simple description for temperature dependence of reaction rate constants. It is valid for all phenomena with an underlying mechanism following Boltzmann statistics for their energy distribution [44].
For the evaluation of the JMAK fits, Arrhenius plots with 1/Temperature on the x-axis and the natural logarithm of the inspected variable (τ or n) on the y-axis were used.

3 Methods

The experimental part of this work is twofold: First the application of different combinations of temperature and bias current on various CZTS mini modules to find favourable parameters (section 3.1.1). These experiments were carried out on the 'small' sun simulator (section 3.2.1). The information gained from these experiments (results presented in section 4.1) was used to apply the most promising combinations of bias and temperature on full scale CIGS and c-Si modules; these experiments needed the use of a climate chamber (section 3.2.3) and were measured in an IEC 60904-9 [45] standardized flasher (section 3.2.2) using standardized IEC IV measurement procedures IEC 60904-1 [46].

3.1 Modules

Photovoltaic modules used for the experiments include CZTS, CIGS and c-Si type modules. For details on these types of solar modules, see section 2.6.

3.1.1 CZTS mini modules

CZTS (for details see section 2.6.4) mini modules used for the first part of the experiments were supplied directly by the manufacturing company. They were used without any recent pretreatment or measurements.
The samples used come from three different batches: **M1853**, **M2063** and **M2064**. M1853 samples (as indicated by their lower number) have come to the laboratory for previous testing and already been used before the measurements presented here. They were in dark storage at room temperature for a few months in between. Samples from batches M2063 and M2064 came directly from the manufacturer right before being used in these measurements.

The modules came in two sizes (see also figure 3.1), smaller ones from batch M2063 with a surface area of $\approx 20 - 25cm^2$ and larger ones of batches M1853 and M2064 with $\approx 88 - 90cm^2$ surface.

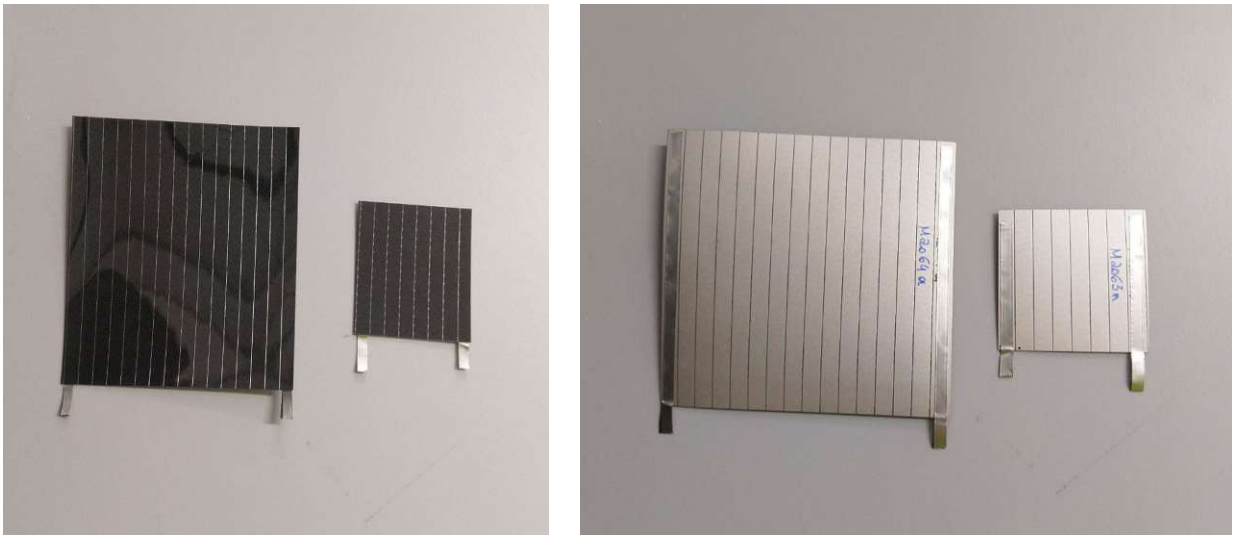

Figure 3.1: CZTS mini modules M2063n (right module, surface area of 21.62cm^2) and M2064a (left module, surface area of 88.8cm^2); they are representative for all mini modules used in these experiments.

3.2 Solar simulators and measurement devices

According to the IEC standard 60904-9 [45] solar simulators can be used for either IV-measurements or irradiance exposure. For the experiments only the measurement of IV curves was utilized. The main components of any solar simulator are a light source plus its power supply, the optics and filters necessary to manage the light beam according to the IEC 60904 classifications and controls for operation.
Solar simulators are classified by the IEC standard 60904-9 in three major classes (A through C, with A the best class) in each of three categories:

- spectral match
- spatial non-uniformity
- temporal stability

This leads to a classification of solar simulators as e.g. AAA, AAB etc. Moreover solar simulators can be classified according to their mode of operation as steady state, single pulse or multipulse simulators.

3.2.1 Small solar simulator

The 'small' sun simulator at the PV laboratories at AIT Vienna was used for measurements of all CZTS mini modules' IV curves. A picture detailing the setup can be seen in figure 3.2.

Figure 3.2: Setup of the small sun simulator, consisting of: [1] AAA class steady state solar simulator Xenon lamp, [2] temperature sensors, [3] high power series sourcemeter, [4] water cooling for lamp and sample and [5] the darkened chamber for measurements.

Using a 53 Ampere Xenon arc lamp, optics and filters, it simulates the natural solar spectrum in a steady state. The components of the simulator are:

- **sun simulator**: class AAA steady state solar simulator with a Xenon arc lamp
- **darkroom**: a small, light-proof darkroom where measurements take place without the interference of light other than that of the sun simulator, for a look inside the darkroom see figure 3.3
- **high power series sourcemeter**: the device is run as variable current source while applying a set bias voltage ramp. The current and voltage can be measured in 2-point or 4-point configurations. For transformation of data to the accompanying software, from where it can be extracted and used for more detailed analysis
- **reference cell**: monocrystalline silicon reference cell (RS-ID 4), very accurate cell (used for financial reasons instead of a much more expensive pyranometer). Short circuit current of the reference cell is exactly proportional to irradiance, thus allowing to indirectly measure irradiance.
- **cooling**: water cooling for the system, including the measurement platform
- **temperature sensor**: two temperature sensors are used, one is fixed to the reference cell, the other is always placed under the sample with tape
- **contacts**: samples are contacted with manually adjustable pins

3.2.2 PASAN Flasher

The full size flasher used to measure IV curves of CIGS and cSi modules is a class AAA pulsed solar simulator manufactured by PASAN, using an electronic load rather than a decade as resistance. The uncertainty for both current and voltage measurements is 0.1%. In principle, the PASAN flasher is a large version of the small sun simulator described in the previous section, and will not be described in more detail.
All measurements took place at STC and following instructions from IEC standard 60904-1 [46] (*Measurement of photovoltaic current-voltage characteristics*).

3.2.3 Climate chamber

While for the small solar simulator heating of modules was possible in situ through a heated measurement plate, the use of a separate climate chamber was necessary for the biasing of full scale modules.
The climate chamber was used to keep modules at constant temperature during the time of biasing. Its temperature stability is $\pm 1K$ of the set target temperature.
Modules were introduced into the chamber at room temperature, then the heating was started, and when the target temperature was reached on all thermal probes attached

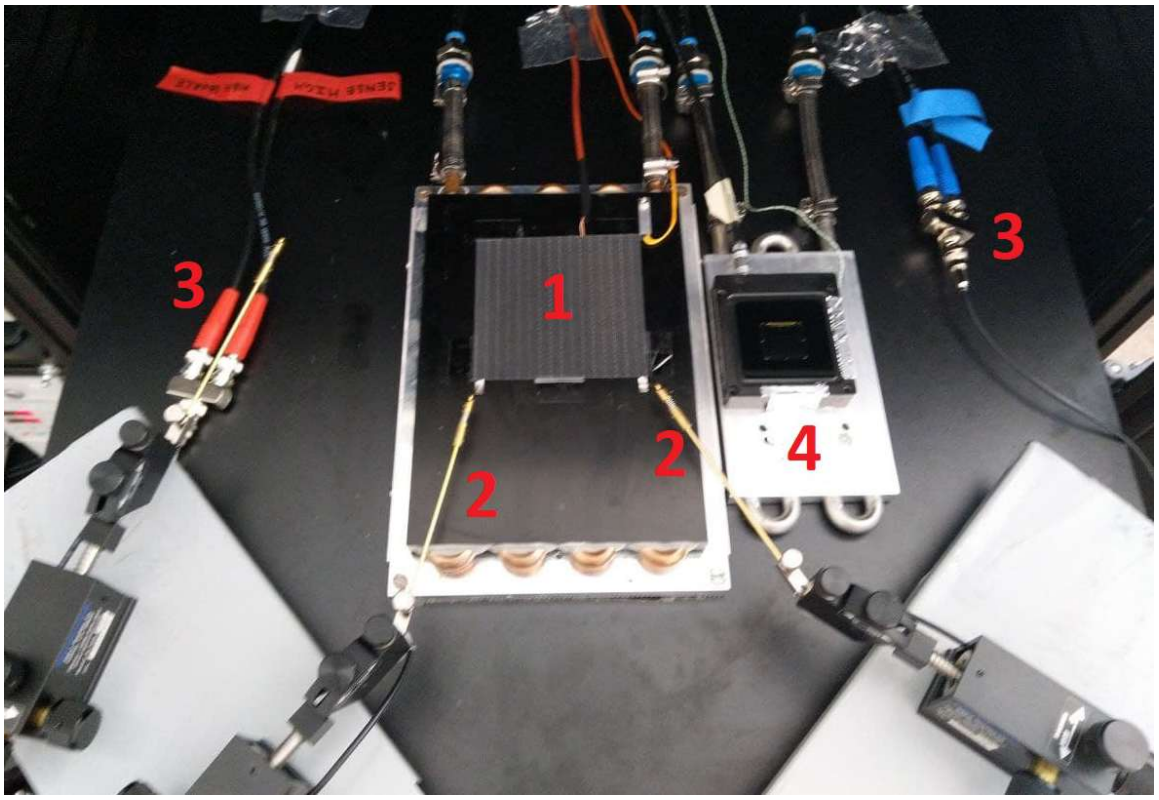

Figure 3.3: Setup within the darkroom of the small solar simulator. [1] sample M2064a, [2] the contacting pins, [3] wiring of contacting pins, [4] c-Si reference cell RS-ID 4

to the modules, the bias voltage was started. Due to the fast dynamic of the climate chamber (> 20 K/min) it is assumed that the time of modules at elevating temperature is small compared to the time at the set temperature during active bias application. Additionally, the dynamics are slowed down exponentially for temperatures lower than the target (Arrhenius' law).

3.3 Stabilization criterium

As specified in IEC 61215 the measuring procedure was continued until the relative change of the maximum power P was below 2% for three consecutive cycles in a way that

$$\Delta P = \frac{P_{max} - P_{min}}{P_{average}} \leq 0.02 \tag{3.1}$$

with P_{max} the largest value of P over the three cycles, P_{min} the smallest value of P over the three cycles and $P_{average}$ the averaged power of three consecutive cycles. When this stabilization criterium was met, the power output of the module was considered stabilized according to IEC 61215.
Measurements were stopped either after the condition $\Delta P \leq 0.02$ was met, or it appeared that no stabilization was possible in a reasonable amount of time (5-7 cycles).

3.4 Measurement procedures

3.4.1 CZTS mini modules: Measuring procedure

A flow chart of measuring procedures can be found in figure 3.4.
All measurements were done as follows: Samples were always handled with gloves, and cleaned before a new measurement. Then the sample was fixated on the measurement platform as close as possible to the reference cell with transparent tape; the temperature sensor was placed directly underneath the sample and also fixated with tape.
After contacting the sample with the pins, a first IV curve was measured at STC. This first measurement was the *initial* measurement used as reference point in all plots and also defined the bias current - bias currents applied were fractions of the I_{SC}, either $\frac{1}{3}$, $\frac{2}{3}$ or 1 I_{SC}. Then the temperature was set to the biasing temperature (25, 50 or 65°C). When the biasing temperature was stable (±0.5°C), the current bias was applied for 30 minutes.
After 30 minutes, the bias current was turned off and the temperature was brought back to 25°C for an STC IV measurement. This completes one cycle.
Measurements were carried on until the stabilization criterium (equation 3.1) was met for three consecutive cycles.

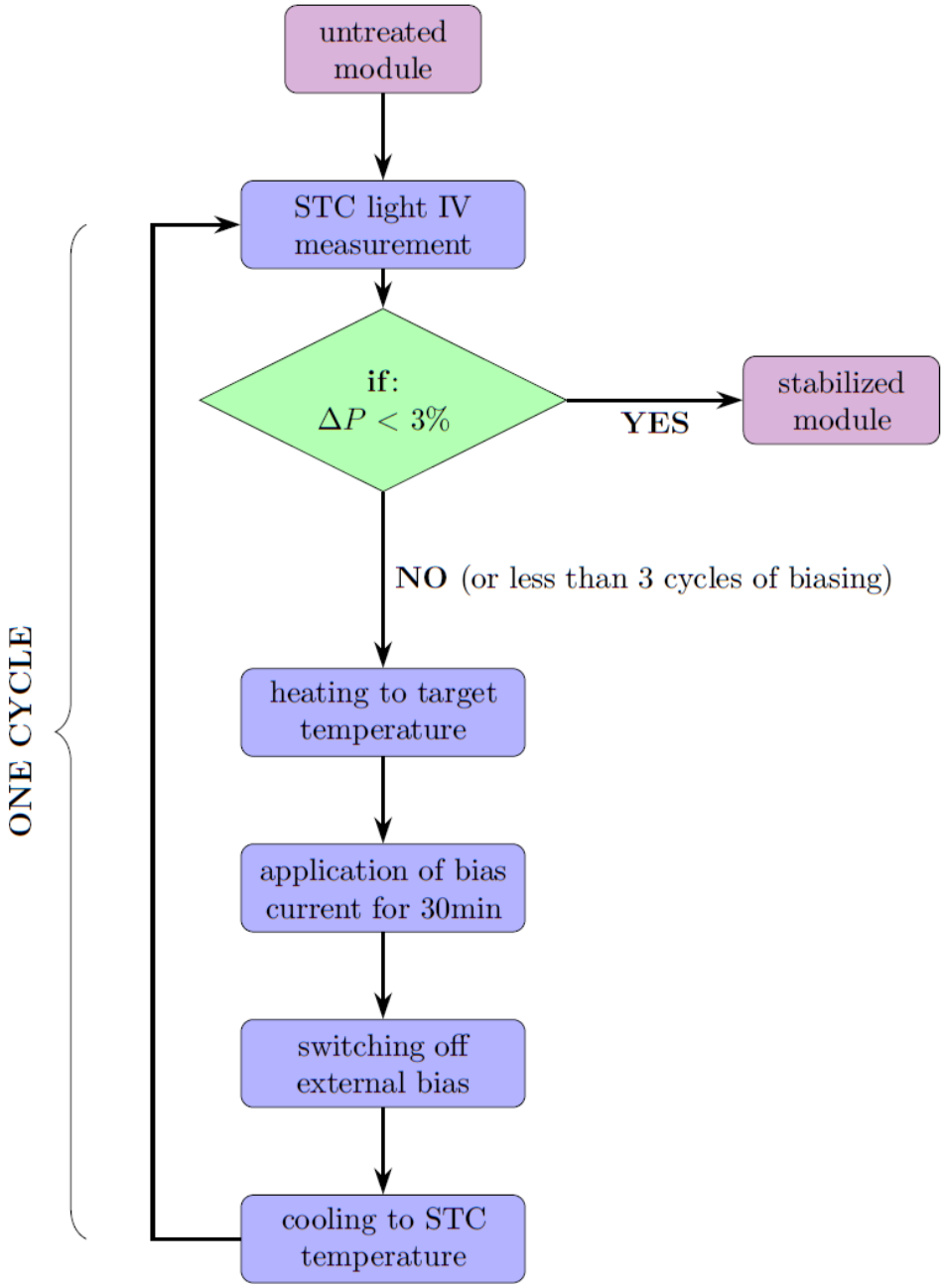

Figure 3.4: Measurement procedure for CZTS and full scale modules.

Route	R 1 Bias	R 1 Temp	R 2 Bias	R 2 Temp	Module
A1	1/3 I_{sc}	25°C	1/3 I_{sc}	50°C	M1853a
					M1853b
					M2063d
A2	1/3 I_{sc}	25°C	2/3 I_{sc}	25°C	M1853c
					M2063g
B1	1/3 I_{sc}	50°C	2/3 I_{sc}	50°C	M1853d
					M2063i
B2	1/3 I_{sc}	50°C	1/3 I_{sc}	65°C	M2063k
					M2063l
C1	2/3 I_{sc}	50°C	2/3 I_{sc}	65°C	M2064a
C2	2/3 I_{sc}	50°C	1 I_{sc}	50°C	M2063n
					M2064b

Table 3.1: Overview of biasing routes for CZTS mini modules. 'R' stands for Round. R 1 Bias corresponds to the biasing current used in the first biasing round applied to this module, R 1 Temp corresponds to the temperature during bias, analogous for round 2. For a better overview, consider figure 3.5.

3.4.2 CZTS mini modules: Biasing routes

Table 3.1 contains a list of parameters of the different biasing routes applied to the CZTS mini modules. For an overview also consider figure 3.5.
Each of the modules underwent two rounds of biasing (round 1 and 2), with a variation of temperature and/or current bias. Round 1 is divided into three groups - A, B and C. Each group marks a certain bias current and temperature. In the second round, modules undergo a change of these parameters and are again separated into groups 1 and 2. For example, a module with B2-biasing was biased at 1/3 I_{sc} and 50°C in round 1 and after a resting period with 1/3 I_{sc} and 65°C. The time between two rounds of biasing was always at least 24 hours.
This form of biasing in two steps was performed to observe the changes in electrical output of modules coming from higher temperatures and higher bias current separately.

3.4.3 Full scale modules CIGS & cSi: Measuring procedure

Full scale modules were also treated according to the basic measurement procedure pictured in the flow chart of figure 3.4.
The full scale CIGS and cSi modules first underwent an initial measurement in the IV flasher before starting with the biasing experiments. This measurement was used to determine the bias current, taking the average of the two I_{sc} values of each technology. The biasing current for the thin film modules (CIGS) was set at 1/3 of the averaged I_{sc} of the two modules as:

$$I_{bias,CIGS} = \frac{1}{3} \cdot (\frac{I_{sc,1} + I_{sc,2}}{2})$$

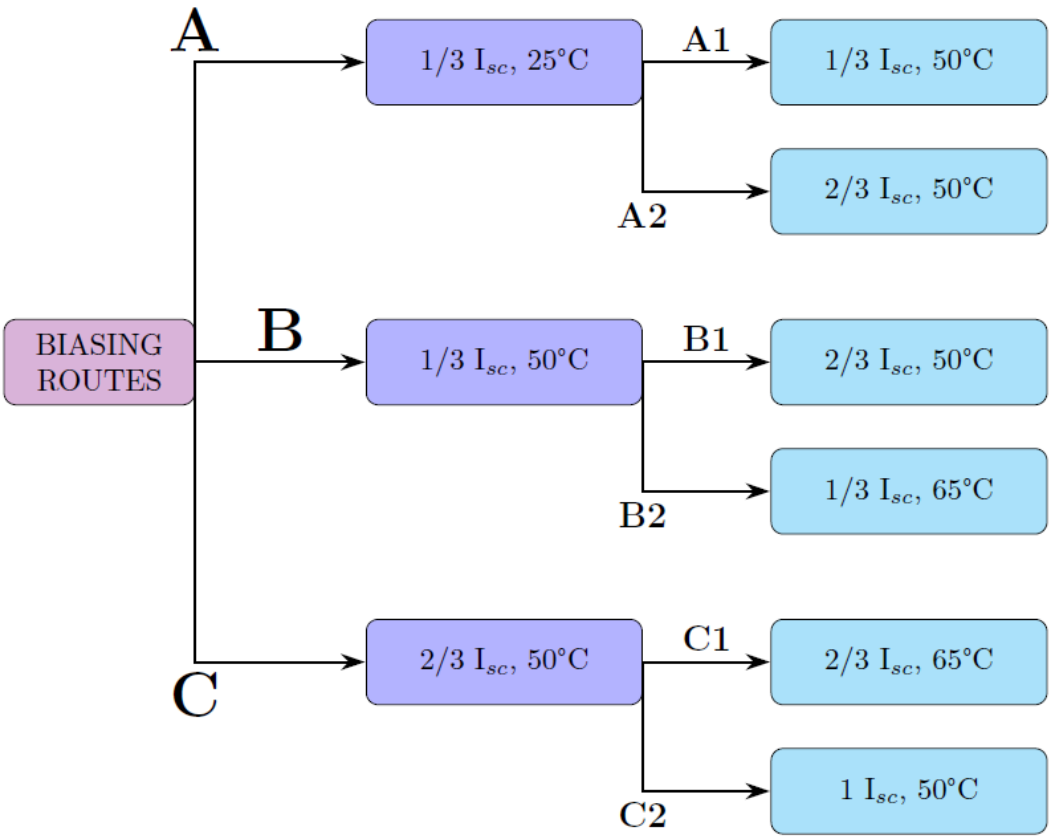

Figure 3.5: Schematic overview of the applied biasing routes for CZTS mini modules. For example, a module in the A2 category was biased in round 1 (=A) with 1/3 I_{sc} at 50°C until stabilization was achieved. After a resting period of at least 24 hours, the same module was then biased with 2/3 I_{sc} at 50°C until stable again. See also table 3.1.

Round	Temperature	Current bias	Module Type	Modules
1	50 °C	1/3 I_{sc}	CIGS	CIGS 01, CIGS 02
	50 °C	2/3 I_{sc}	c-Si	cSi 1, cSi 2
2	65 °C	1/3 I_{sc}	CIGS	CIGS 01, CIGS 02
	65 °C	2/3 I_{sc}	c-Si	cSi 2, cSi 3
3	85 °C	1/3 I_{sc}	CIGS	CIGS 01, CIGS 02
	85 °C	2/3 I_{sc}	c-Si	cSi 2, cSi 3

Table 3.2: Biasing parameters for the full scale modules (CIGS and c-Si), with temperature, current bias and module type and name. For details on the biasing procedure, see section 3.4.3. Note that 1/3 I_{sc} for the CIGS modules corresponded to 0.79 A, while 2/3 I_{sc} for c-Si modules were an applied 6.43 A .

modules	shutter	current [A]	sensitivity	exposure time [s]
c-Si	2.8	10	250	10
CIGS	2.8	2	250	10

Table 3.3: Parameters for all electroluminescence imaging of investigated full scale modules.

For the mono-c-Si modules, a biasing current of 2/3 of the initial I_{sc} was used. The higher current used for the crystalline silicon modules was applied because a higher current would be needed to find a measurable change in the generally stable c-Si technology.

An initial Electroluminescence picture was also taken of each of the modules before the first biasing, with the settings found in table 3.3 .

After this initial characterization, the modules were brought to the climate chamber, manufactured by CTS (in a different laboratory of the same building). For better cable management, the two CIGS and two c-Si modules were connected with each other in series, and then in series to one external power source for each circuit (as mentioned in table 3.2, the CIGS modules were biased with 0.79 A and the c-Si modules with 6.43 A). To follow and better control the temperature and current in the modules during the biasing, a Keysight 34972A data logger (serial number MY49015882) was used. One thermal probe was attached to the back of one module of each technology, and then connected into the Keysight logger. A shunt resistance of 100mΩ was implemented to measure the changing current and voltage of the modules (see also table 3.4).

After setting up the required electronics, the climate chamber was set to the desired temperature (50, 65 or 85 °C). It took between 3 and 5 minutes for the probes to reach this temperature. When it was reached, the external power sources with the biasing currents were turned on. Both temperature and bias were maintained constant for 30 minutes. After 30 minutes, the external bias was turned off and the chamber was brought to cool down to room temperature. The modules might have been exposed to the elevated temperature slightly longer than 30 minutes sharp, but - as stated above - the dynamic of the cooling in this chamber is so fast (> 20 K per minute), that it the effects are negligible.

Device	device #	Channel	Module Type
thermal probe	80	101	c-Si samples
thermal probe	101	102	CIGS samples
shunt resistance	14	210	c-Si samples
shunt resistance	11	211	CIGS samples

Table 3.4: Overview of devices and device numbers as well as channels in the datalogger used for the biasing experiments.

After the biasing, the modules were brought back to the flasher system in the dark and cooled to 25°C. IV characteristics at STC were measured as soon as possible (usually around ten to twenty minutes after removing the bias). The protocol 'initial flash - biasing at elevated temperatures - post-biasing flash' is considered one stabilization cycle, with three cycles at the same temperature and bias current completed for each round of biasing. At the end of each round (= after three cycles of biasing) another EL image was taken, using the settings of table 3.3 to see if any damage was done to the modules during biasing.

3.5 Computational analysis

The raw IV-data extracted from both the small sun simulator and the IV-flasher were refined with the help of Python [47]. Self-written programs were used for visualization of data, production of plots and fitting of parameters via the JMAK equation (see also section 2.9) and generation of Arrhenius curves.

3.5.1 Fitting via JMAK and Arrhenius

For considerations of dimensionality and the nature of the microscopic processes happening in the solar module samples during biasing, the data was fitted for power over time via the Johnson-Mehl-Avrami-Kolmogorov equation (described in theory in section 2.9) using a function of the shape

$$f(t) = c_0 + c_1 \cdot e^{(-t/\tau)^n} \tag{3.2}$$

and varying parameters c_0, c_1, τ and n with the help of Python's Scipy library.

To make an estimation on whether the underlying microscopic process during power stabilization was (only) thermally activated, this data was then fitted with an Arrhenius curve (for theoretical details see section 2.9.1). The plots are half-logarithmic with the logarithm of one variable (either n or τ) found in the JMAK fit, and plotted over the inverse temperature (1000/T [K]).

3.6 Errors

Since all measurements were interpreted only in direct relation to each other (as absolute values) statistical errors can be neglected. Moreover the measuring flashers are calibrated each day with a reference module with an accuracy of $\approx \pm 0.001$ Ampere, further negating the effects of errors.
Any errors in the data come from the electrical error of 0.1% in voltage and 0.1% in current measurements (or errors of power at 0.14%), or from systemic errors. Overall, a resolution of errors caused by the measuring devices can be estimated to be around $\pm 0.3 - 0.6\%$.
Due to the nature and their small size (compared to our absolute values) of these errors, they were mostly neglected here.

Errorbars are only used for the presented JMAK fits, with a $\pm 1\%$ errorbar. These are used explain why even if the fitting curve does not go directly through all datapoints, the fit can still be valid if it goes through the errorbars.

4 Results

In this chapter the results of the experiments are presented, including plots and fits for a number of important electrical parameters, as well as electroluminescence images of the full scale modules. Note that not every plot will be presented in this chapter and that this is merely a selection of representative data. All plots not featured here can be found in appendices A and B. The discussion of the presented results and their meaning for future projects can be found in the next chapter (chapter 5, Discussion and Outlook).
The results are sorted by module type (mini modules in section 4.1 and full scale modules in section 4.2).

4.1 CZTS mini modules

Here all results concerning the investigated CZTS minimodules will be presented, from an overview of the behavior of all electrical parameters in a single round of bias (section 4.1.1), to an overview of a representative sample's behavior in both rounds of biasing (section 4.1.2), followed by an overview of notable differing behavior in section 4.1.3. A complete list of numerical values of maximum power output P_{max} can be found in section 4.1.4. Finally, sections 4.1.5 and 4.1.6 present the JMAK fits and Arrhenius plots extracted from the experimental data.

4.1.1 CZTS mini modules: All electrical parameters

Figures 4.1, 4.2 and 4.3 give an overview of the relative changes in all electrical parameters of one representative sample (M2064b, Round 2) during the entire biasing procedure.

4.1.2 CZTS mini modules: representative results

The following section features a series of plots for both rounds of biasing of one representative CZTS mini module (sample M2063l). For most samples, their behavior was similar to this. A few exceptions will be noted and described in section 5.1.
The first plot (figure 4.4) shows the maximum power output at the end of each biasing step for both rounds (round 1: 50°C and 1/3 I_{sc}, round 2: 65°C and 1/3 I_{sc}), normalized to the initial value of each round. Especially the second round of biasing (lighter violet curve) shows the typical behavior of an order transition, with a slow start, rapid change and plateau in the stable condition.
The second plot (figure 4.5) shows the I_{sc}, the third (figure 4.6 the V_{oc} and the fourth (figure 4.7) the fill factor of the same sample.
These four plots played an important role in finding the most promising temperature/bias

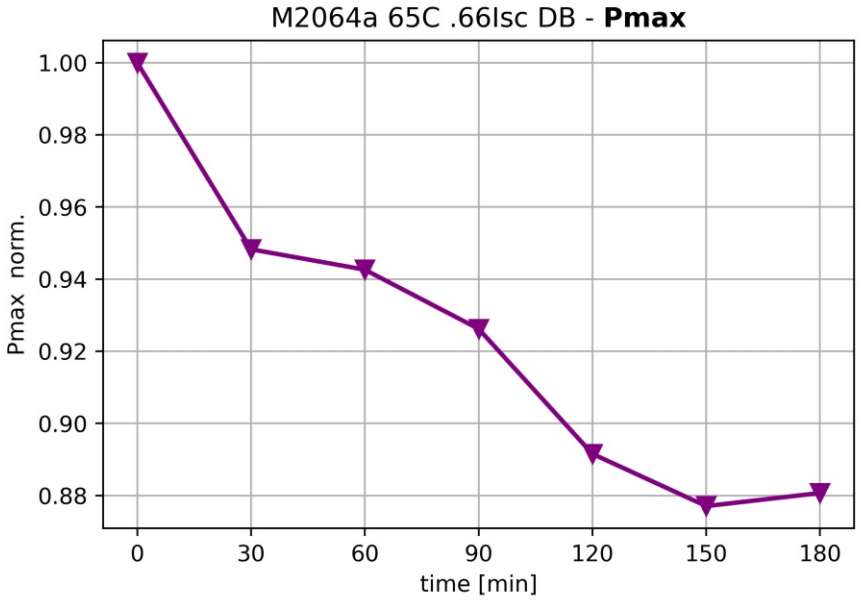

(a) Maximum power Pmax

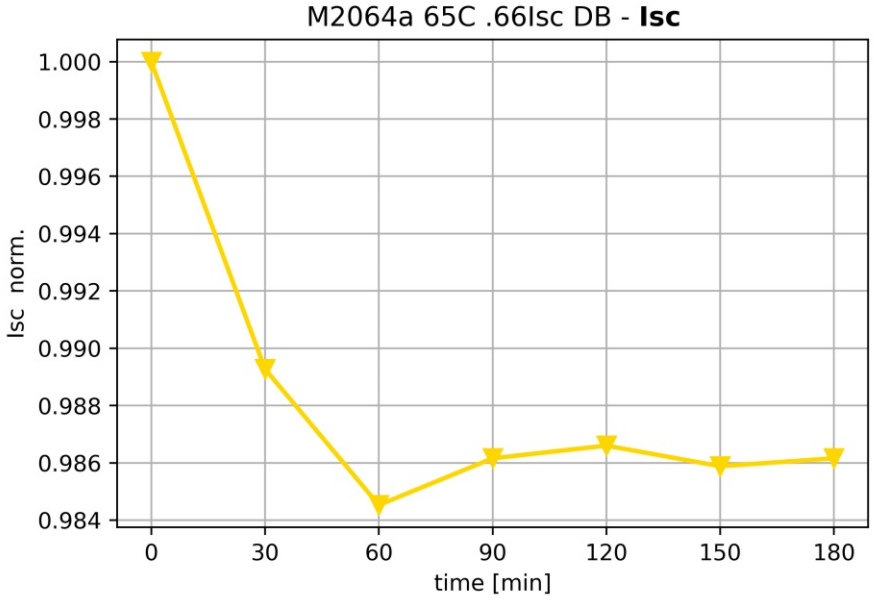

(b) Short circuit current (Isc)

Figure 4.1: Relative change of maximum power output (a) and short circuit current (b) of sample in six cycles of dark bias measurements at 65°C and 2/3 of initial Isc current as bias. Stabilization is reached in the last three cycles.

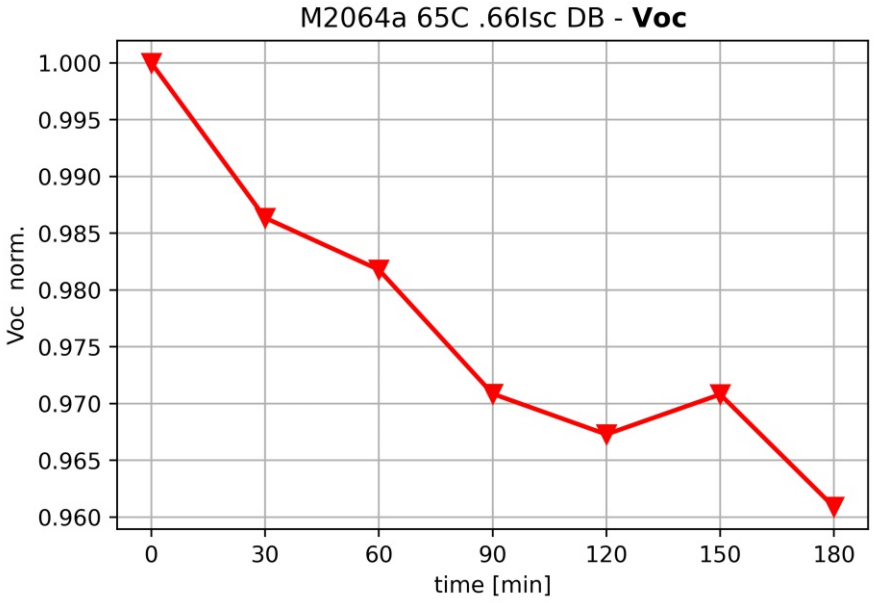

(a) Open circuit voltage (Voc)

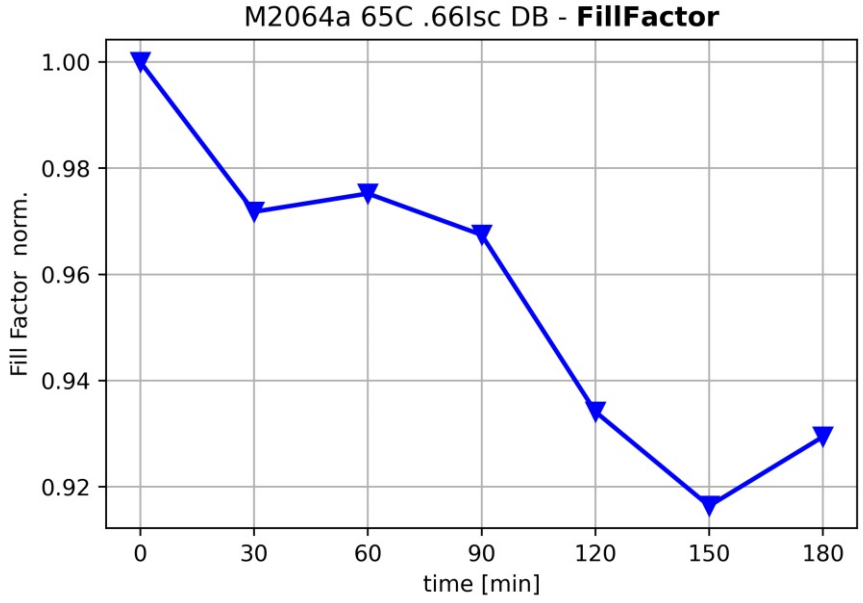

(b) Fill factor (FF)

Figure 4.2: Relative change of open circuit voltage (a) and fill factor (b) of sample M2064a.

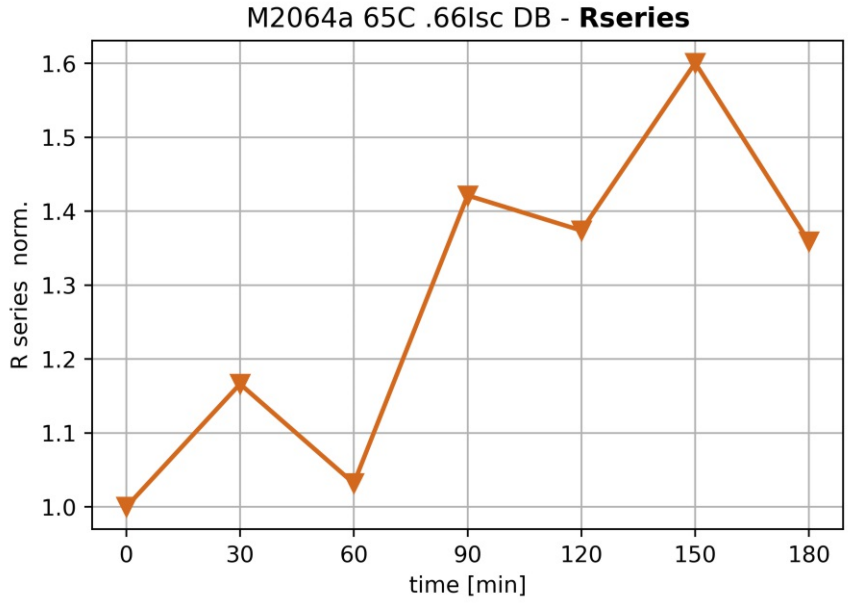

(a) Series resistance (Rseries)

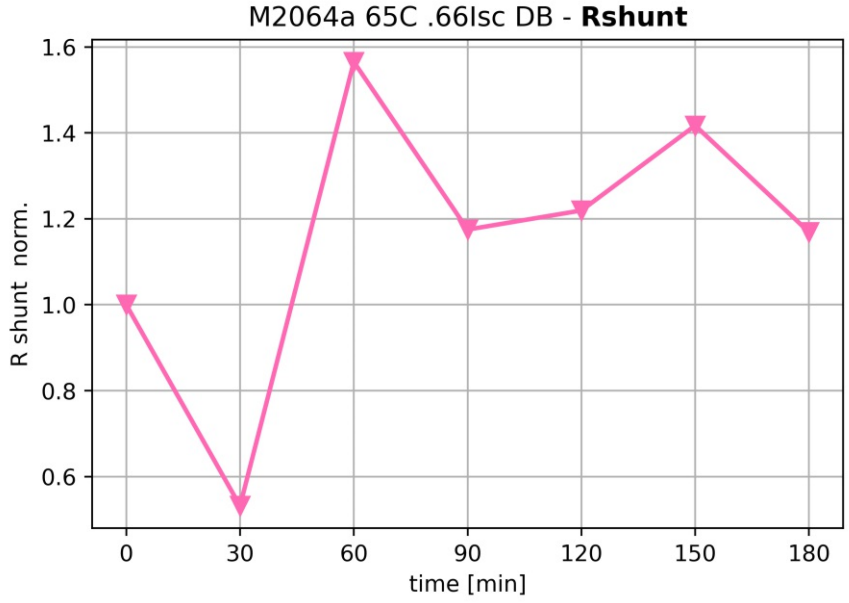

(b) Shunt resistance (Rshunt)

Figure 4.3: Relative change of series (a) and shunt resistances (b) of sample M2064a

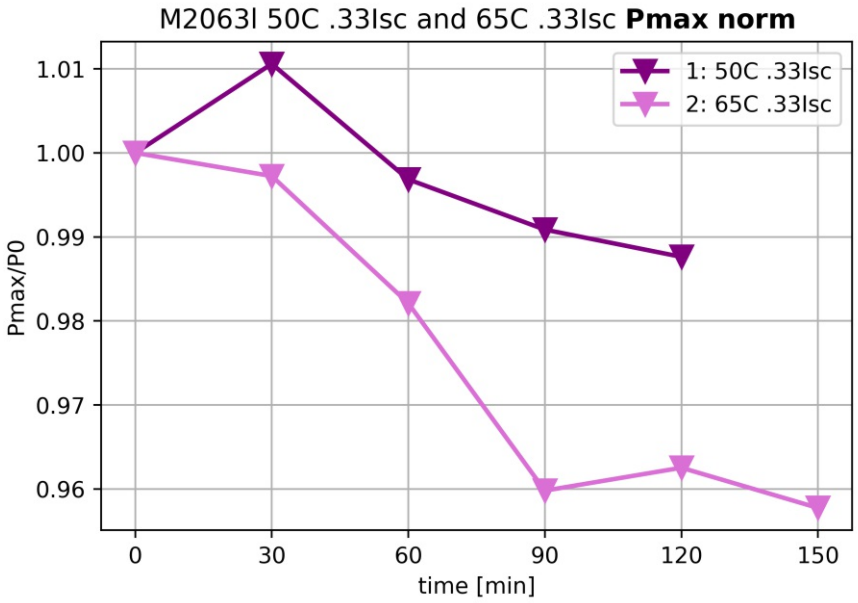

Figure 4.4: Behavior of representative CZTS minimodule in two rounds of biasing (route B1), P_{max} behavior. The darker violet curve is the data for the first round of biasing (B), the lighter violet is the second round (B1).

combinations for the full scale module measurements. The plots for all CZTS mini modules can be found in appendix A.

4.1.3 CZTS mini modules: divergent results

Notable exceptions to the representative behavior described in the previous section was seen in the following samples:

M1853d

Sample M1853d reached no saturation in its current and even made a significant increase in current after five hours in bias, as can be seen in figure 4.8. This behavior also means that no stabilization of P_{max} was achieved for the sample.
This is a previously known issue of these CZTS modules that will be discussed in the results.

M2064a

As can be seen in figure 4.9, the short circuit current of sample M2064a rose by $\approx +2\%$ in the first round of biasing. At the same time, the fill factor stabilized.
The possible indications of these phenomena will be discussed in the next chapter.

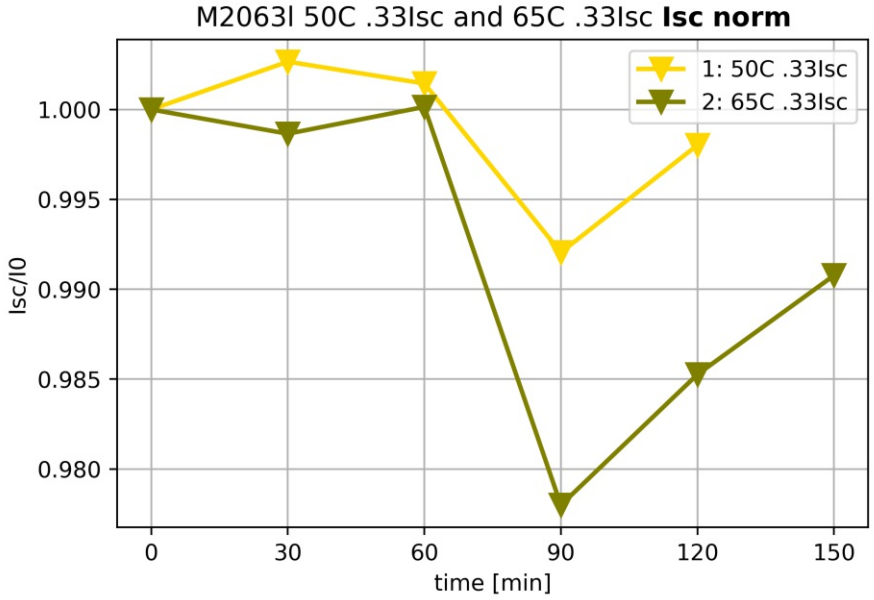

Figure 4.5: Behavior of representative CZTS minimodule in two rounds of biasing (route B1). The short circuit current (I_{sc}) exhibits only small changes during biasing, with a deviation of $\pm < 1\%$ in the first round and around $\pm 2\%$ in the second round. .

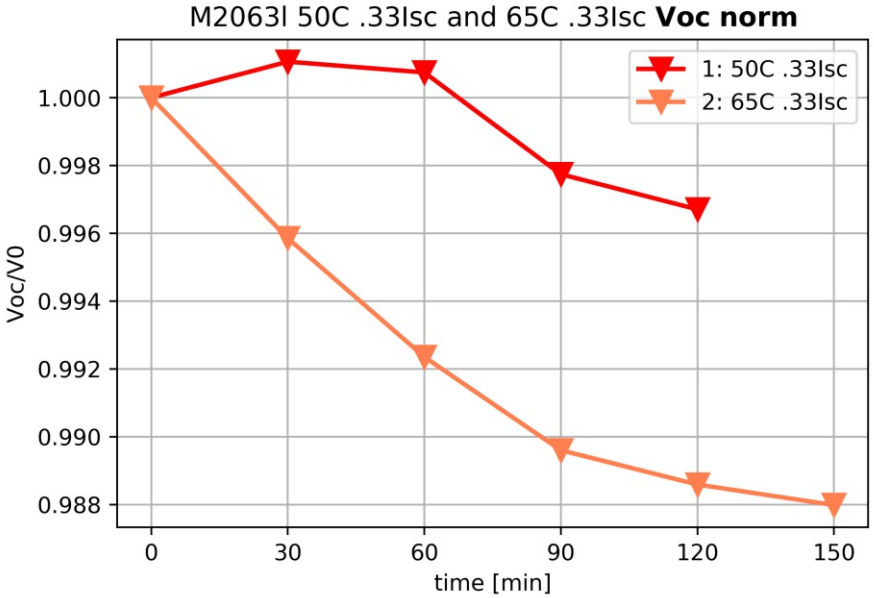

Figure 4.6: Behavior of representative CZTS minimodule in two rounds of biasing (route B1). The open circuit voltage (Voc) is very stable in the first round (B, darker red curve) with a deviation of only $< \pm 0.4\%$. In the second round (B1, light orange curve) Voc falls faster and longer, but is still small with a stabilization at around 98.8% of the initial value.

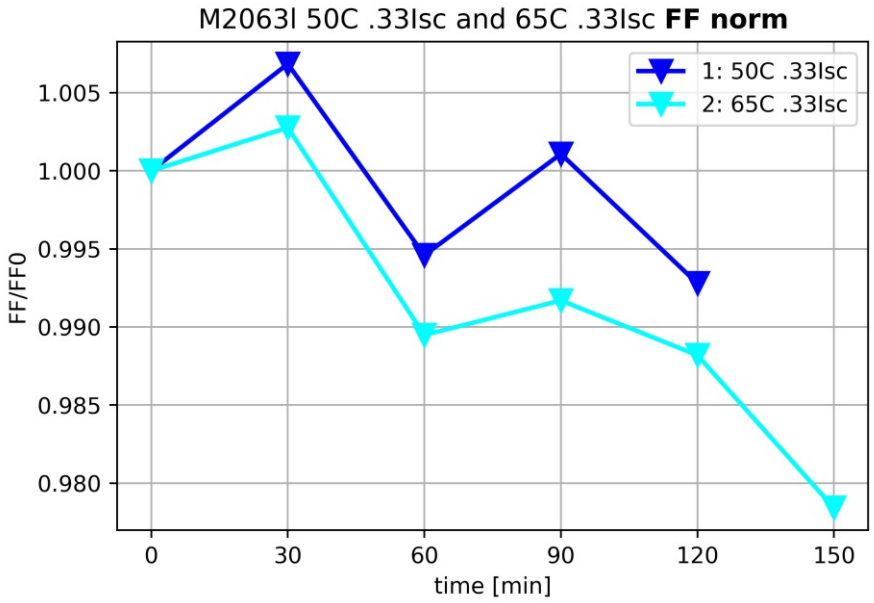

Figure 4.7: Behavior of representative CZTS minimodule in two rounds of biasing (route B1). The fill factor shows irregular behavior, but a decrease compared to the initial value in both rounds of biasing.

4.1.4 Change of P_{max}

The following tables (4.1, 4.2 and 4.3) contain the absolute numeric values of measured power output for CZTS minimodules in bias, as well as the amplitude of change in P_{max} in absolute numbers and as fraction of the initial value. Table 4.2 gives an overview of the changes in P_{max}, averaged by temperature, table 4.3 does the same averaged by biasing current.

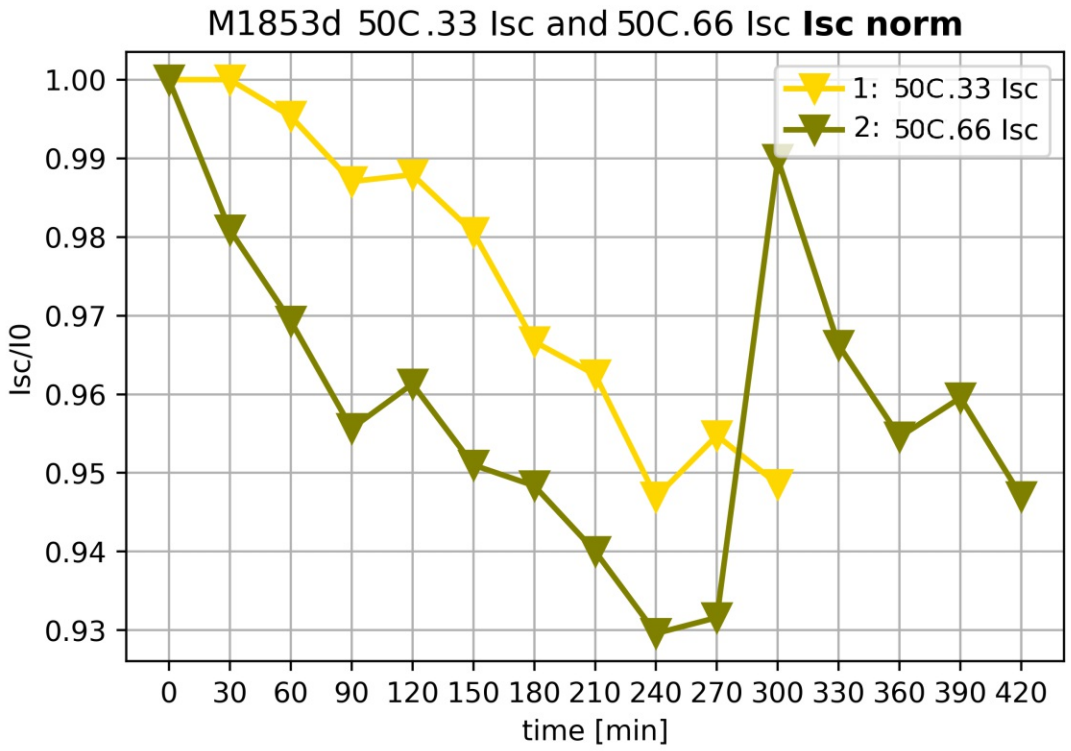

Figure 4.8: This plot of the short circuit current behavior of sample M1853d shows that the current never saturated. As explained in the text, this behavior has previously been seen in the manufacturer's CZTS modules and is attributed to a loss of backside contact.

4.1.5 JMAK fit parameters

For several of the samples (M2063g round 2, and both rounds of M2063i), JMAK fits were not possible at all, since the data was simply not representing a sigmoid curve. These samples were excluded from the following averaging process. Taking all successfully fitted samples (see table 4.4), we then averaged characteristic time τ and Avrami exponent n for all biasing temperatures (25, 50 and 65°C). The results can be found in table 4.5.
For some samples initial points (a long time before stabilization) had to be removed to allow a meaningful fit.

Table 4.5 contains the averaged Avrami exponents $\overline{n}$ and characteristic times $\overline{\tau}$ of .

Representative plots of normalized maximum power output over the time fitted with a function $f(t)$ from equation 3.2 can be found in the following figures (4.10 and 4.11).

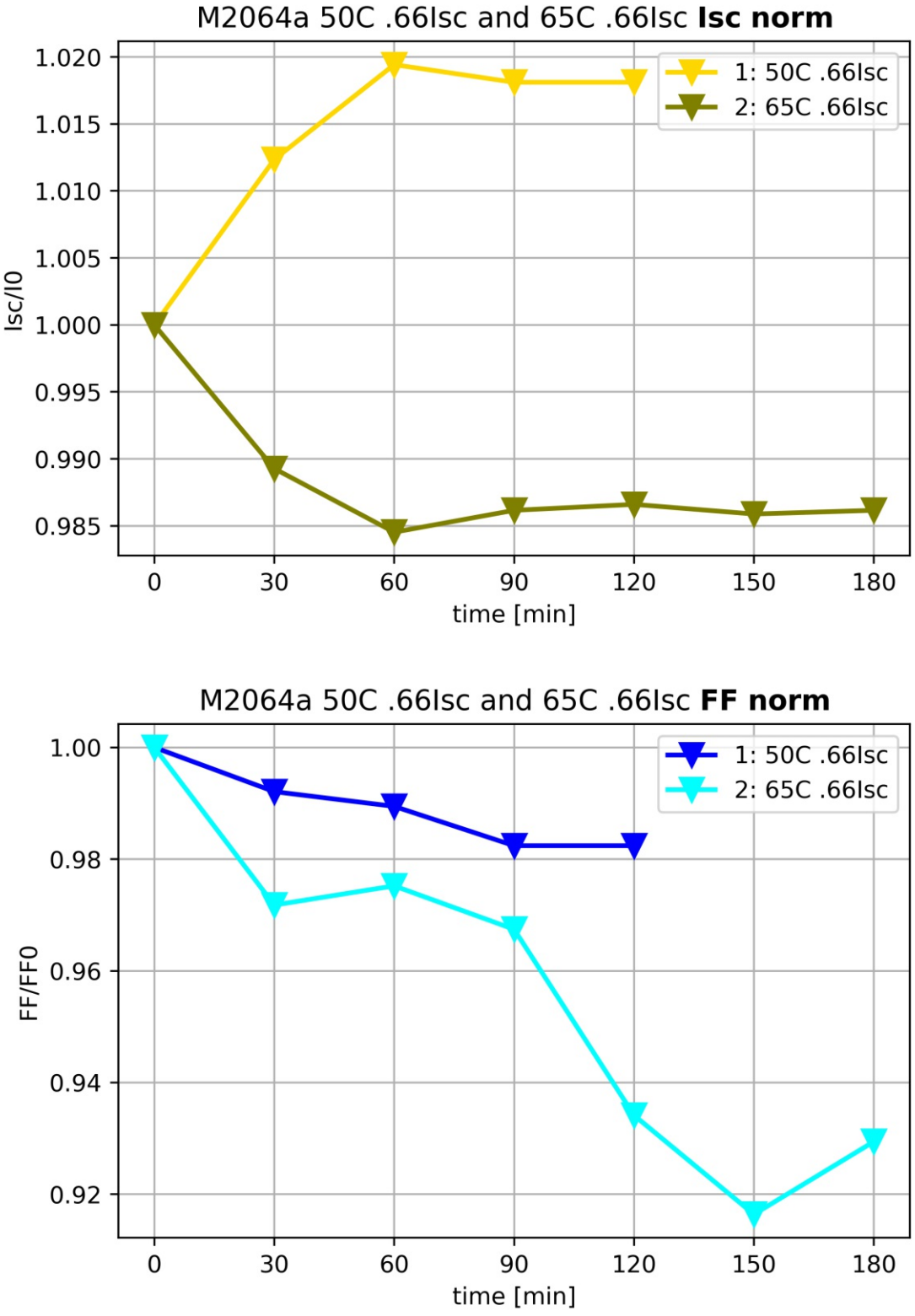

Figure 4.9: This plot of the short circuit current and fill factor behavior of sample M2064a shows that the current rose in the first round of biasing (bright yellow) while the fill factor stabilized.

Amplitude of P_{max}

sample	initial P_{max} [W]	ΔP_{max} [W]	Δ P_{max} [%]	stab. [y/n]
M1853a 25 .33	0.2704	+0.0060	+2.24	y
M1853a 50 .33	0.2727	-0.0215	-7.89	n
M1853b 25 .33	0.2972	-0.0055	-1.85	y
M1853b 50 .33	0.2657	-0.0117	-4.41	y
M1853c 25 .33	0.3285	-0.0121	-3.68	y
M1853c 50 .66	0.3018	-0.0178	-6.89	y
M1853d 50 .33	0.2253	-0.0161	-7.17	y
M1853d 50 .66	0.2191	-0.0446	-20.34	y
M2063d 25 .33	0.0961	-0.0075	-7.75	n
M2063d 50 .33	0.0846	-0.0125	-14.73	n
M2063g 25 .33	0.0635	-0.0283	-44.52	n
M2063g 50 .66	0.0603	-0.0047	-7.85	y
M2063i 50 .33	0.0799	+0.0012	+1.50	y
M2063i 50 .66	0.0777	-0.0029	-3.78	y
M2063k 50 .33	0.0966	-0.0011	-1.12	y
M2063k 65 .33	0.0960	-0.0063	-6.56	y
M2063l 50 .33	0.0922	-0.0011	-1.24	y
M2063l 65 .33	0.0910	-0.0038	-4.23	y
M2063n 50 .66	0.1012	-0.0009	-0.86	y
M2063n 50 1	0.1015	-0.0027	-1.99	y
M2064a 50 .66	0.4209	-0.0027	-0.64	y
M2064a 65 .66	0.4145	-0.0510	-12.29	y
M2064b 50 .66	0.4248	-0.0056	-1.33	y
M2064b 50 1	0.4163	-0.0147	-3.53	y

Table 4.1: Numeric values of initial power output in CZTS minimodules, as well as amplitude change in absolute numbers and as percentile. (Errors for these values are around $\pm 0.14\%$ per measurement.)
The last column ("stab. [y/n]") gives an overview of whether it was possible to stabilize the given sample.

Especially in the first three figures(4.10 (a) and (b) and 4.11 (a)), data points show strong resemblance to sigmoid shapes, as fitted with the JMAK method (see section 2.9 for theory and 3.5.1 for application to this data). The values for n and τ were obtained via a fitting program written in Python, and sometimes refined manually.
The manual refinement was done as follows: For some samples (especially those with few datapoints) a simultaneous fitting of n and τ sometimes led to unrealistic values of the parameters and overall "bad" fits. It can be assumed that within the same sample n varies mainly with changes in bias current, and τ with changes in temperature. The fitted parameters from one round of biasing should also be similar for one module, depending if temperature or bias current is changed between rounds. Considering this, one parameter

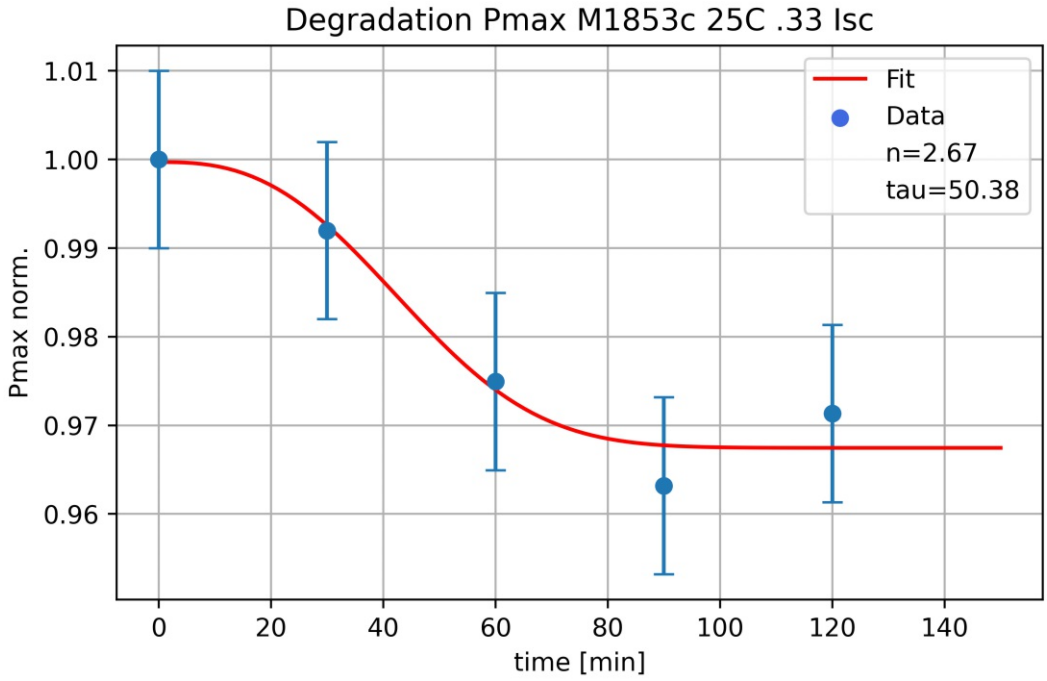

(a) JMAK fit (n=2.67, τ=50.38) for maximum power output of sample M1853c during biasing at 25°C and 1/3 I_{sc}.

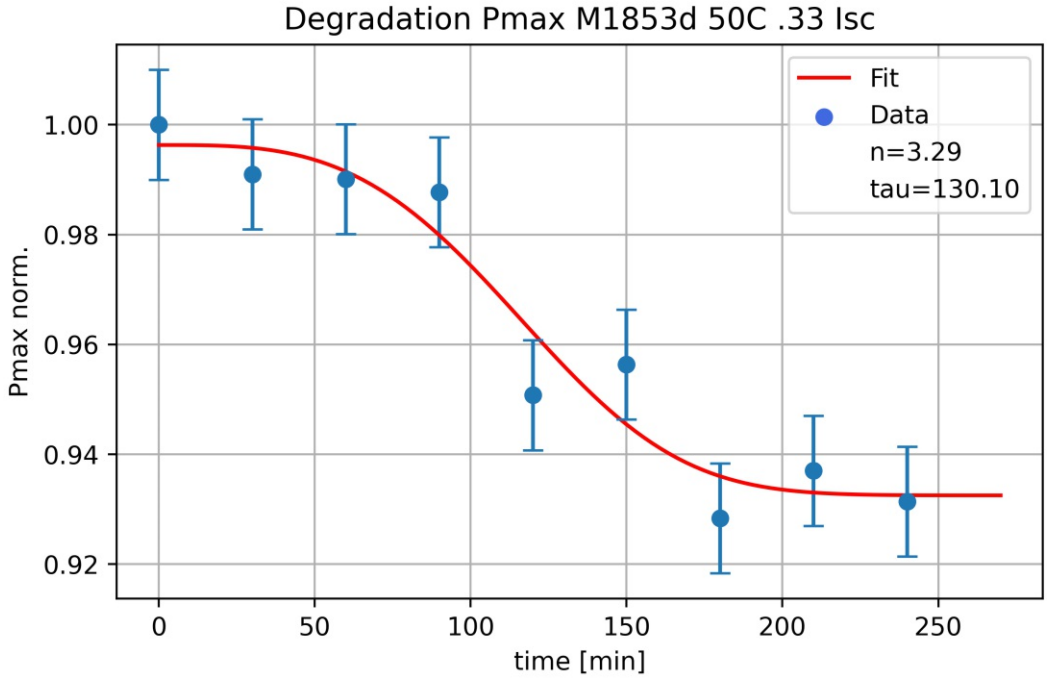

(b) JMAK fit (n=3.29, τ=130.10) for maximum power output of sample M1853d during biasing at 50°C and 1/3 I_{sc}.

Figure 4.10: JMAK fit samples M1853c 25 .33 (a) and M1853d 50 .33 (b).

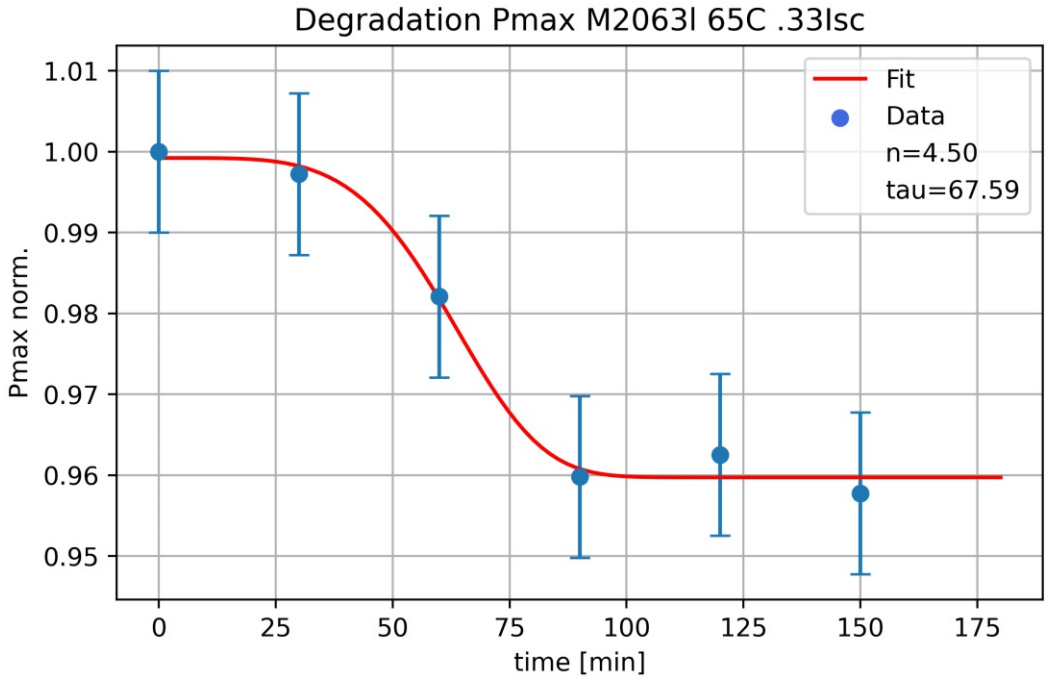

(a) JMAK fit (n=4.50, τ=67.59) for maximum power output of sample M1853c during biasing at 25°C and 1/3 I_{sc}.

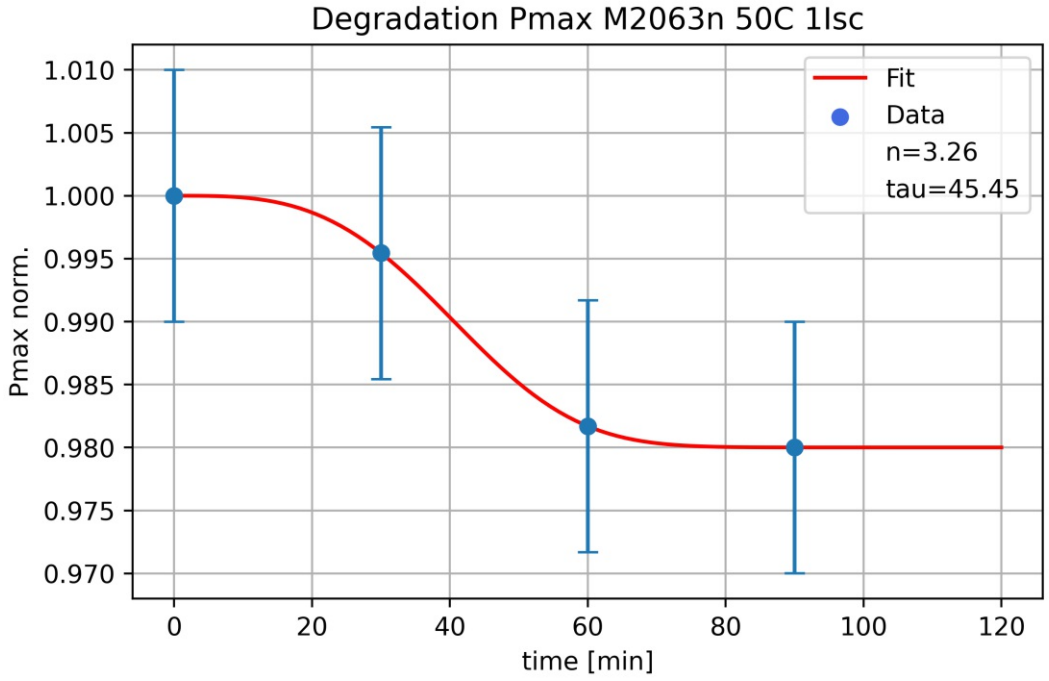

(b) JMAK fit (n=3.26, τ=45.45) for maximum power output of sample M1853d during biasing at 50°C and 1 I_{sc}.

Figure 4.11: JMAK fit samples M2063l 65 .33 (a) and M2063n 50 1 (b).

Temperature [°C]	average change [%]
25	2.59*
50	5.267
65	7.694

Table 4.2: Average change of maximum power output of CZTS minimodules, avereraged by temperature. * in this figure, samples M2063d and M2063g were excluded due to their large power loss that was most likely caused by bad manufacturing.

Bias Current [fraction of I_{sc}]	average change [%]
0.33	7.777
0.66	6.624
1	2.765

Table 4.3: Average change of maximum power output of CZTS minimodules, avereraged by applied bias current (as fraction of I_{sc}).

(n or τ) was taken from a good fit of the same sample and used as fixed parameter in the bad fit. Thus letting loose only one parameter at a time, much better fits could be achieved.
In figure 4.11 (b) the sigmoid shape is not as pronounced, especially since there are only four datapoints and the change of ΔP is quite small for the whole intervall. This is the case for several of the samples (mostly at higher temperatures and biasing currents), all fits can be found in appendix A.

4.1.6 Arrhenius behavior

As explained in section 3.5.1, an Arrhenius plot of the logarithmized averaged variable (n and τ) on the y-axis and inverse temperature (1000/T [K]) on the x-axis was done. Plotting the averaged variables from table 4.5 led to figures 4.12.

This linear fit seems justifiably good to approximate the data, the implications of this will be discussed in section 5.1.3.

JMAK fit parameters (all samples)

sample	**temp.** [°C]	**bias** [$\mathbf{I_{sc}}$]	**best fit** τ	**best fit** n
M1853a	25	1/3	71.61	1.50
M1853a	50	1/3	69.230	1.50
M1853b	25	1/3	30.93	3.00
M1853b	50	1/3	16.45	3.00
M1853c	25	1/3	50.38	2.67
M1853c	50	2/3	28.91	2.67
M1853d	50	1/3	130.1	3.29
M1853d	50	2/3	47.29	3.00
M2063d	25	1/3	12.00	3.50
M2063k	50	1/3	20.61	3.00
M2063g	25	1/3	7.78	2.70
M2063g	50	1/3	no fit	no fit
M2063i	50	1/3	no fit	no fit
M2063i	50	2/3	no fit	no fit
M2063k	50	1/3	72.24	2.95
M2063k	65	1/3	82.35	2.95
M2063l	50	1/3	73.14	3.50
M2063l	65	1/3	67.59	4.50
M2063n	50	2/3	45.45	3.26
M2063n	50	1	45.45	3.26
M2064a	65	2/3	55.00	3.00
M2064a	65	2/3	90.84	1.50
M2064b	50	2/3	59.01	2.52
M2064b	50	1	45.91	1.80

Table 4.4: Complete list of all fitted parameters for CZTS mini module samples.

temperature [°C]	**characteristic time** $\overline{\tau}$ [s^{-1}]	**Avrami exponent** $\overline{n}$
25	34.54	2.67
50	54.52	2.83
65	80.26	2.98

Table 4.5: Average characeristic time $\overline{\tau}$ and average Avrami exponent $\overline{n}$ for all CZTS mini module samples with good JMAK behavior, sorted and averaged by temperature during biasing. Calculated from table 4.4.

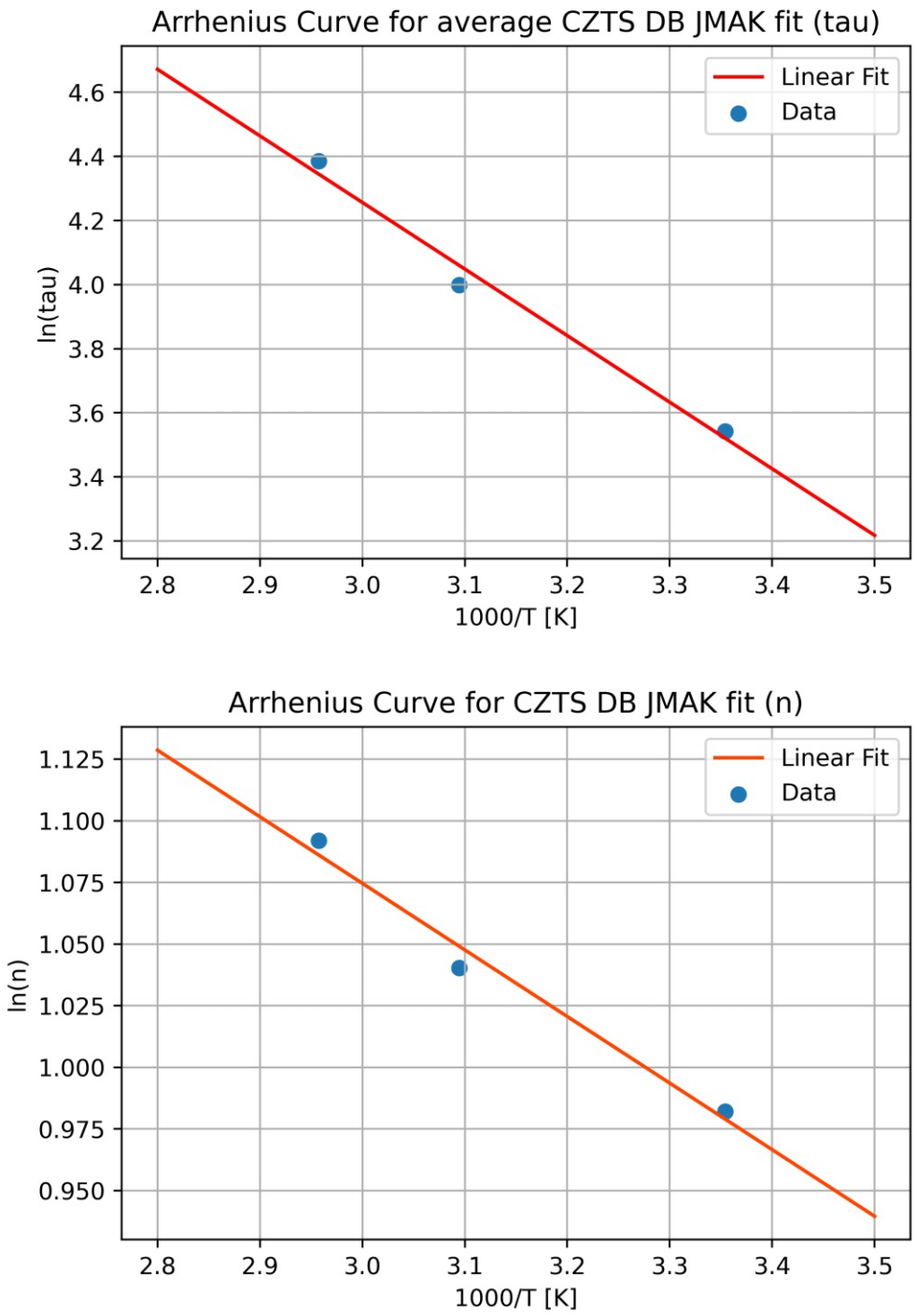

Figure 4.12: Arrhenius behavior of characteristic time τ and Avrami exponent n averaged over temperature during biasing.

4.2 Full scale CIGS and mono-c-Si modules

The following section contains a representative overview of all results for the full scale CIGS and mono-c-Si modules investigated. For details on the measuring procedure, see section 3.4.3.

4.2.1 CIGS: All electrical parameters

Figure 4.13 gives an overview of electrical parameters during biasing of full scale CIGS modules.
$\mathbf{P}_{max}$ shows a rise for all modules and all temperatures compared to the initial value. The rise is about twice as large for CIGS 1 as it is for CIGS 2.
The **fill factor** behaves very similarly to P_{max}, rising for every series of measurements, more for CIGS 1 and less for CIGS 2.
While the $\mathbf{I}_{sc}$ shows no clear trend, $\mathbf{I}_{mpp}$ (at maximum power point) exhibits the same trend as P_{max} and fill factor.
The voltage $\mathbf{V}_{oc}$ of the CIGS modules shows a trend of annealing at lower temperatures (50°C and 65°C) and degradation for higher temperatures (75°C). It is be noted that the scale of changes is very small ($< \pm 1\%$), thus happening on a scale smaller than the resolution of the measurements.
$\mathbf{V}_{mpp}$ shows again a similar behavior to P_{max}, if less pronounced.

4.2.2 c-Si: All electrical parameters

While all plots for c-Si full scale modules are presented in figure 4.14, note that the changes are so small, they are barely outside of the error for these measurements. That means, all cSi modules were basically stable in all parameters at all times.

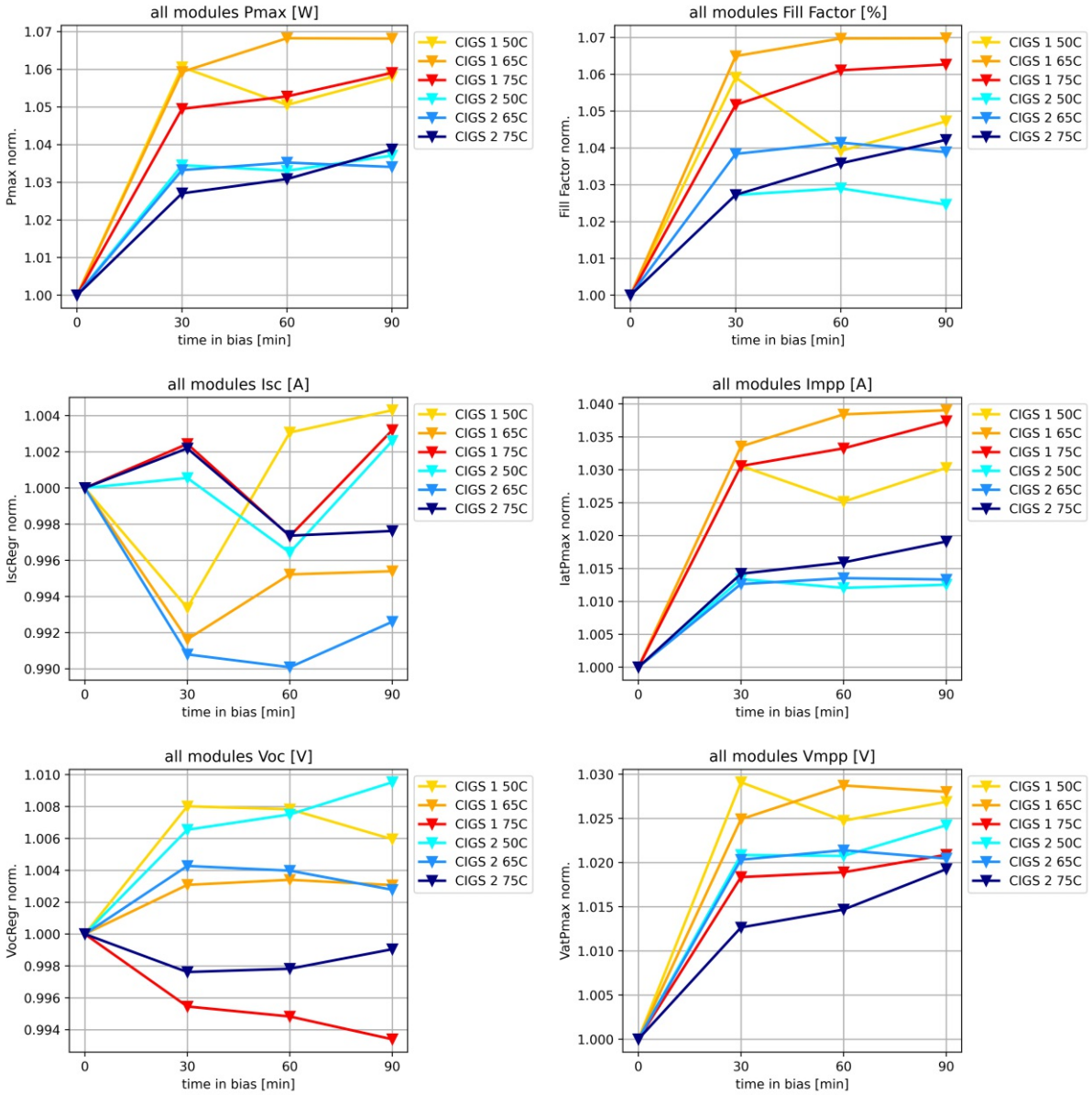

Figure 4.13: Overview of all electrical parameters of the investigated full scale CIGS modules.

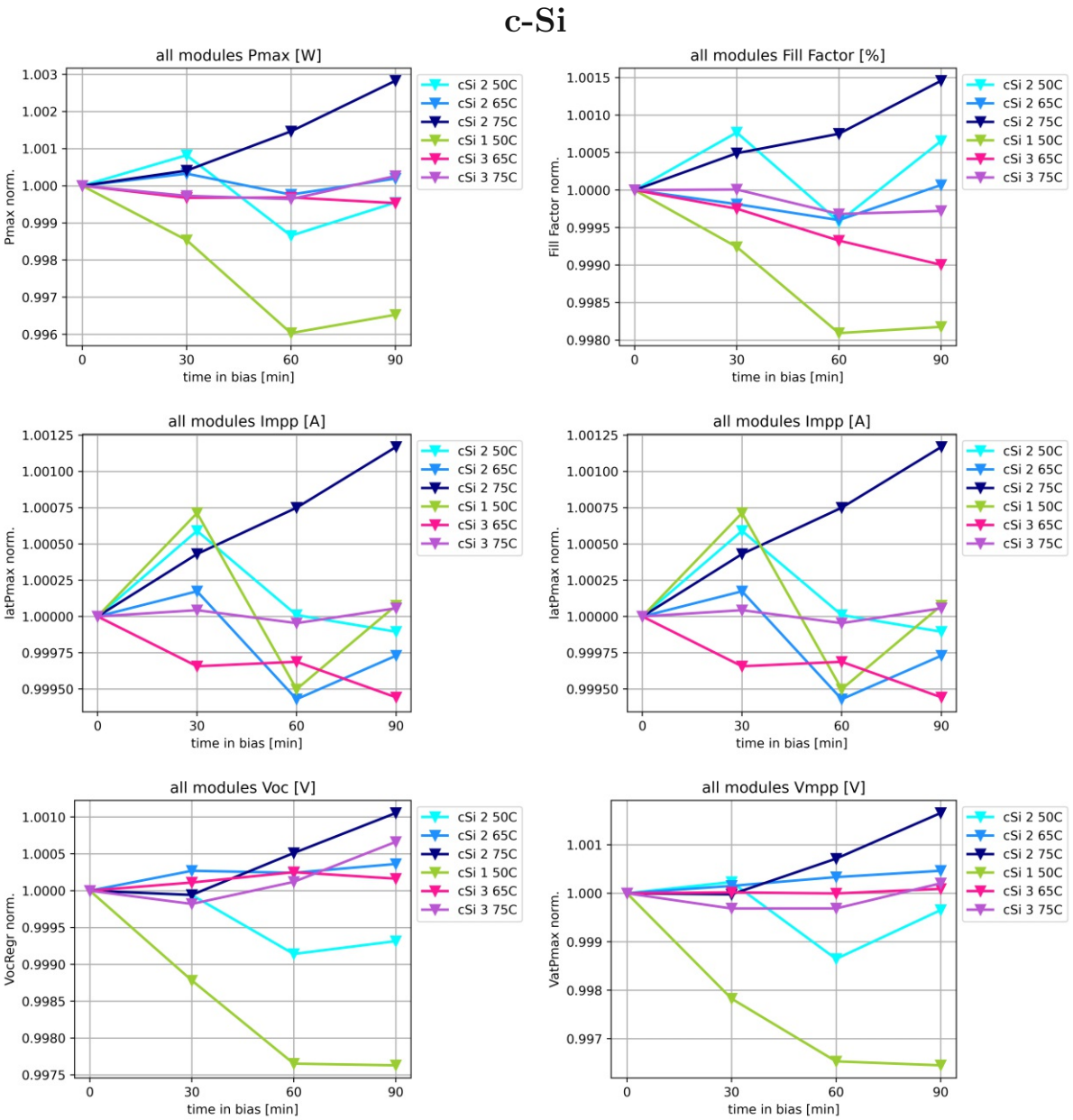

Figure 4.14: Overview of all electrical parameters of the investigated full scale c-Si modules.

Amplitude of P_{max}

sample	initial P_{max} [W]	amplitude P_{max} [W]	amplitude P_{max} [%]
CIGS 1 50C	142.85	+8.65	+6.06
CIGS 1 65C	142.00	+9.69	+6.82
CIGS 1 75C	143.50	+8.47	+5.91
CIGS 2 50C	149.97	+5.56	+3.71
CIGS 2 65C	149.43	+5.26	+3.52
CIGS 2 75C	149.60	+5.79	+3.87
cSi 2 50C	306.03	-0.41	-0.14
cSi 2 65C	305.77	+0.10	+0.03
cSi 2 75C	305.61	+0.86	+0.28
cSi 1 50C	308.09	-1.22	-0.40
cSi 3 65C	305.86	-0.14	-0.05
cSi 3 75C	305.94	-0.11	-0.04

Table 4.6: Numeric values of initial power output in CIGS and cSi full scale modules, as well as amplitude change in absolute numbers and as percentile. (Errors for these values are around ±0.1% per measurement.)

Temperature [°C]	CIGS: average change [%]	c-Si: average change [%]
50	4.88	0.27
65	5.17	0.04
75	4.89	0.16

Table 4.7: Average change of maximum power output of full scale modules, averaged by temperature.

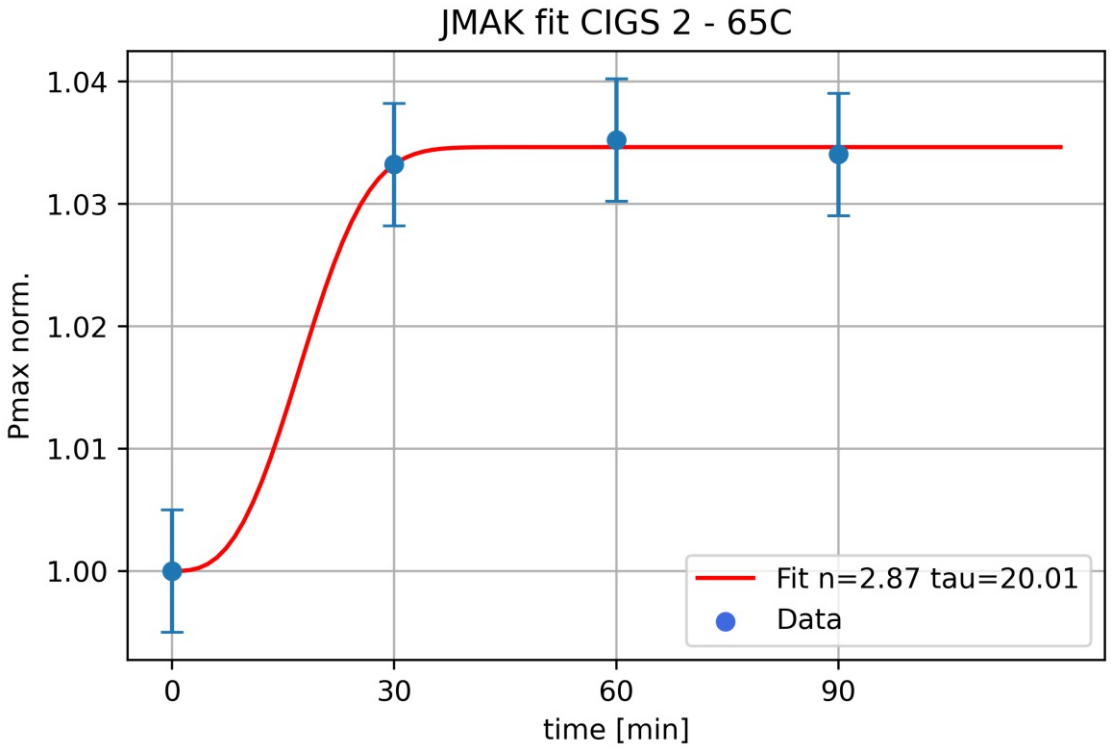

Figure 4.15: JMAK fit for CIGS 2 after 65°C bias round.

4.2.3 Full scale: JMAK fit parameters

JMAK fits for full scale modules were made more difficult by the small number of measurements (only four per sample). For c-Si modules, JMAK fits were not feasible since changes in parameters were far too small.
For CIGS modules, JMAK fits were made, even though they show an increase in power rather than the decrease expected from CZTS results (see section 4.1.5).
One exemplary fit will be presented in figure 4.15 and an overview of fitting parameters n and τ in table 4.4. In addition, table 4.9 contains the averaged values for τ, averaged by temperature.

4.2.4 Full scale: Arrhenius behavior

From table 4.9, an Arrhenius plot has been made for CIGS samples, as presented in figure 4.16.

4.2.5 Electroluminescence Images

To ensure no physical harm had been done to the modules tested in dark bias conditions, electroluminescence images were taken before the initial measurements and after the last

JMAK fit parameters (CIGS samples)

sample	**temperature** [°C]	**best fit** τ	**best fit** n
CIGS 1	50	12.00	3.28
CIGS 1	65	24.15	3.28
CIGS 1	75	23.71	3.28
CIGS 2	50	18.24	2.87
CIGS 2	65	20.01	2.87
CIGS2	75	26.03	2.87

Table 4.8: Complete list of all fitted parameters for full scale CIGS and c-Si modules, with an average $\overline{n}$ of 3.075 and an average $\overline{\tau}$ of 20.69.

temperature [°C]	$\overline{\tau}$
50	15.12
65	22.08
75	24.87

Table 4.9: Averaged τ for all CIGS modules, averaged by temperature during bias.

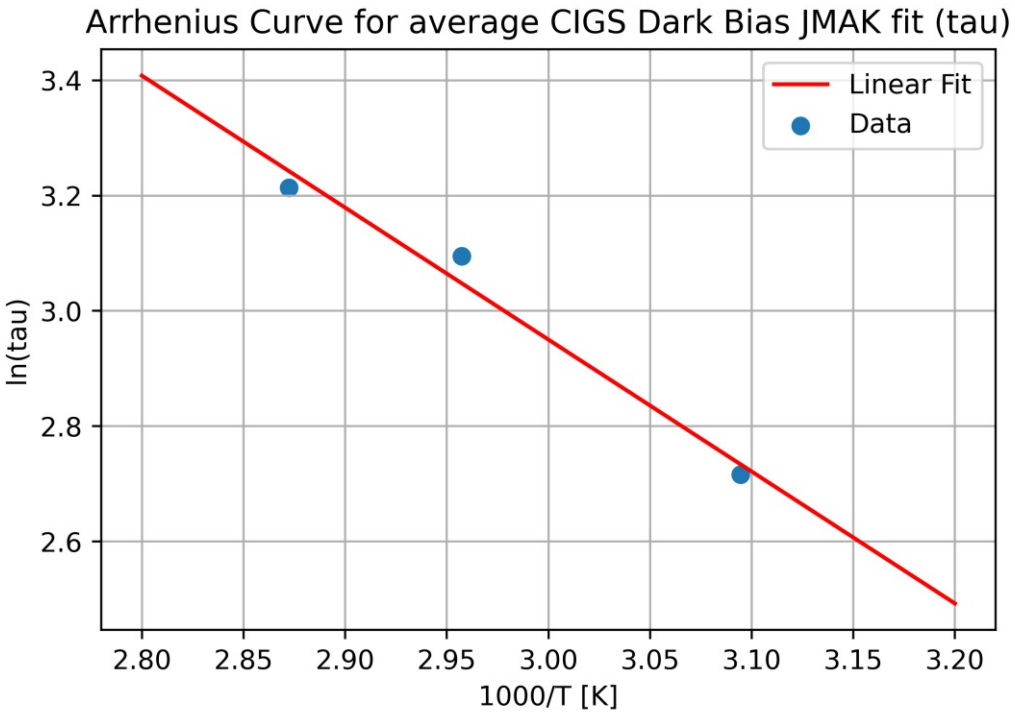

Figure 4.16: Arrhenius plot for CIGS modules.

measurement. They can be found side by side in figure 4.17.

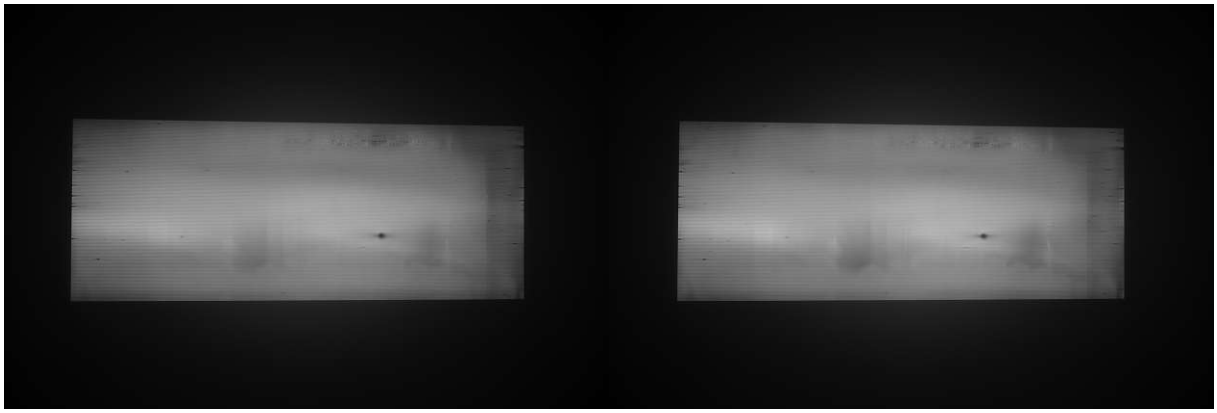

(a) CIGS 1 - before (b) CIGS 1 - after

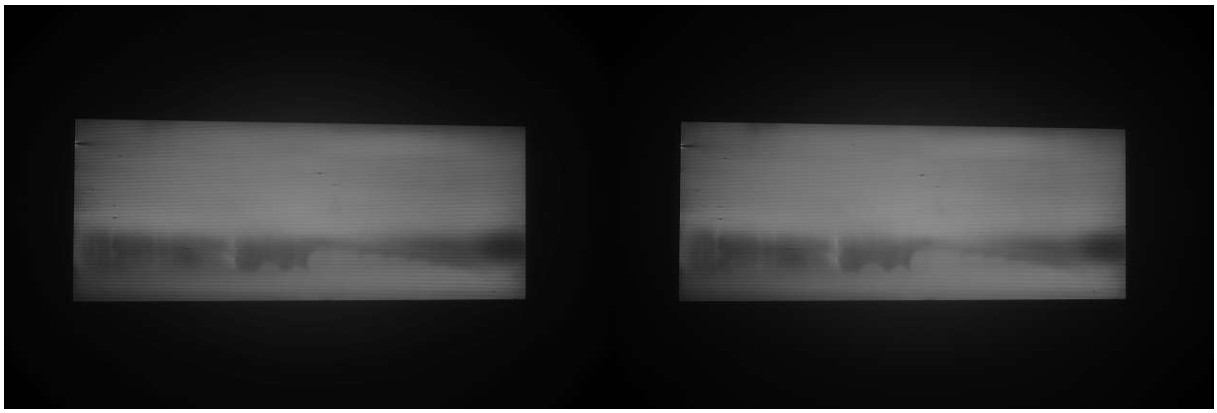

(c) CIGS 2 - before (d) CIGS 2 - after

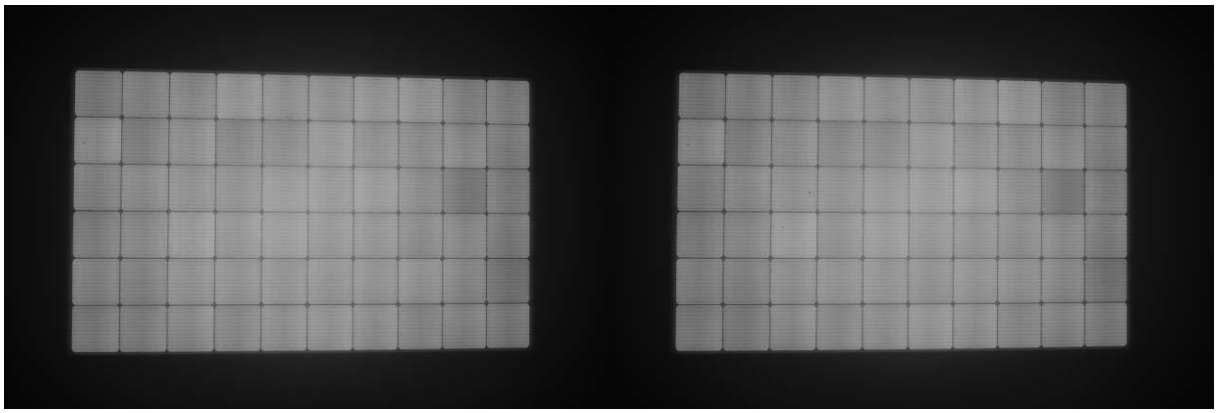

(e) c-Si 2 - before (f) c-Si 2 - after

Figure 4.17: Electroluminescence images of CIGS 1 and 2 as well as c-Si 2 modules before the initial experiments (left side, pictures a, c and e) compared to the an EL image after the final measurement of the series (right side, pictures b, d and f).

4.2.6 Comparison with outdoor exposure

For the comparison of the dark bias method with the currently standard outdoor exposure of modules, figure 4.18 contains side-by-side graphs of the behavior of the maximum output power in either stabilization process.
A large thanks goes to Diana Krainer, who provided the experimental data for the outdoor exposure.

4.2.7 Full scale: IV characteristics before and after dark bias

The change in the IV characteristics of examined modules was also investigated. For a visualization, consider figure 4.19 where the initial and final IV characteristic for one CIGS and one c-Si module are compared.
The CIGS module exhibits an improved characteristic after biasing (shown in red) compared to the initial characteristic (in blue). For the c-Si module, the characteristic did not change at all.

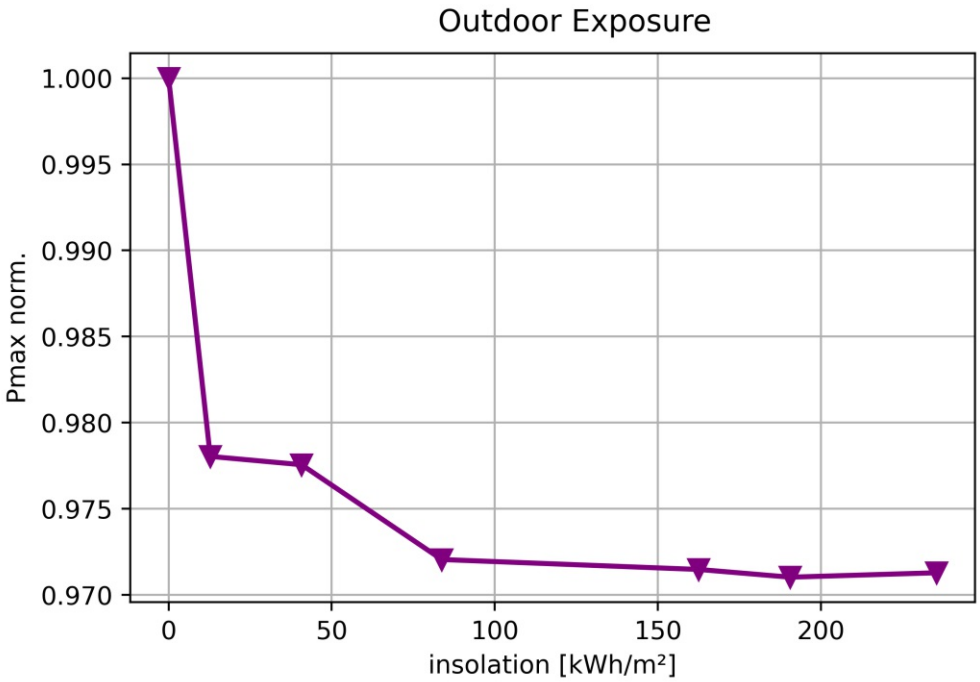

(a) Maximum power output of cSi full scale module in outdoor exposure.

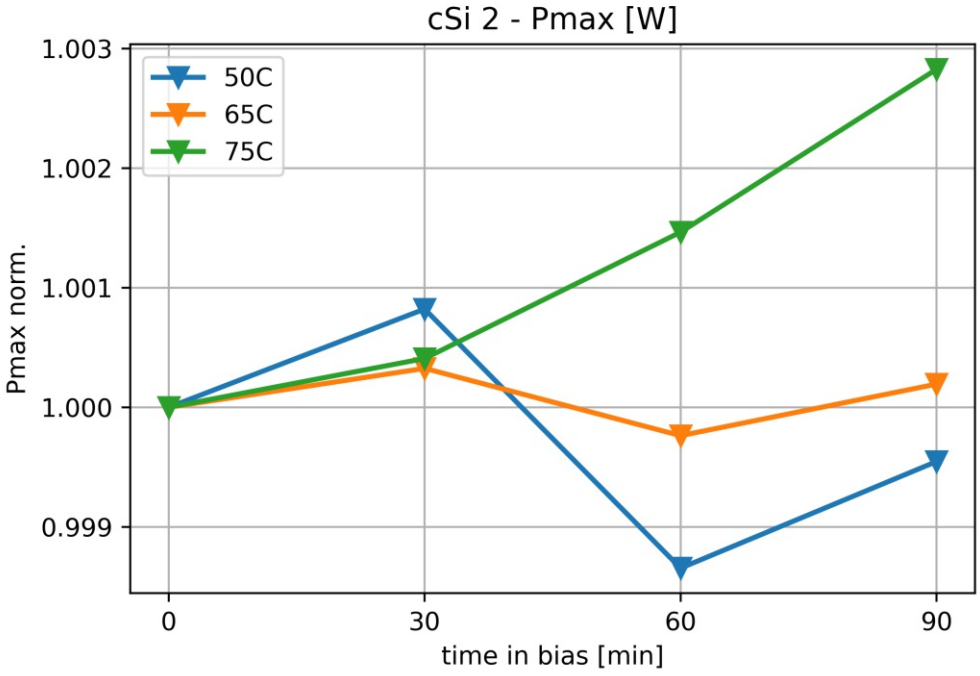

(b) Maximum power output of cSi full scale module in dark bias at 50, 65 and 75°C.

Figure 4.18: Side-by-side comparison of outdoor exposure and dark bias in cSi modules.

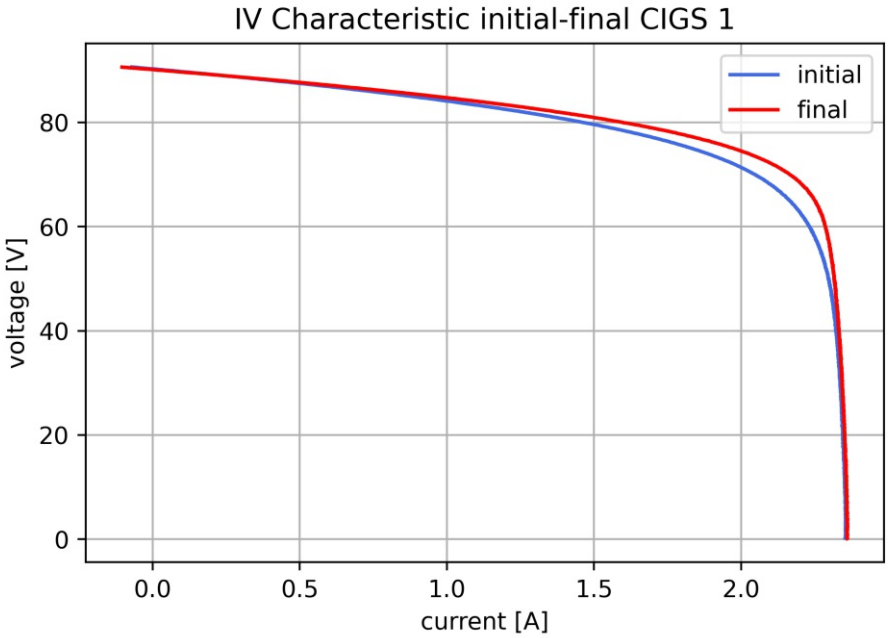

(a) CIGS

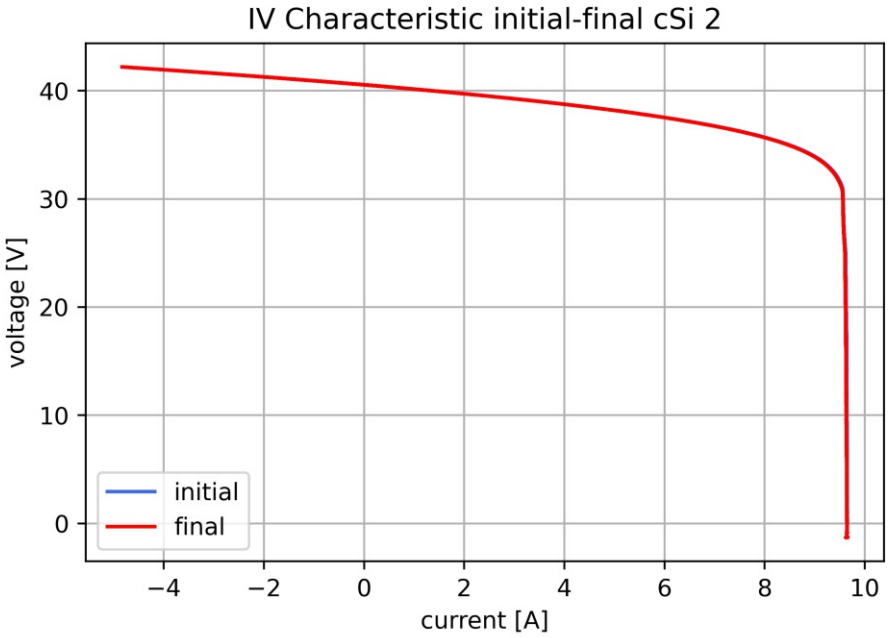

(b) c-Si

Figure 4.19: Comparison of initial and final IV characteristic of (a) CIGS and (b) c-Si modules. While the characteristic of the CIGS module improved slightly during biasing, the change in the c-Si module is not visible at all.

5 Discussion and Outlook

In this chapter the results from the previous sections are discussed and an outlook for similar experiments in the future is attempted.

What was observed in all experiments was an order-disorder transition, driven simultaneously by temperature (→ annealing) and injection of charge carriers via current bias. Such a transition is fueled by the changing number of point defects like vacancies or interstitial atoms or by changing grain boundaries.
Especially at lower temperatures, defects heal (arranging out-of-place atoms) and increase performance. When all defects are healed (either by dark bias experiments or before that) and more (thermal) energy is supplied, new defects start to form again (from breaking of weak bonds). Since the effects of additional energy in the system depends on the a-priori state of the system, the history of manufacturing and previous testing is so important.
By trying to stabilize the power output, these two mechanisms compete and it is attempted to find equilibrium.
Changes specifically in I_{sc} come mostly from decreased mobility and shortened diffusion length, the latter of which changes quickly with defects.

If one were to look at the samples microscopically, it would be possible to determine whether processes fueled by temperature or charge carriers are ordering or disodering processes. But for this work, only macroscopic indicators where considered, and the effects are interpreted indirectly via electrical output parameters.

5.1 CZTS mini modules

The particular characteristics of CZTS modules seen here come from their way of manufacturing. They are produced very fast and at high temperatures, healing out many defects in the material. When treated again with higher temperatures and bias current, the first observed changes are degrading in nature (introduction of new defects). This was also observed in the experiments here. Most samples exhibited initial degradation of all electrical parameters.
The other phenomenon encountered in this particular type of CZTS module (from this manufacturer) is the detachement of the semiconductor powder from the back contact observed in some samples.

5.1.1 CZTS: Influence of temperature and current bias on electrical parameters

As shown in section 4.1, especially by considering figures 4.4, 4.5, 4.6 and 4.7 (and their counterparts for other samples in the appendix), as well as tables 4.2 and 4.3 it can be deduced that - generally speaking:

- most CZTS samples exhibited the expected behavior: an initial decline in P_{max}, followed by a stabilization
- almost all CZTS samples could be stabilized
- higher temperatures caused larger average changes of P_{max} (table 4.2)
- larger bias currents caused smaller average changes of P_{max} (table 4.3
- older samples (batch M1853) exhibited larger initial losses in P_{max} than those fresh from production (batches M2063 and M2064)

Figure 5.1 contains a plot of maximum percentile changes for most electric parameters. The largest changes are in series resistance, followed by efficiency and P_{max}. The smallest changes appear to be in V_{OC}.

5.1.2 CZTS: P_{max} Stabilization

Under the temperature and bias ranges given for CZTS minimodules in chapter 3, power stabilization as defined by IEC 61646 was achieved for most samples. Figure 5.2 shows the final variation of P_{max} over the last three consecutive cycles of biasing, and it includes the 2% marker that was used to quantify "power stabilization" according to the IEC standard.
Only samples M1853a 50C .33 Isc, M2063d 25C .33 Isc, M2063d 50C .33 Isc and M2063g 25C .33 Isc could not be stabilized under the circumstances.

One problem of these manufacturer's samples that has been encountered in previous experiments is the loss of backside contact. The phenomenon was also seen here, most prominently in sample M1853d 50C .33 Isc (see figure 4.8). It is assumed that due to the manufacturing process, the backside contact deteriorates after some time of use. This leads to a rapid fall of short circuit current and unstable behavior.

5.1.3 CZTS: JMAK fit parameters and Arrhenius behavior

To model the samples' behavior, the mentioned JMAK fits were applied, with Avrami exponent n and characteristic time τ.
n can give indications about the dimensionality of the underlying processes (it is related to the number of defect centers). This is a highly material-specific property, thus it is

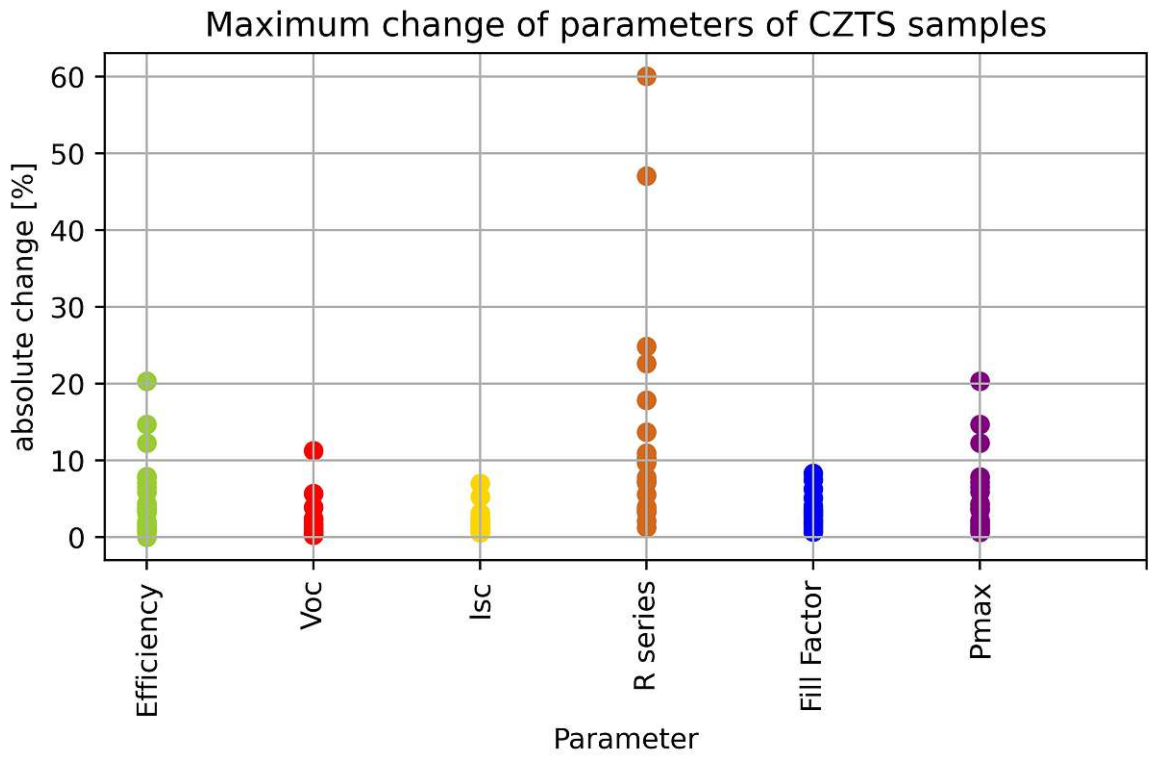

Figure 5.1: Shown is the absolute change in percent of the most important electrical parameters of CZTS minimodules.

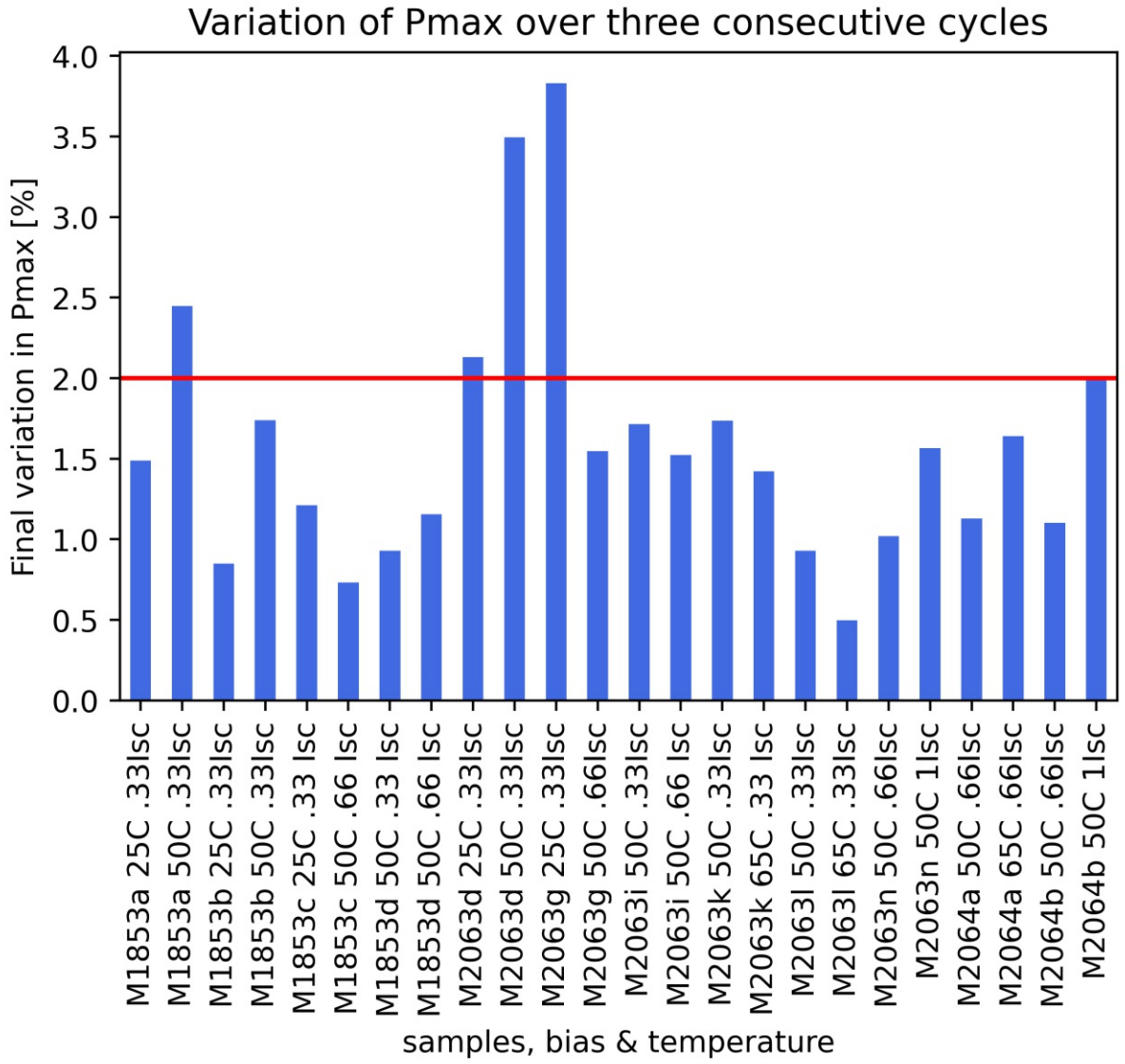

Figure 5.2: Bar chart of variation of maximum power output for dark bias experiments in all CZTS mini modules. The red line indicates the 2% marker dictated by the IEC standard describing stabilization (if three consecutive cycles are below the threshold). We see that only four samples did not pass the criterium, namely M1853a Round 2 (50C $.33I_{sc}$), M2063d in Rounds 1 and 2 (25C $.33I_{sc}$ and 50C $.33I_{sc}$) as well as M2063g Round 1 (25C $.33I_{sc}$).

to be expected that one sample has roughly the same n for all temperatures/biases. If a fit with this assumption is not possible, it is to be assumed that the number of defects changed significantly.
Due to the assumptions of the underlying processes, n was expected to change rather with bias current than with temperature.
τ on the other hand was expected to change mainly with temperature and stay fairly constant with changing bias current.

The results of the final JMAK fitting parameters presented in table 4.4 and the averaged $\overline{\tau}$ and $\overline{n}$ fit well into these assumptions.
From the acquired values of n it can be surmised that the stimulated process is not a low-dimensional (surface) process, but rather a voluminous process. Surface processes are often characterized by values of $n < 2$.
Values for τ exhibit dependence on temperature but not bias current.

The **Arrhenius** fits for both n and τ in figure 4.12 show that the assumption of Arrhenius behavior is a good one for both parameters. This indicates that the changes modeled here are in fact thermally activated.

5.1.4 CZTS: Comparison with light soaking of CZTS mini modules

Figure 5.3 shows the behavior of the power output of a CZTS mini module in traditional light soaking.
While this curve is not totally similar to the dark biasing results, neither is it completely different. The general trend of a decreasing power output holds true, as does the pacing of the change, first quick, then slowly stabilizing.

5.1.5 CZTS: Summary and settings for full scale experiments

After all these preliminary measurements, it was determined to use 50°C, 65°C and 75°C as temperatures for the full scale biasing experiments. 25°C was disregarded since there would be no comparability with traditionl experiments conducted in light soaking (operating temperatures start at around 40°C).
For bias, it was agreed to not vary in the course of the following measurements. While the influence of current bias on the stabilization behavior is of interest, the measurements conducted here were limited in number and thus it was necessary to focus on one parameter.
The bias for the thin film CIGS modules used in full scale modules was set at 1/3 average initial I_{sc}, since this worked very well for the CZTS samples. For the c-Si modules 2/3 I_{sc} was used, to induce a larger reaction in these generally more stable modules.

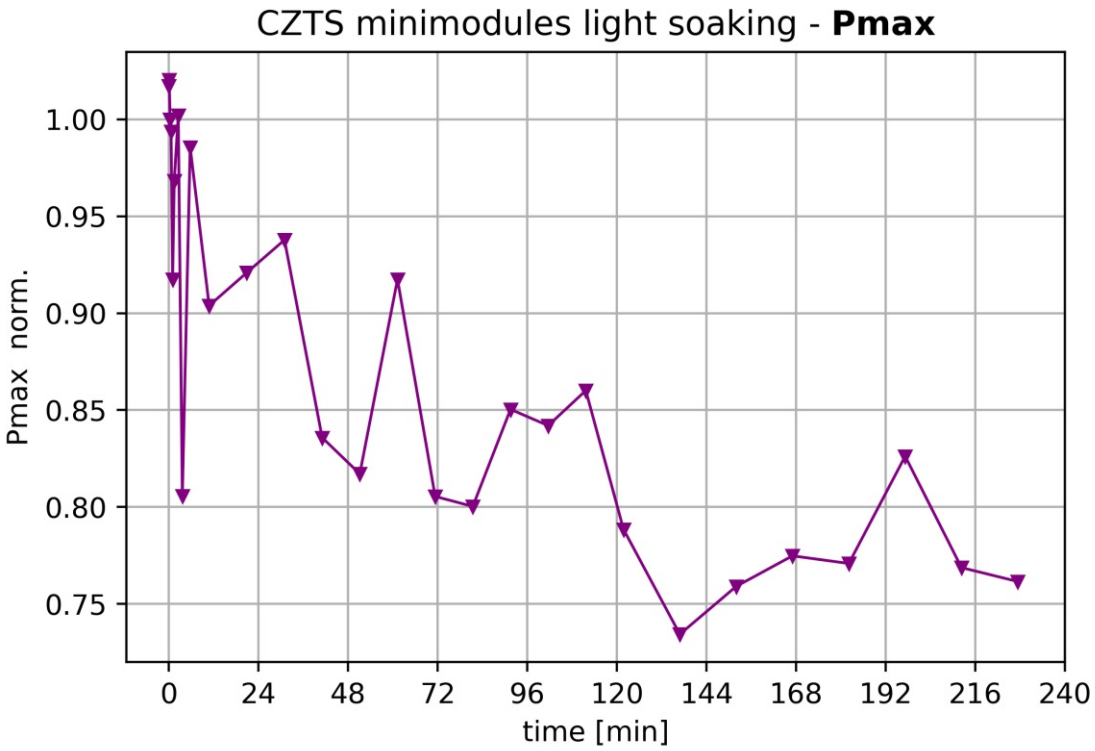

Figure 5.3: Pictured is the behavior of P_{max} of a CZTS mini module in traditional light soaking. During the first few minutes, measurements are more frequent, until after 30minutes they come in regular 30min intervals.

5.2 CIGS and mono-c-Si full scale modules

Contrary to the CZTS modules which were in an ordered state to begin with and then degraded before stabilization, the investigated CIGS modules appeared more unordered. This difference stems from the very different manufacturing process of both types of modules.
In the CIGS modules an initial increase in power and improvement of overall electrical parameters was observed, consistent with healing of point defects introduced during manufacturing.

5.2.1 Full scale: Influence of temperature during bias on electrical parameters

CIGS

Considering figure 4.13 the following can be said for the examined CIGS modules:

- for P_{max}, fill factor, I_{mpp} and V_{mpp} there is a pronounced difference between modules

CIGS 1 and CIGS 2, where CIGS 1 has larger changes in all these parameters

- changes in I_{sc} and V_{oc} are on a very small scale, below the resolution of measuring instruments featured here
- $\mathbf{P}_{max}$: There is a noteworthy tendency for higher temperatures to also bring larger deviation (not strictly, but on average). This is the most pronounced in the first step of biasing and less pronounced in the second and third steps.
- **Fill factor**, $\mathbf{I}_{sc}$: Losses in fill factor do not completely correlate with losses in P_{max}. This can be explained either with a loss of fill factor by loss of I_{mpp} (although this change is again, within the measurement accuracy) or by an improvement via better voltage. The letter can be explained by a higher number of surface contacts.

c-Si

Considering figure 4.14 these statements can be made:

- all changes happened on extremely small scales ($< 1\%$)
- there is a spread in increase and decrease for all parameters
- bias appears to cause both degrading, rearranging mechanisms (c-Si 1 50°C, light green curve) as well as ordering mechanisms (c-Si 75°C, dark blue curve)
- V_{oc} and V_{mpp} appear to be sorted by temperature (the higher the temperature, the larger these parameters). This indicates that 50°C are not enough to trigger annealing, so no weak bonds are healed here yet.

Figure 5.4 contains the normalized maximum parameter changes for all CIGS and c-Si modules. All parameter changes are on much larger scales for CIGS modules, while the c-Si modules showed almost no changes in any parameters.
The largest changes in CIGS parameters are in P_{max} , DUT and cell efficiency and fill factor (all parameters' changes are $\approx 7\%$). The smallest variation was observed in V_{oc} and I_{sc} ($\approx 1\%$).

5.2.2 Full scale: Stabilization

From a glance at figure 5.5, it can be seen that all full scale modules achieved stabilization in all experiments. The values are also all well below the 2%-threshold (with only one CIGS sample above a 1% change, CIGS 2 in 75°C bias).
It also shows that power changes for c-Si modules were much smaller than for the thin film CIGS modules.

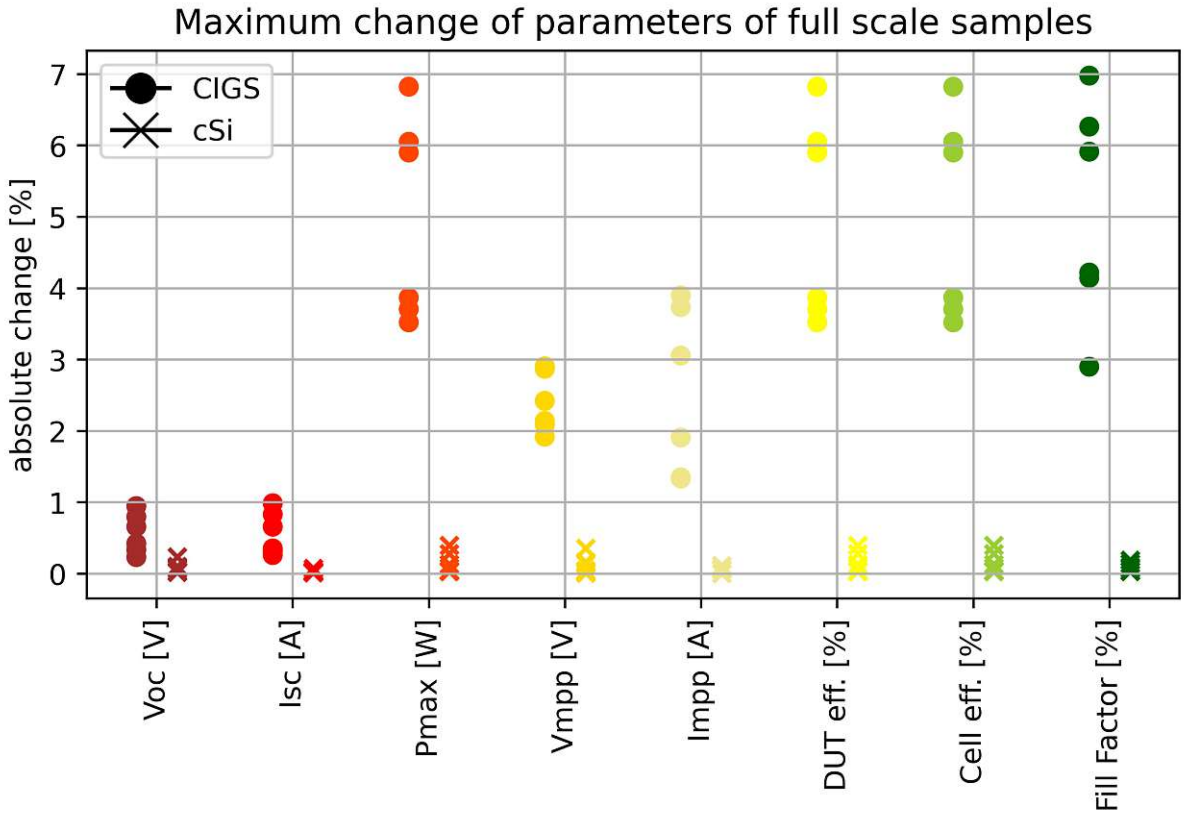

Figure 5.4: Shown is the absolute change in percent of the most important electrical parameters of CIGS (dots) and c-Si (crosses) modules.

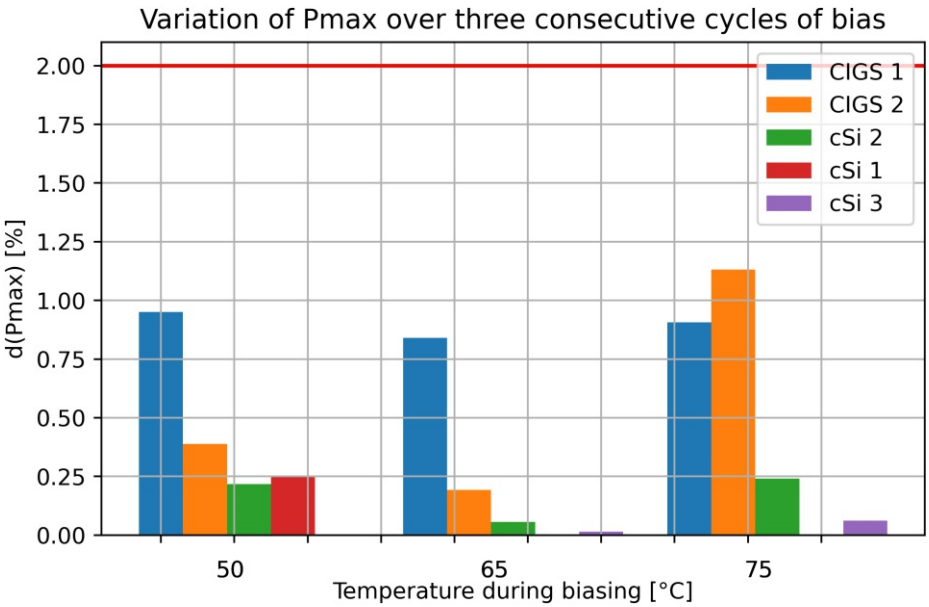

Figure 5.5: Overview of changes in parameters for all full scale modules between dark biasing procedures, as well as the 2%-marker indicating stabilization.

Keeping in mind that the goal was to show stabilization similar to stabilization in outdoor exposure or light soaking, this was not achieved with this series of experiments. A guess is that the applied current bias was too small to induce degrading effects like the ones usually seen in light exposure.

5.2.3 CIGS: JMAK fit parameters and Arrhenius behavior

As explained in section 4.2.3, JMAK fits were attempted for CIGS modules only, since the changes observed in c-Si modules were far too small.
The fits for CIGS 1 and CIGS 2 were all made with the same n ($n = 3.28$ for CIGS 1 and $n = 2.87$ for CIGS 2 at all temperatures). The fact that fits were possible with one n per module is a good indicator that n is only dependent on material and does not change with temperature. As mentioned above, a change in n within the same sample would be best explained by a large change in the number of defects. Since this was not observed here, it is to be assumed that the defect density remained stable.

The values of average characteristic time $\overline{\tau}$ were then used for the Arrhenius plot in figure 4.16, exhibiting good linear behavior. This can be interpreted as a solely thermally activated process.

Full scale: EL images

As noted above, electroluminescence images were taken to monitor any large damages to the modules during dark bias procedures. By comparing the pre- and post-dark-bias-pictures in figure 4.17, no such damages were found.

5.2.4 c-Si: Comparison with mono-c-Si outdoor exposure

The comparability of outdoor exposure and dark bias stabilization is rather surprising, due to the differences in underlying processes (photo effect, Auger-electrons,...).

The circumstances for outdoor exposures were different from dark biasing in a number of ways, most importantly the incoming sunlight. Both exposure to UV light and current can break weak van-der-Waals bonds, but there may be a difference in the way and/or severity at which the breaking occurs and the underlying processes might be different.

The comparison of outdoor exposure and dark bias measurements in this work was complicated by the very small changes observed in dark biasing. It can be surmised that with the right parameters of temperature and current bias for dark bias experiments, a behavior like the one typically seen in outdoor exposure (see figure 4.18(a)) can occur. However it was not observed with the parameters used here.

5.2.5 Full scale: IV characteristic

The effects of current bias and temperature on modules - as noted in section 4.2.7 - were seen only in CIGS modules. Since the change of all parameters in c-Si was far too small, the IV-characteristic did not change at all (see figure 4.19(b). The characteristic of CIGS modules was however slightly improved (see figure 4.19(a) by bias and/or temperature. Again, it is to be surmised that different parameters of bias current and temperature might bring improvements.

5.3 Conclusion

The application of dark bias as an alternative to light soaking for stabilization of power output in photovoltaic modules was investigated first in literature and followed by experiments.
In literature before the 2017 Pearl-TF PV project, dark bias stabilization was conducted with high bias currents. These yielded quite unfavorable results. In the Pearl-TF PV project a smaller bias was applied and this lead to surprisingly good results. These smaller currents were used for the experiments here.

In accordance to the findings of the Pearl-TF PV project, it was possible to stabilize CZTS minimodules without light exposure in a laboratory setting. On the full scale CIGS and c-Si modules investigated, using the described parameters for current bias and temperature, the results are not so clear.

The observations can be summarized as such:

- order-disorder transitions driven by temperature and injection of charge carriers were observed
- **CZTS:** ordered initially, then disordered/degraded by application of bias and/or temperature (initial decline of P_{max} followed by stabilization for most samples)
- **CZTS:** the higher the temperature during bias, the larger the changes in P_{max}
- **CZTS:** the larger the biasing current I_{sc}, the smaller the changes in P_{max}
- **CZTS:** JMAK fits go well with the assumptions for n and τ
- **CZTS:** JMAK fits indicate that the stimulated process is a voluminous process rather than a surface process
- **CZTS:** fitted values for characteristic time τ depend on temperature but not bias current
- **CZTS:** both n and τ exhibit Arrhenius behavior (underlying processes are likely thermally activated)
- **CZTS:** results for dark biasing are comparable to light soaking of similar modules
- **Full scale:** all full scale modules were stabilized
- **CIGS:** higher temperatures caused larger changes in P_{max}
- **CIGS:** JMAK fits indicate stable defect density (same n could be used for all fits of one sample)
- **CIGS:** exhibited good Arrhenius behavior

- **c-Si:** dark bias caused degrading and annealing processes almost equally, but all changes were on a very small scale
- **c-Si:** higher temperatures caused larger changes in V_{OC} and V_{mpp}; only temperatures T>50°C triggered annealing
- **c-Si:** dark bias experiments with the given parameters are not comparable to outdoor exposure of c-Si modules

The findings from the CZTS minimodules in particular confirm that in principle, it is possible to use current bias without exposure to light as an alternative to light soaking procedures in order to stabilize thin film PV modules before testing.

The JMAK fits and Arrhenius plots performed show thermally activated behavior (at least the behavior is similar and with the applied methods cannot be distinguished from thermally activated behavior).

On the full scale modules, the chosen parameters (temperature and current bias) were not suitable to induce the order-disorder transformation desired.

5.4 Outlook

As found in the Pearl-TF PV report before, the measurements presented here show that dark bias power stabilization for thin film photovoltaic modules is in fact an alternative to traditional light soaking approaches. Dark bias stabilizations are less time consuming and can be done without a special, expensive setup, making them attractive alternatives for industry and research.
Although the findings of the presented experiments are promising, the exact procedures and parameters will have to be determined for each individual thin film photovoltaic technology in the future.

Bibliography

[1] V. Quaschning, "Regenerative Energiesysteme," *München: Hanser-Verlag*, 1998.

[2] M. T. García-Álvarez, L. Cabeza-García, and I. Soares, "Assessment of energy policies to promote photovoltaic generation in the European Union," *Energy*, vol. 151, pp. 864–874, 2018.

[3] A. Jäger-Waldau, "PV status report 2019," *Institute for Energy and Transport, Renewable Energy Unit*, 2019.

[4] K. Hansen, C. Breyer, and H. Lund, "Status and perspectives on 100% renewable energy systems," *Energy*, vol. 175, pp. 471–480, 2019.

[5] A. Wagner, *Photovoltaik Engineering*. Springer, 5 ed., 2019.

[6] C. Deline, A. Stokes, T. J. Silverman, S. Rummel, D. Jordan, and S. Kurtz, "Electrical bias as an alternate method for reproducible measurement of copper indium gallium diselenide (CIGS) photovoltaic modules," in *Reliability of Photovoltaic Cells, Modules, Components, and Systems V*, vol. 8472, p. 84720G, International Society for Optics and Photonics, 2012.

[7] S. Philipps and W. Warmuth, "Photovoltaics Report Fraunhofer Institute for Solar Energy Systems," ISE, 2019.

[8] J. A. del Cueto, C. A. Deline, S. R. Rummel, and A. Anderberg, "Progress toward a stabilization and preconditioning protocol for polycrystalline thin-film photovoltaic modules," in *2010 35th IEEE Photovoltaic Specialists Conference*, pp. 002423–002428, IEEE, 2010.

[9] M. G. Deceglie, T. J. Silverman, K. Emery, D. Dirnberger, A. Schmid, S. Barkaszi, N. Riedel, L. Pratt, S. Doshi, G. Tamizhmani, *et al.*, "Validated method for repeatable power measurement of cigs modules exhibiting light-induced metastabilities," *IEEE Journal of Photovoltaics*, vol. 5, no. 2, pp. 607–612, 2014.

[10] IEC 61215/1-1-x, "Terrestrial photovoltic (PV) modules - Design qualification and type approval," standard, International Electrotechnical Commission, 2016.

[11] R. Sasala and J. Sites, "Time dependent voltage in $CuInSe_2$ and CdTe solar cells," in *Conference Record of the Twenty Third IEEE Photovoltaic Specialists Conference-1993 (Cat. No. 93CH3283-9)*, pp. 543–548, IEEE, 1993.

[12] T. J. Silverman, M. G. Deceglie, B. Marion, and S. R. Kurtz, "Performance stabilization of CdTe PV modules using bias and light," in *2014 IEEE 40th Photovoltaic Specialist Conference (PVSC)*, pp. 3676–3681, 2014.

[13] H. Häberlin, "Photovoltaik," *AZ-Verlag/VDE-Verlag, Aarau*, 2007.

[14] M. Gostein and L. Dunn, "Light soaking effects on photovoltaic modules: Overview and literature review," in *2011 37th IEEE Photovoltaic Specialists Conference*, pp. 003126–003131, IEEE, 2011.

[15] "Pearl TF-PV Project Website." `https://pearltf.eu/`. last visited: 26.01.2021.

[16] M. A. Green, *Solar cells: Operating principles, technology, and system applications*. 1982.

[17] J. Goldemberg *et al.*, *World Energy Assessment: Energy and the challenge of sustainability*. United Nations Development Programme New York, 2000.

[18] G. Reich and M. Reppich, *Regenerative Energietechnik*. Springer, 2 ed., 2018.

[19] H.-G. Wagemann and H. Eschrich, *Photovoltaik*. Springer, 2 ed., 2010.

[20] M. Planck, "Ueber irreversible Strahlungsvorgänge," *Annalen der Physik*, vol. 306, no. 1, pp. 69–122, 1900.

[21] A. Einstein, "Über einem die Erzeugung und Verwandlung des Lichtes betreffenden heuristischen Gesichtspunkt," *Annalen der physik*, vol. 4, 1905.

[22] A. Jäger-Waldau, I. Kougias, N. Taylor, and C. Thiel, "How photovoltaics can contribute to GHG emission reductions of 55% in the EU by 2030," *Renewable and Sustainable Energy Reviews*, vol. 126, p. 109836, 2020.

[23] G. Martinopoulos, "Are rooftop photovoltaic systems a sustainable solution for Europe? A life cycle impact assessment and cost analysis," *Applied Energy*, vol. 257, p. 114035, 2020.

[24] N. M. Haegel, R. Margolis, T. Buonassisi, D. Feldman, A. Froitzheim, R. Garabedian, M. Green, S. Glunz, H.-M. Henning, B. Holder, *et al.*, "Terawatt-scale photovoltaics: Trajectories and challenges," *Science*, vol. 356, no. 6334, pp. 141–143, 2017.

[25] Wikimedia Commons, "Price history of silicon PV cells since 1977." `https://commons.wikimedia.org/wiki/File:Price_history_of_silicon_PV_cells_since_1977.svg`, 2015. last accessed: 2020-11-06.

[26] M. Bazilian, I. Onyeji, M. Liebreich, I. MacGill, J. Chase, J. Shah, D. Gielen, D. Arent, D. Landfear, and S. Zhengrong, "Re-considering the economics of photovoltaic power," *Renewable Energy*, vol. 53, pp. 329–338, 2013.

[27] S. Lower, "LibreTexts.org, book 'Chem 1', chapter 9.10 Bonding in Metals." `https://chem.libretexts.org/Bookshelves/General_Chemistry/Book\%3A_Chem1_(Lower)/09\%3A_Chemical_Bonding_and_Molecular_Structure/9.10\%3A_Bonding_in_Metals`. last accessed: 2021-06-09.

[28] W. Demtröder, *Experimentalphysik 3: Atome, Moleküle und Festkörper*. Springer-Verlag, 2010.

[29] D. Menz, "Light soaking of thin-film solar cells under colored light," Master's thesis, Vienna University of Technology, 2015.

[30] V. Wesselak and S. Voswinckel, *Photovoltaik–Wie Sonne zu Strom wird*. Springer-Verlag, 2016.

[31] D.-K. Seo and R. Hoffmann, "Direct and indirect band gap types in one-dimensional conjugated or stacked organic materials," *Theoretical Chemistry Accounts*, vol. 102, no. 1, pp. 23–32, 1999.

[32] S. Jones, *Metastable effects in chalcogenide thin film photovoltaic devices*. PhD thesis, 5 2020.

[33] A. McEvoy, L. Castaner, and T. Markvart, *Solar cells: materials, manufacture and operation*. Academic Press, 2012.

[34] R. Ebner, B. Kubicek, G. Újvári, S. Novalin, M. Rennhofer, and M. Halwachs, "Optical characterization of different thin film module technologies," *International Journal of Photoenergy*, vol. 2015, 2015.

[35] NREL, "Best Research-Cell Efficiency Chart." `https://www.nrel.gov/pv/assets/pdfs/best-research-cell-efficiencies.20200104.pdf`, 2020. last accessed: 23.02.2021.

[36] A. Redinger, D. M. Berg, P. J. Dale, R. Djemour, L. Gütay, T. Eisenbarth, N. Valle, and S. Siebentritt, "Route Toward High-Efficiency Single-Phase $Cu_2ZnSn(S, Se)_4$ Thin-Film Solar Cells: Model Experiments and Literature Review," *IEEE Journal of Photovoltaics*, vol. 1, no. 2, pp. 200–206, 2011.

[37] A. Mittal, G. Ujvari, T. Dimopoulos, M. Rennhofer, S. Lopez, L. Plessing, and V. Schlosser, "Investigation of light induced metastabilities through colored filters on CZTSSe monograin PV devices." Poster at PVSEC 2016 conference, Munich; 20.06.2016 - 24.06.2016.

[38] T. J. Silverman, U. Jahn, G. Friesen, M. Pravettoni, M. Apolloni, A. Louwen, W. van Sark, M. Schweiger, G. Belluardo, J. Wagner, *et al.*, "Characterisation of performance of thin-film photovoltaic technologies," 2014.

[39] S. Novalin, M. Rennhofer, and J. Summhammer, "Electrical metastabilities in chalcogenide photovoltaic devices," *Thin solid films*, vol. 535, pp. 261–264, 2013.

[40] M. N. Ruberto and A. Rothwarf, "Time-dependent open-circuit voltage in $CuInSe_2$/CdS solar cells: Theory and experiment," *Journal of Applied Physics*, vol. 61, no. 9, pp. 4662–4669, 1987.

[41] S. Lany and A. Zunger, "Light-and bias-induced metastabilities in Cu (In, Ga) Se 2 based solar cells caused by the (V Se-V Cu) vacancy complex," *Journal of Applied Physics*, vol. 100, no. 11, p. 113725, 2006.

[42] F. Gröstlinger, "CEMS investigation of the phase transition of metastable FeSi thin films," Master's thesis, University of Vienna, 2008.

[43] M. C. Weinberg, D. P. Birnie III, and V. A. Shneidman, "Crystallization kinetics and the JMAK equation," *Journal of non-crystalline solids*, vol. 219, pp. 89–99, 1997.

[44] A. Mittal, M. Rennhofer, A. Dangel, B. Duman, and V. Schlosser, "Power change in amorphous silicon technology by low temperature annealing," *EPJ Photovoltaics*, vol. 6, p. 65304, 2015.

[45] IEC 60904-9, "Thin-film terrestrial photovoltic (PV) modules - Design qualification and type approval: Solar Simulator Performance Requirements," standard, International Electrotechnical Commission, 2007.

[46] IEC 60904-1, "Thin-film terrestrial photovoltic (PV) modules - Design qualification and type approval: Measurement of photovoltaic current-voltage characteristics," standard, International Electrotechnical Commission, 2016.

[47] "Python Software Foundation, Python Language Reference, version 3.8.3." available at `http://www.python.org`.

List of Figures

List of Tables

Abbreviations

I_{SC} short circuit current.

P_{max} maximum power (point).

R_{series} series resistance.

R_{shunt} shunt resistance.

V_{OC} open circuit voltage.

a-Si Amorphous Silicon.

AIT Austrian Institute of Technology.

c-Si crystalline Silicon.

CB conduction band.

CdTe Cadmium Telluride.

CIGS Copper Indium Gallium (Di-)Selenide.

Cu(In,Ga)Se$_2$ Cu(In,Ga)Se$_2$.

CZTS Copper Zinc Tin Sulfide.

EL Electroluminescence.

GaAs Gallium Arsenide.

IEC International Electrotechnical Commission.

JMAK Johnson-Mehl-Avrami-Kolmogorow.

JRC Joint Research Centre of the European Union.

LED light emitting diode.

LS Light Soaking.

MPP maximum power point.

NREL National Renewable Energy Laboratory.

PV photovoltaic.

SCR Space Charge Region.

TF Thin Film.

VB valence band.

A CZTS data

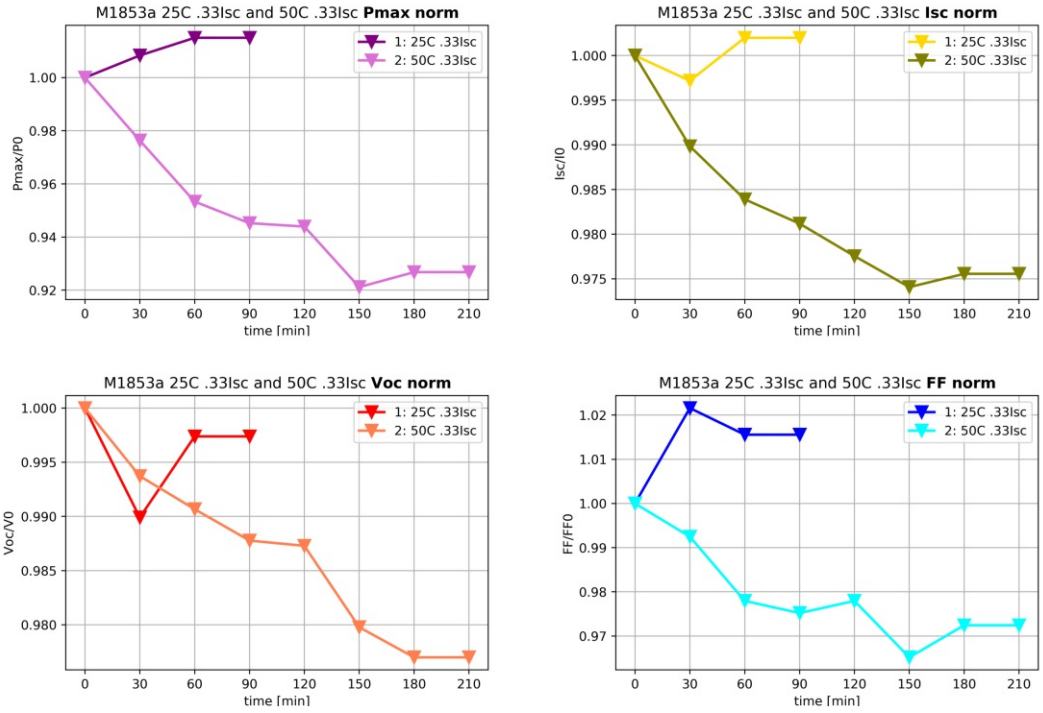

Figure A.1: Sample M1853a, Pmax, Isc, Voc and fill factor.

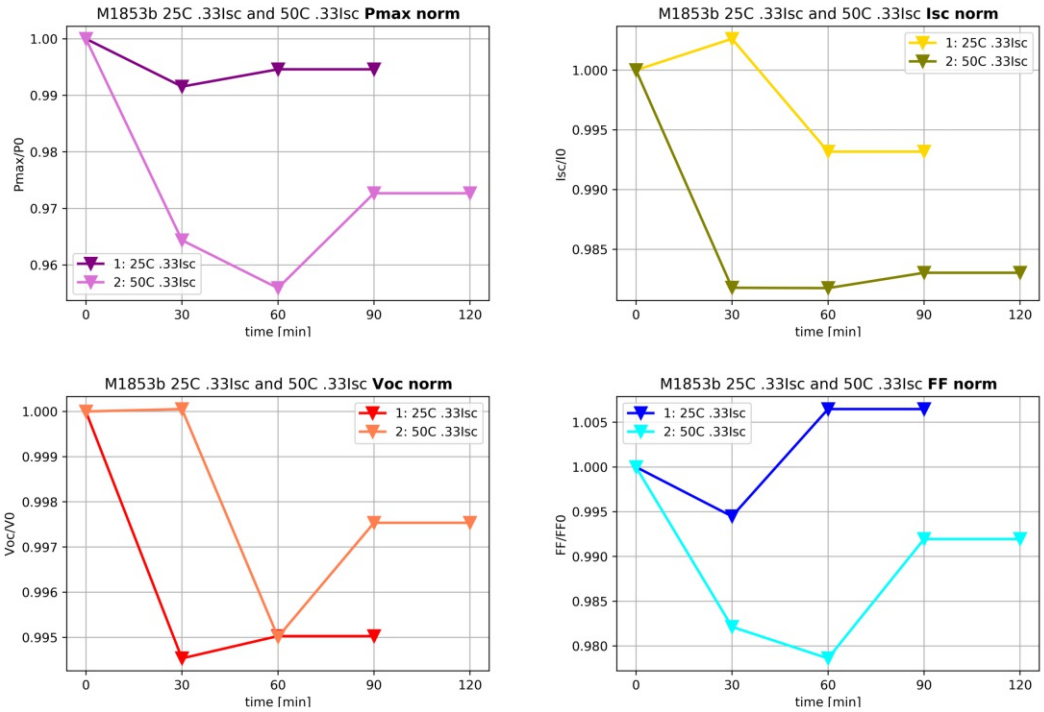

Figure A.2: Sample M1853b, Pmax, Isc, Voc and fill factor.

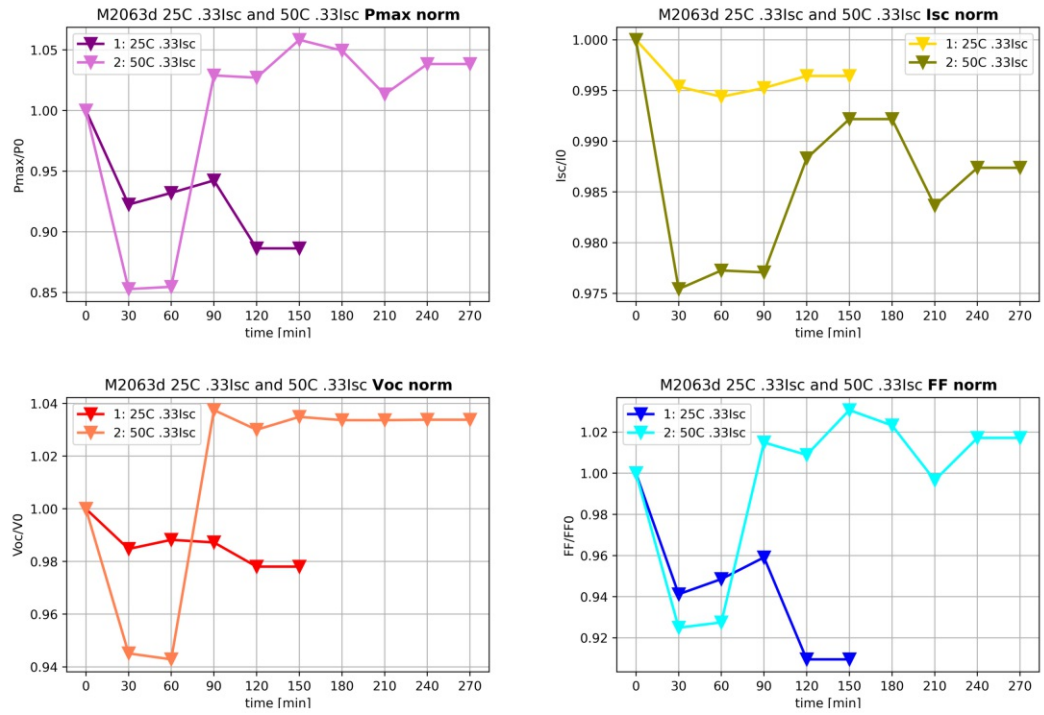

Figure A.3: Sample M2063d, Pmax, Isc, Voc and fill factor.

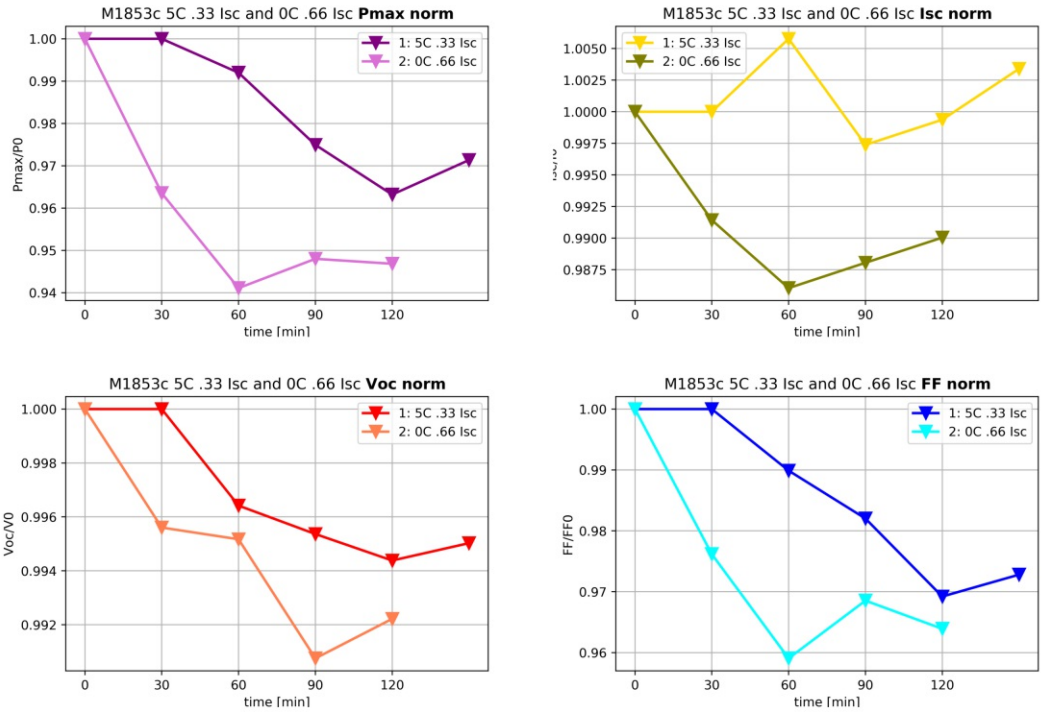

Figure A.4: Sample M1853c, Pmax, Isc, Voc and fill factor.

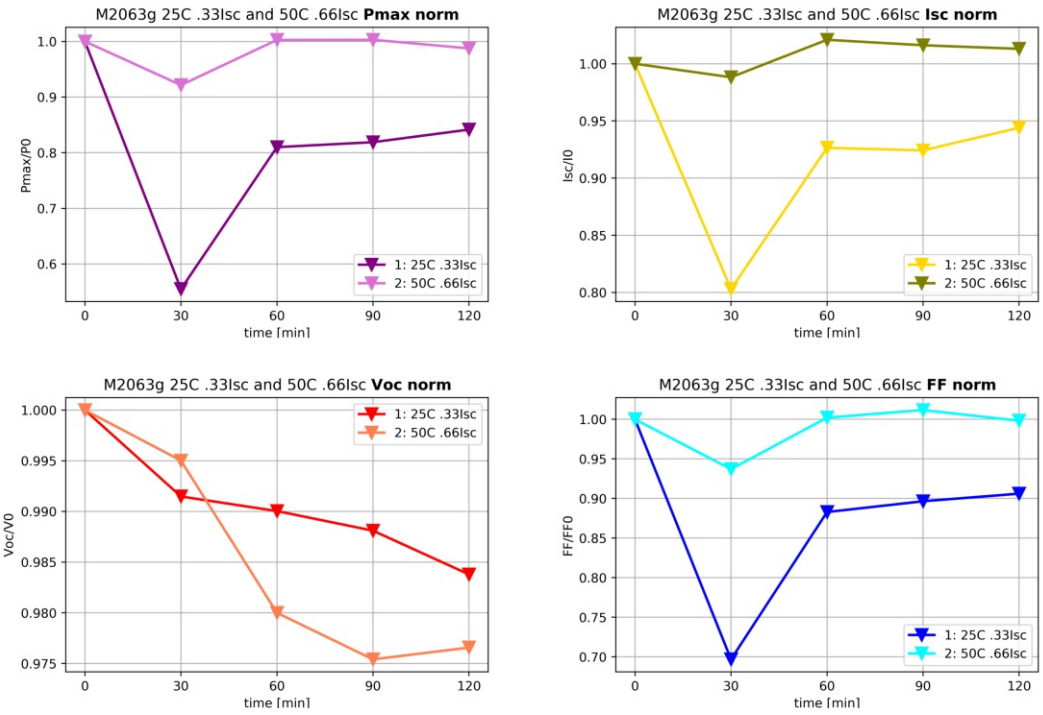

Figure A.5: Sample M2063g, Pmax, Isc, Voc and fill factor.

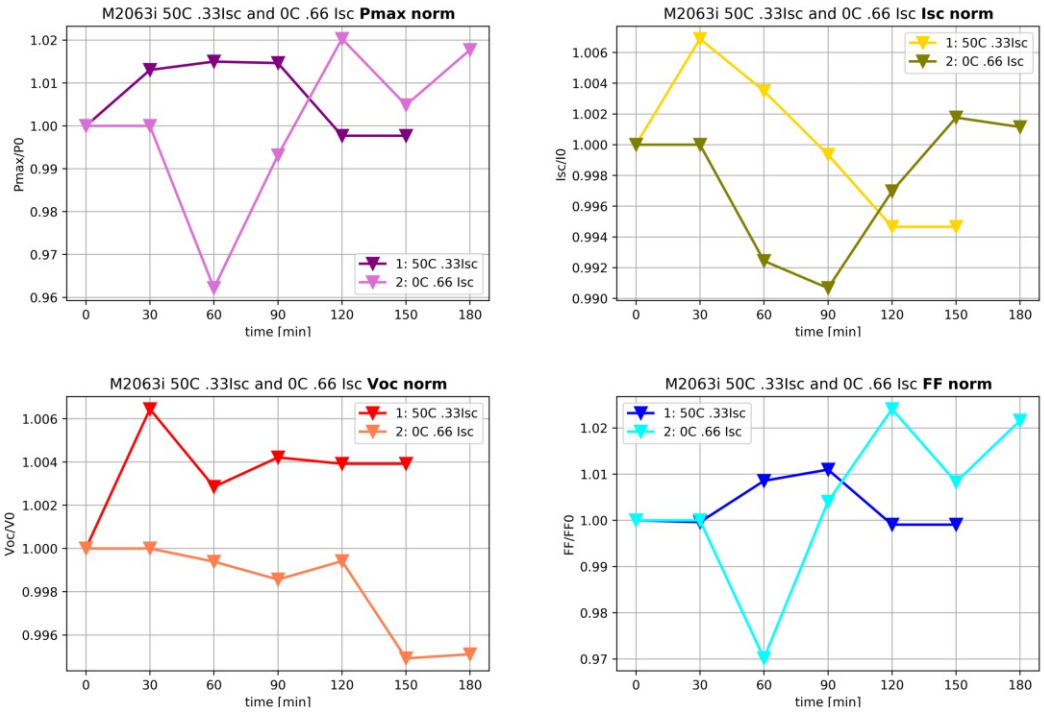

Figure A.6: Sample M2063i, Pmax, Isc, Voc and fill factor.

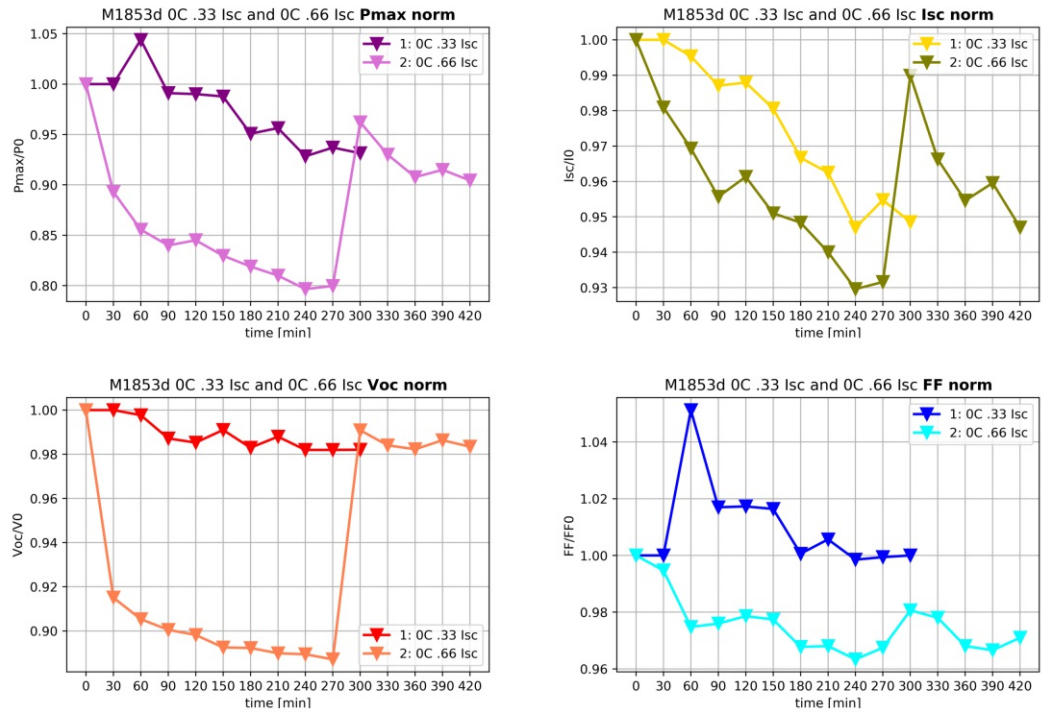

Figure A.7: Sample M1853d, Pmax, Isc, Voc and fill factor.

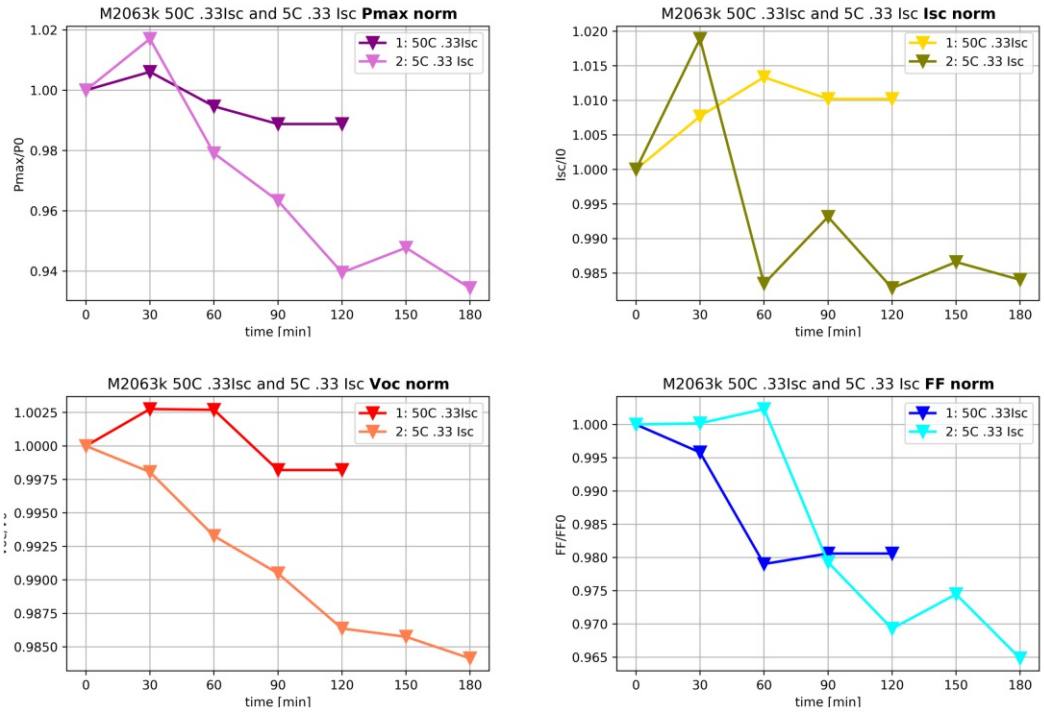

Figure A.8: Sample M2063k, Pmax, Isc, Voc and fill factor.

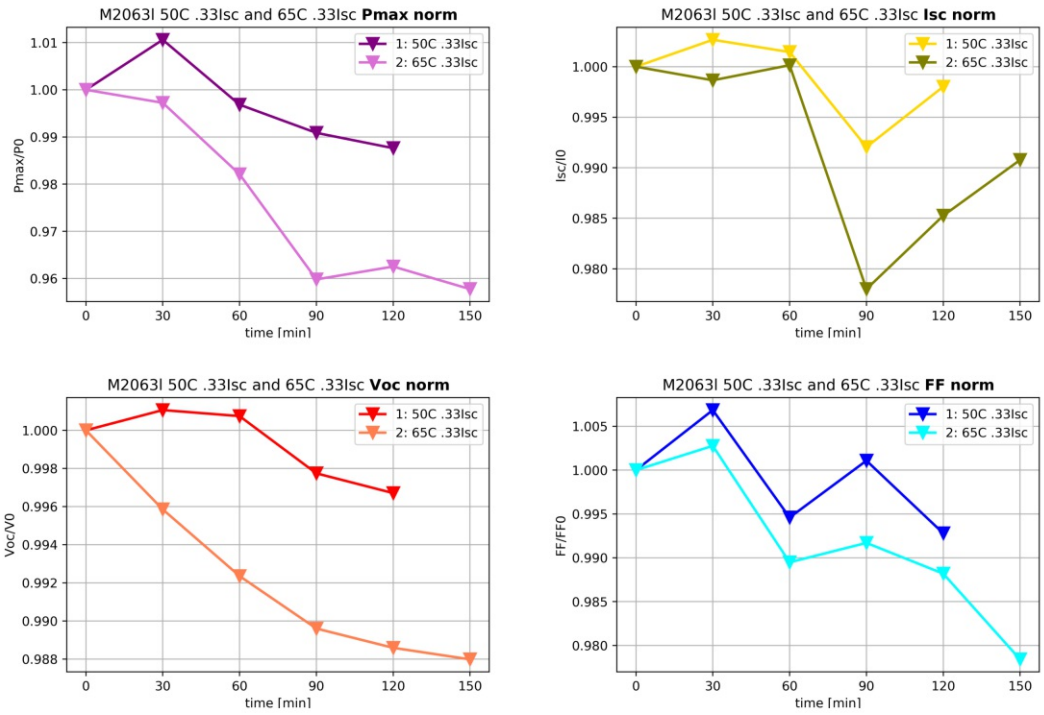

Figure A.9: Sample M2063l, Pmax, Isc, Voc and fill factor.

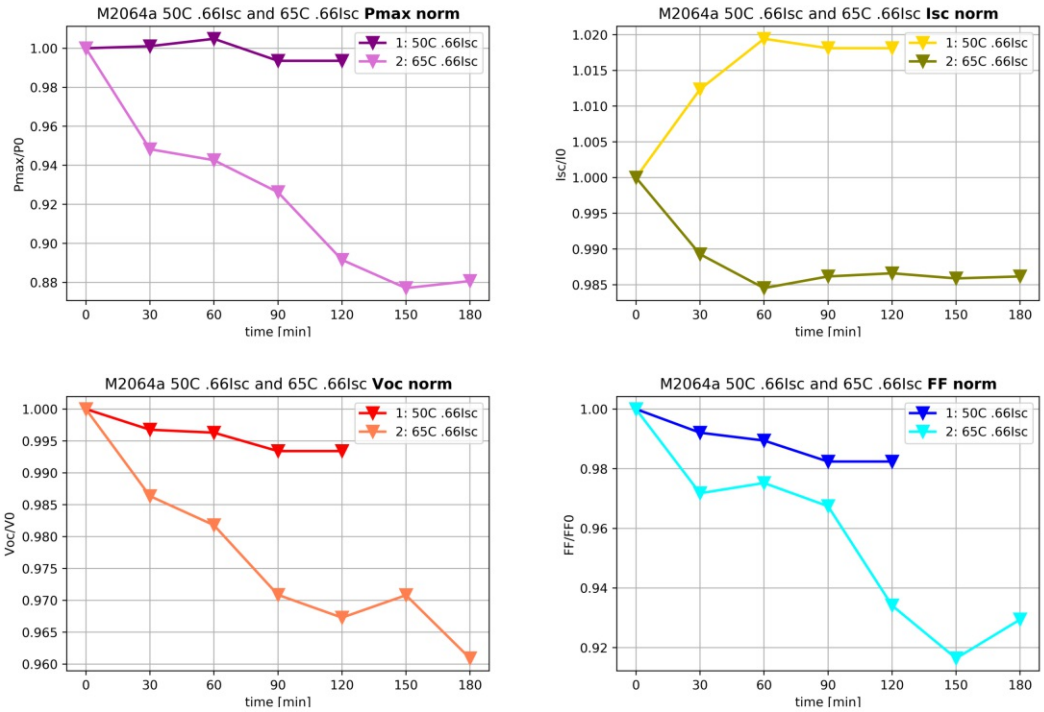

Figure A.10: Sample M2064a, Pmax, Isc, Voc and fill factor.

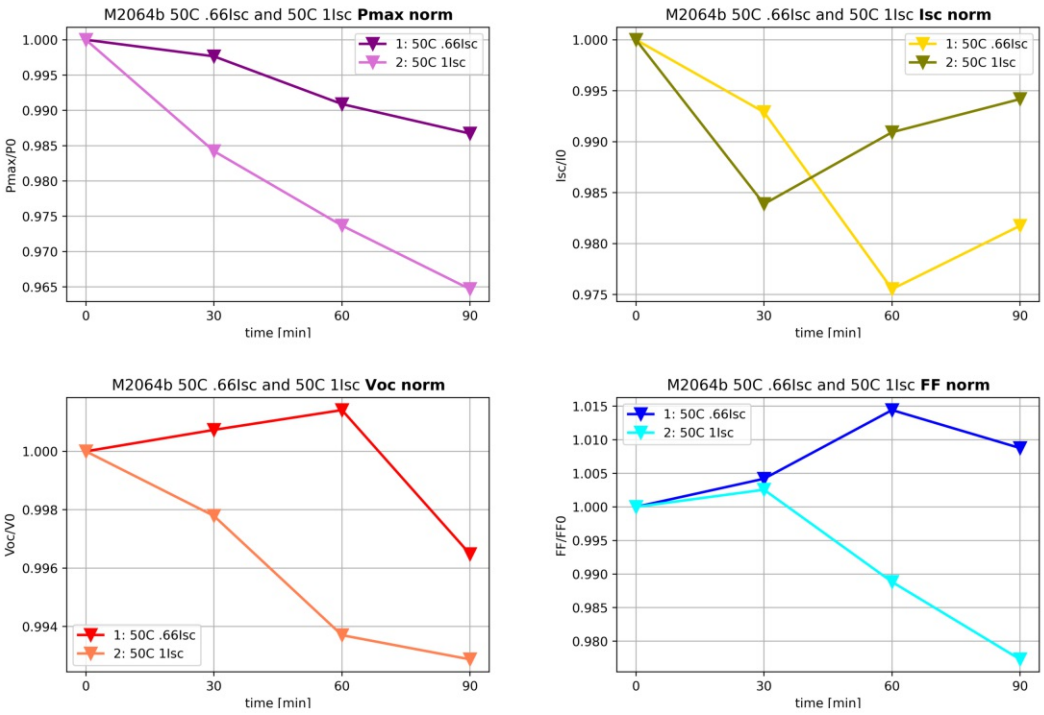

Figure A.11: Sample M2064b, Pmax, Isc, Voc and fill factor.

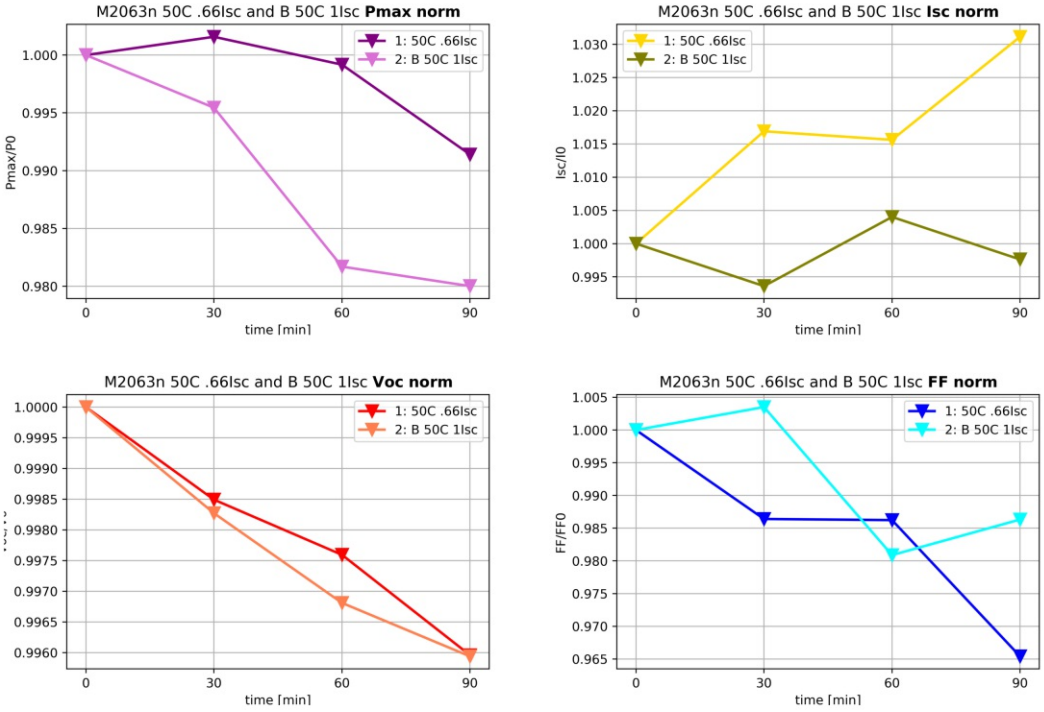

Figure A.12: Sample M2063n, Pmax, Isc, Voc and fill factor.

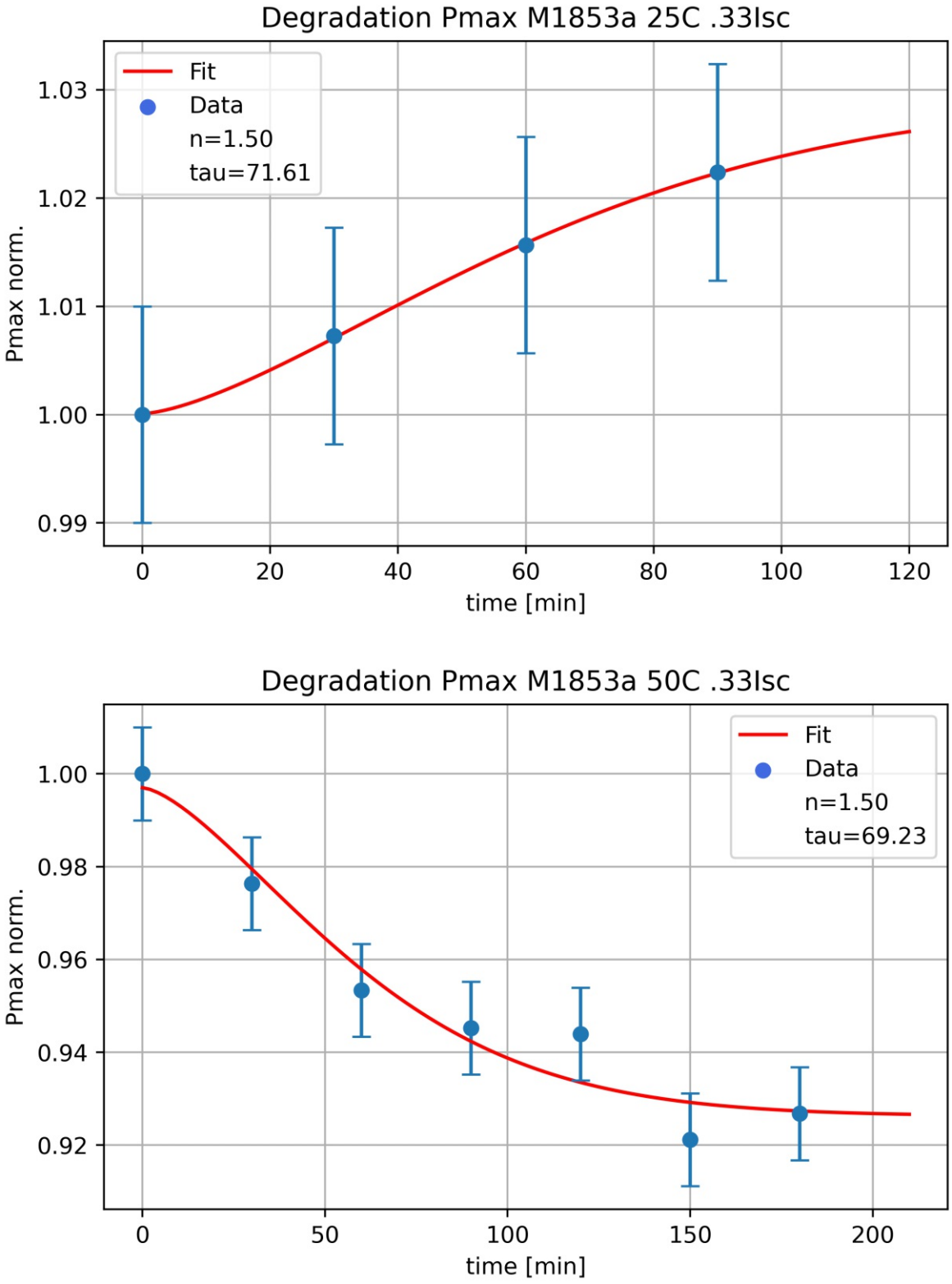

Figure A.13: Sample M1853a JMAK fits

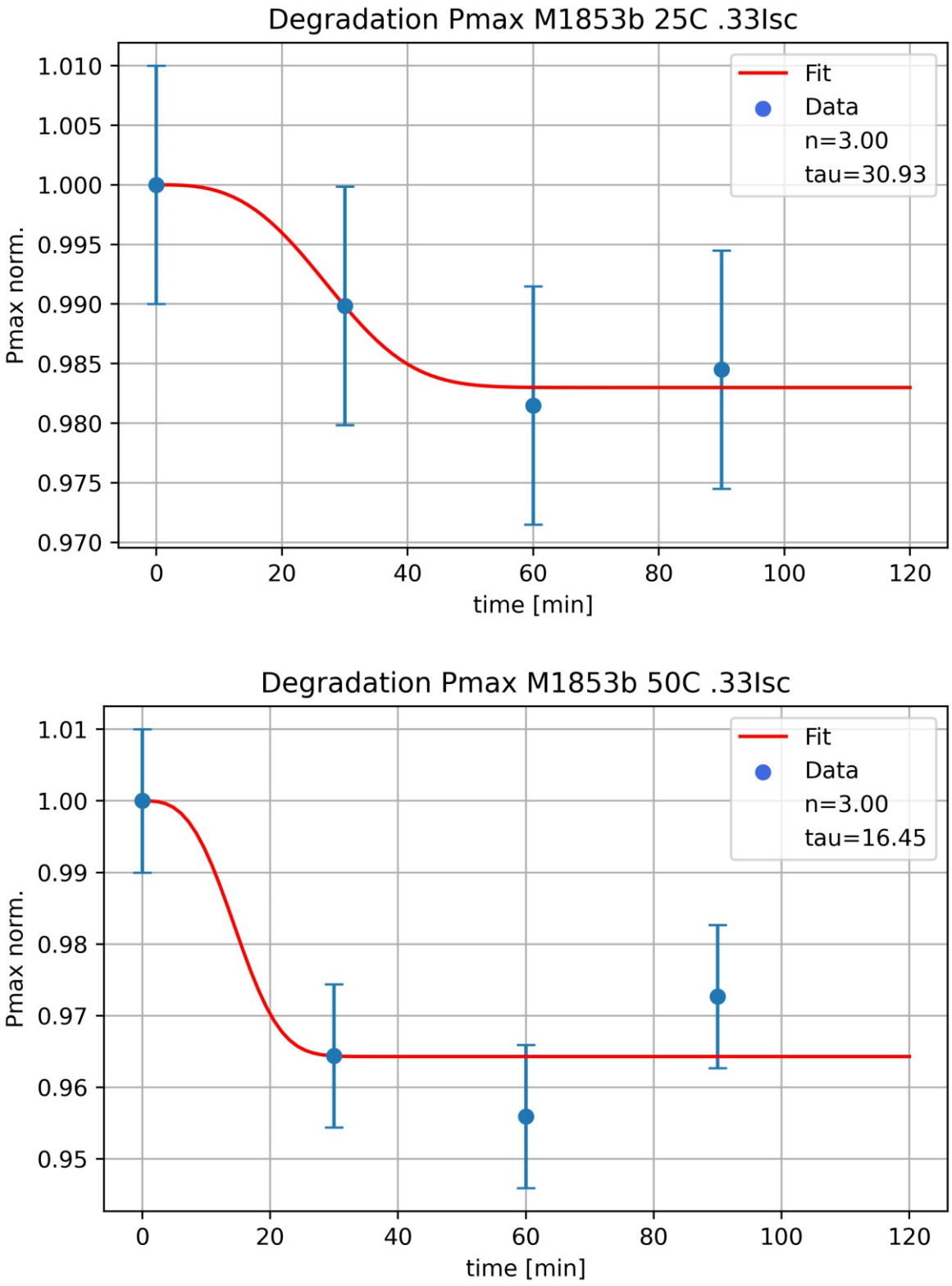

Figure A.14: Sample M1853b JMAK fits

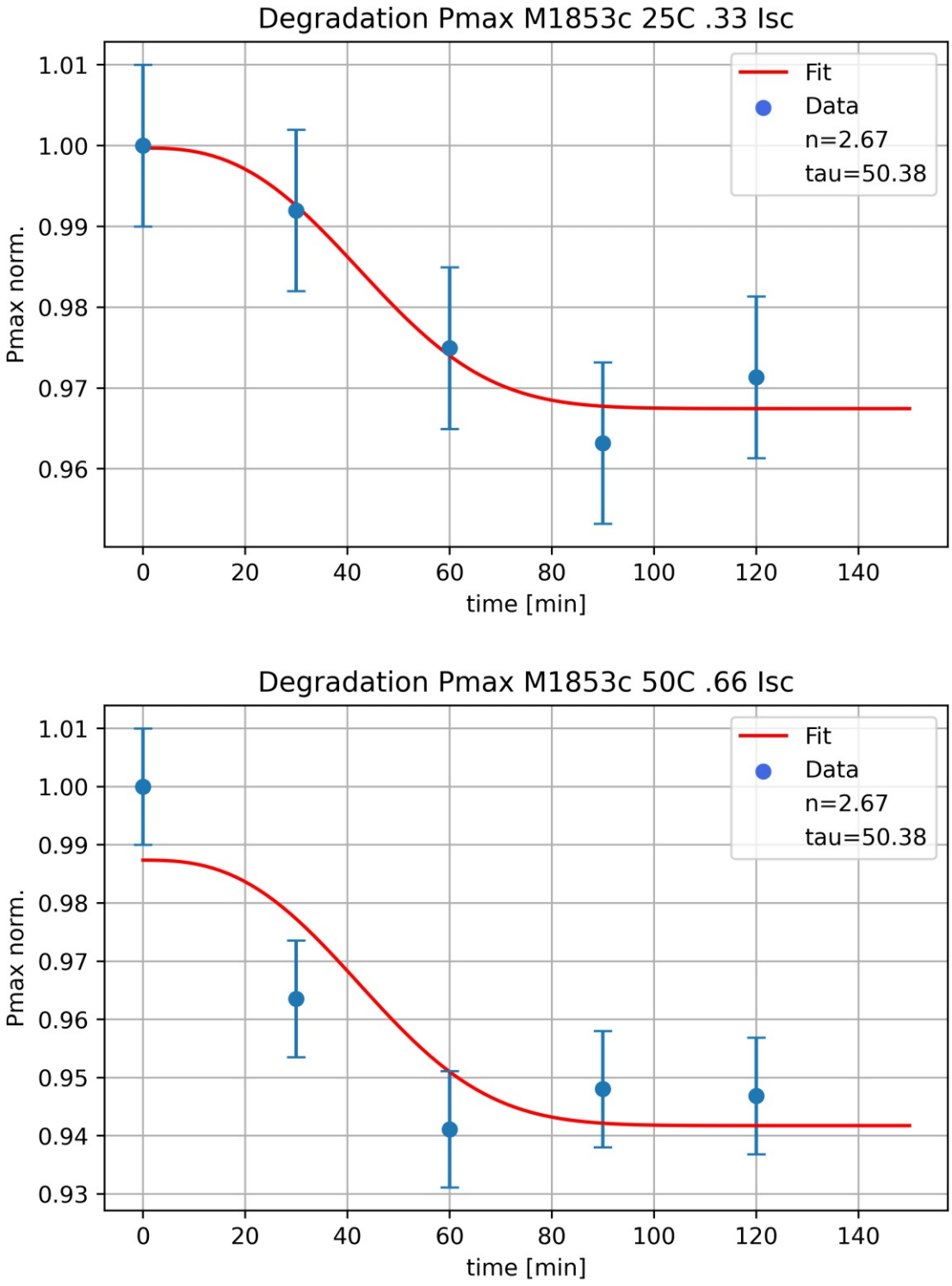

Figure A.15: Sample M1853c JMAK fits

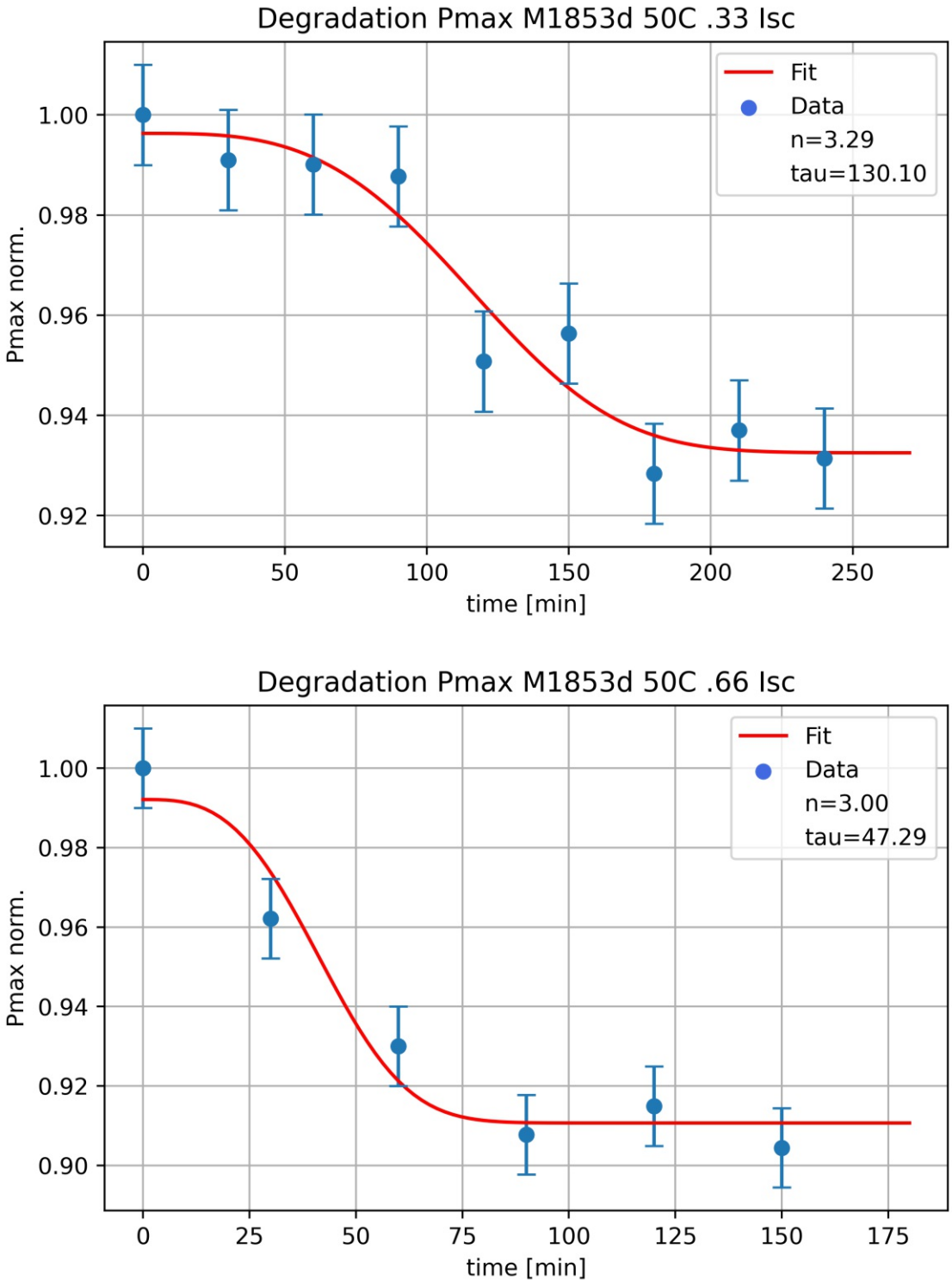

Figure A.16: Sample M1853d JMAK fits

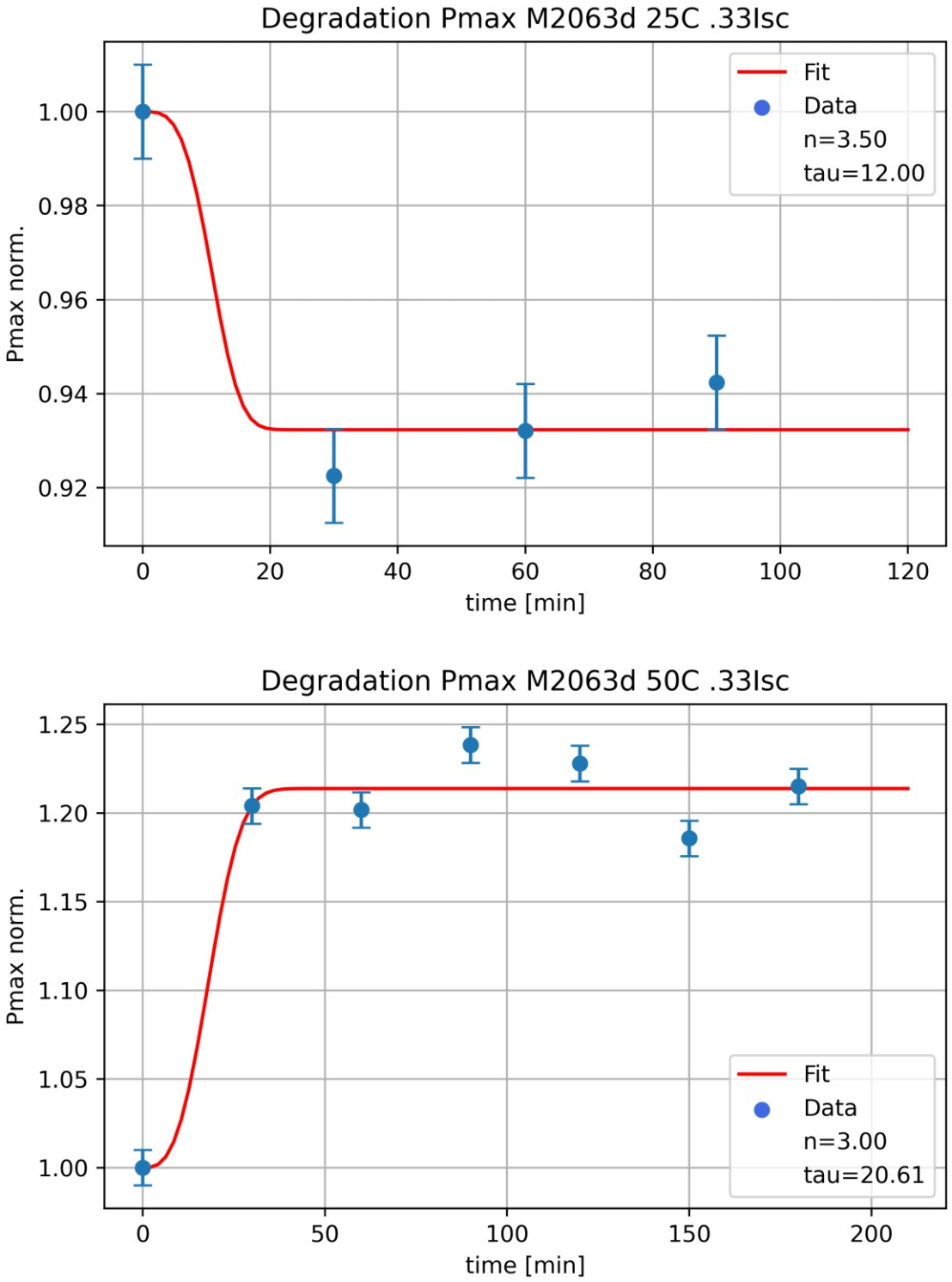

Figure A.17: Sample M2063d JMAK fits

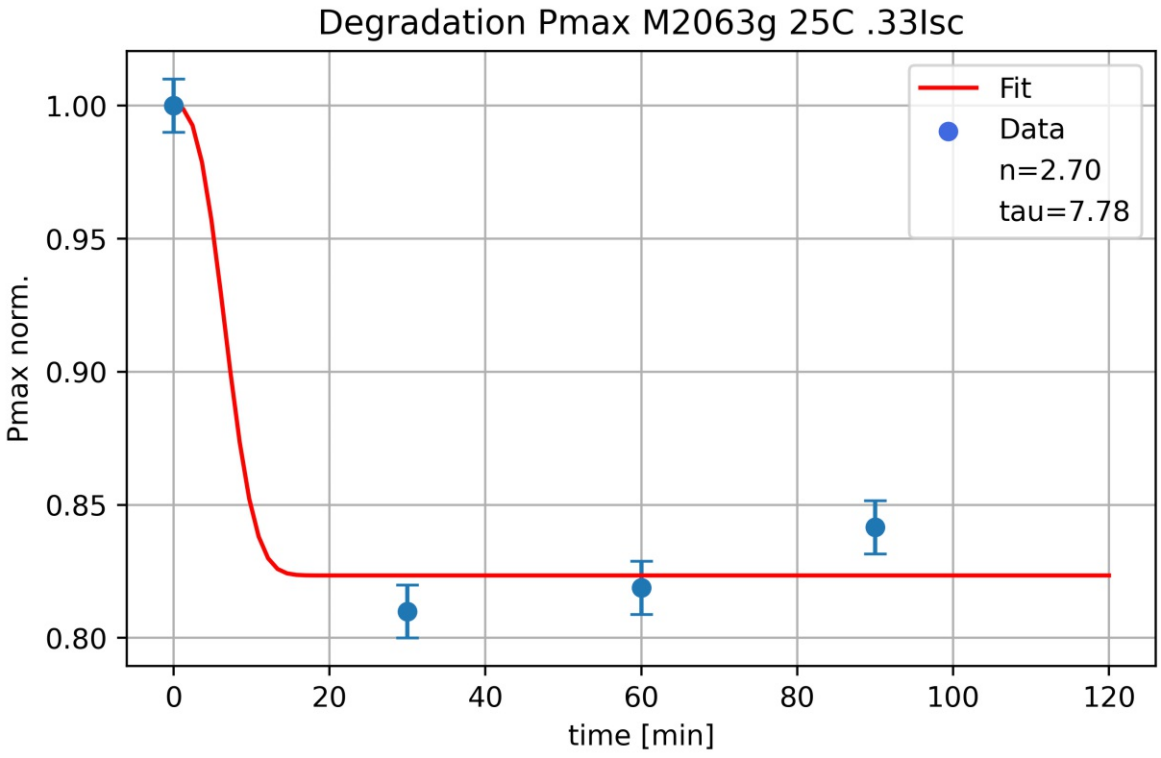

Figure A.18: Sample M2063g JMAK fit

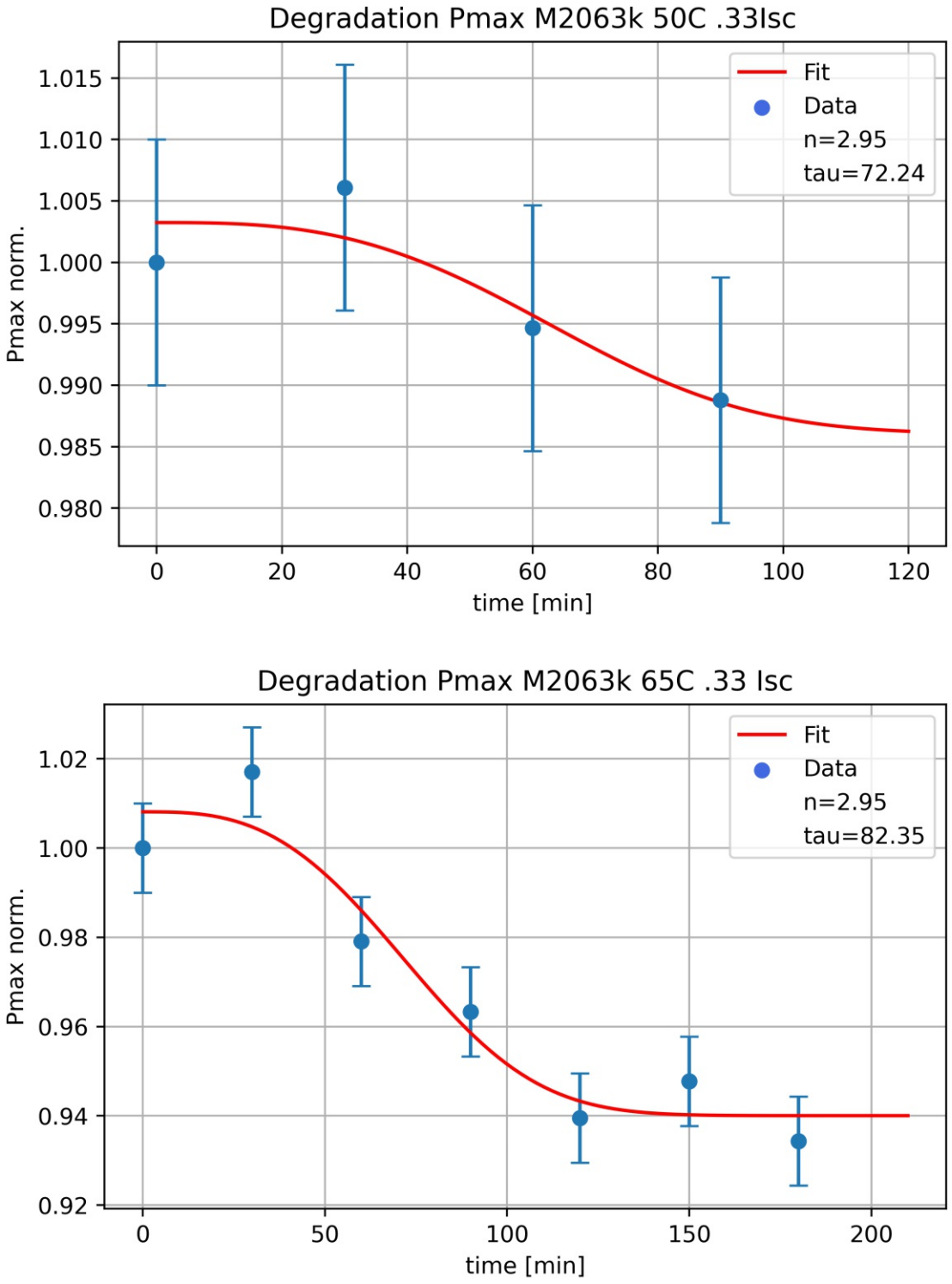

Figure A.19: Sample M2063k JMAK fits

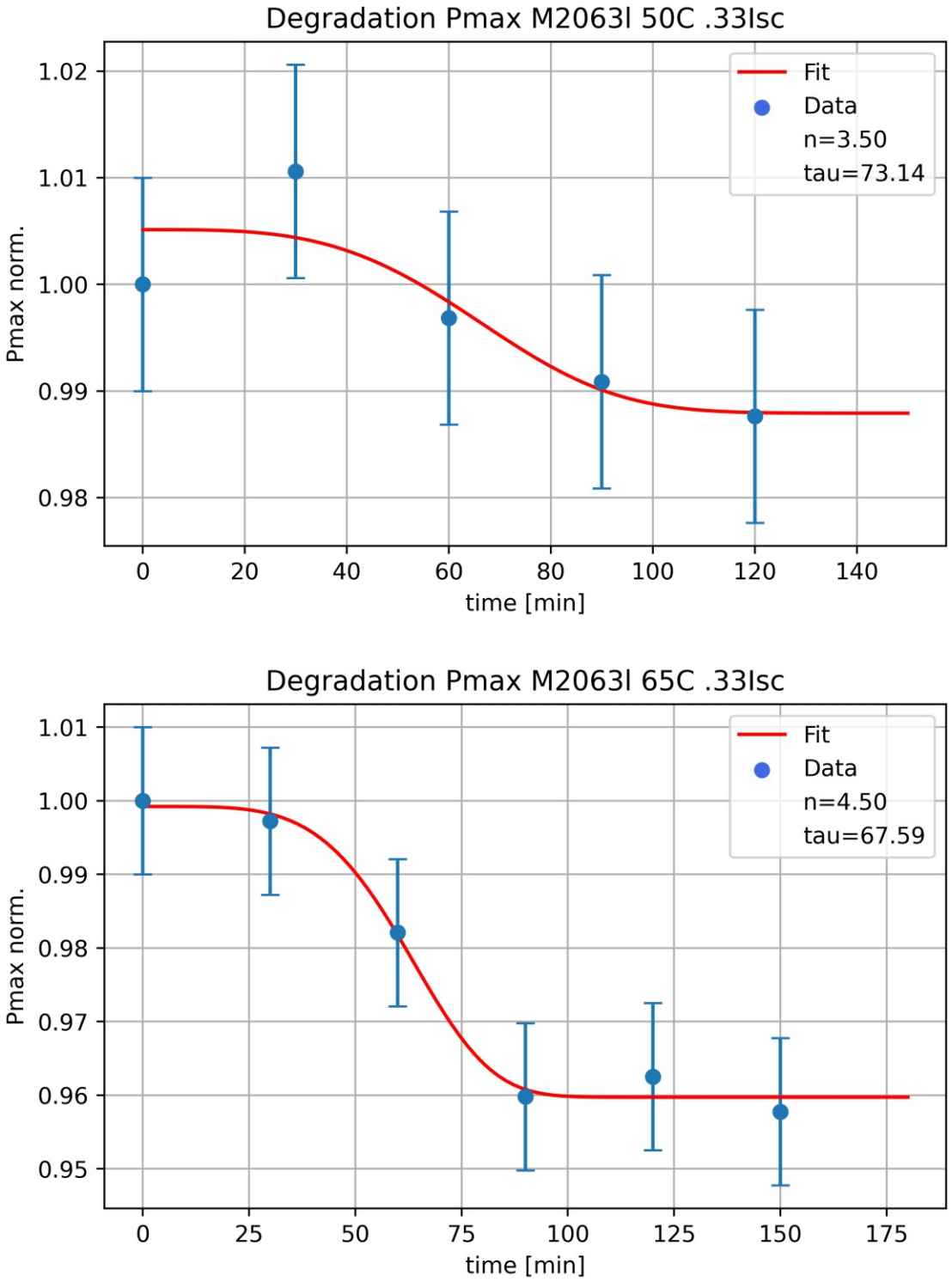

Figure A.20: Sample M2063l JMAK fits

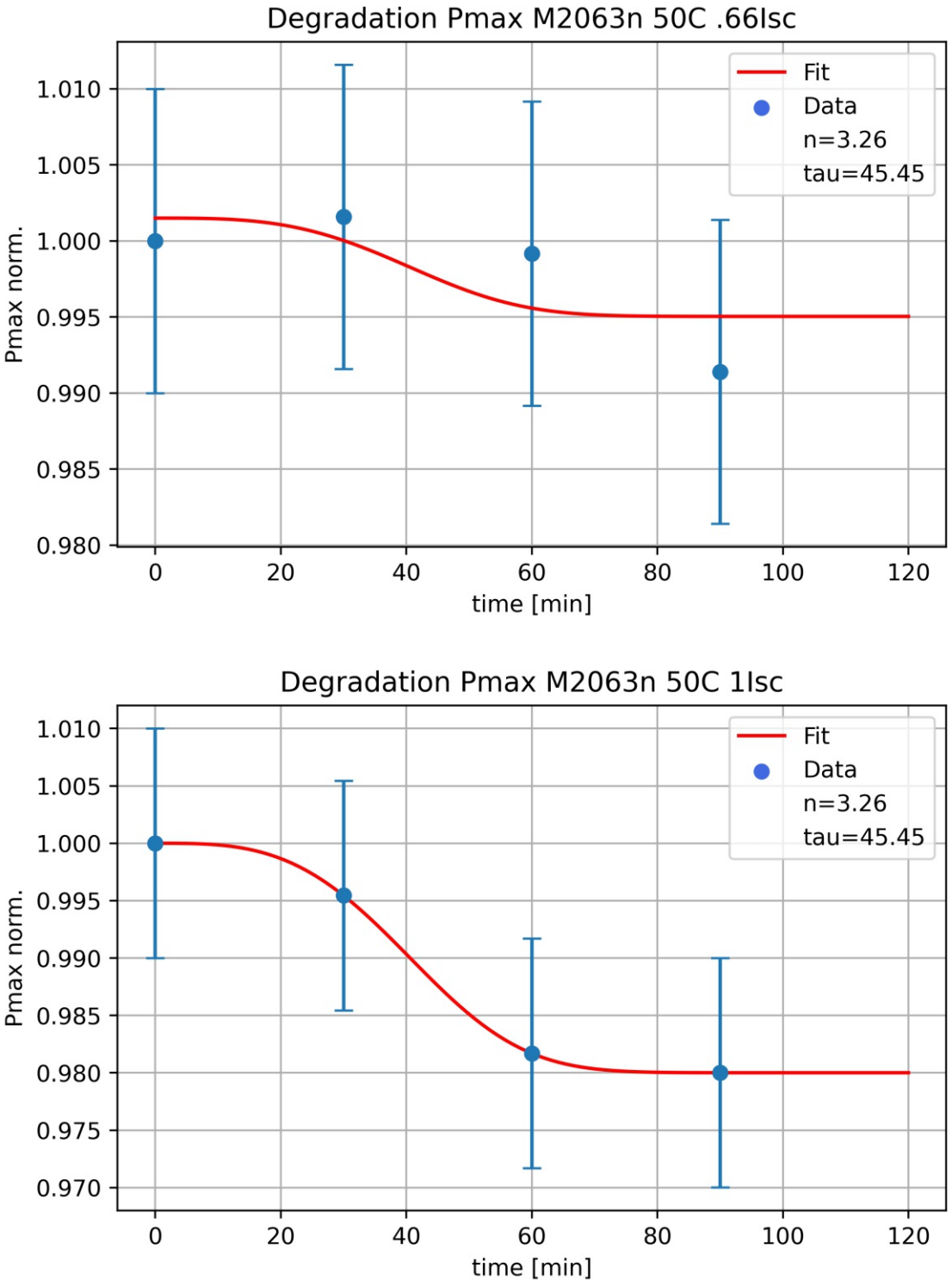

Figure A.21: Sample M2063n JMAK fits

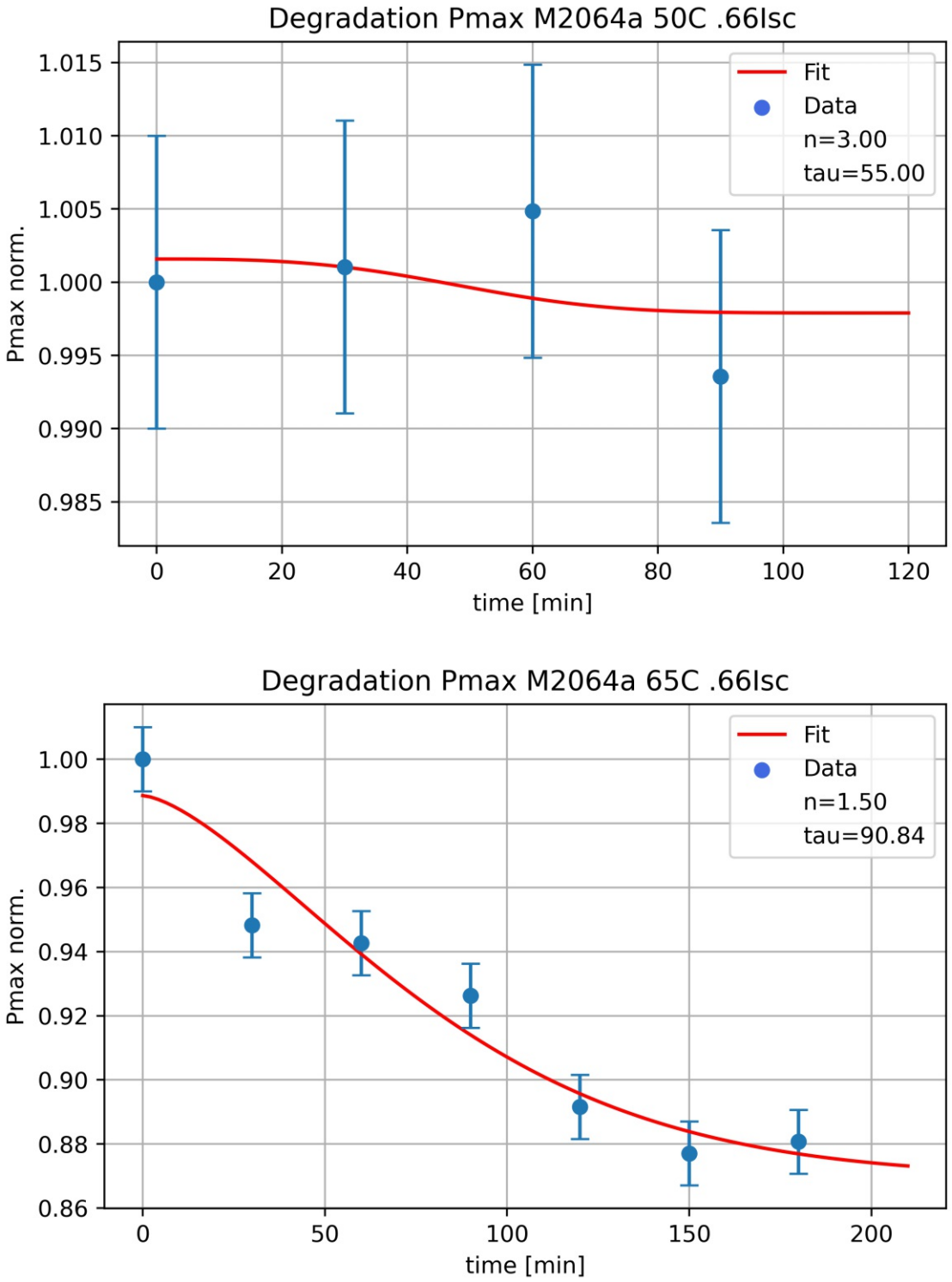

Figure A.22: Sample M2064a JMAK fits

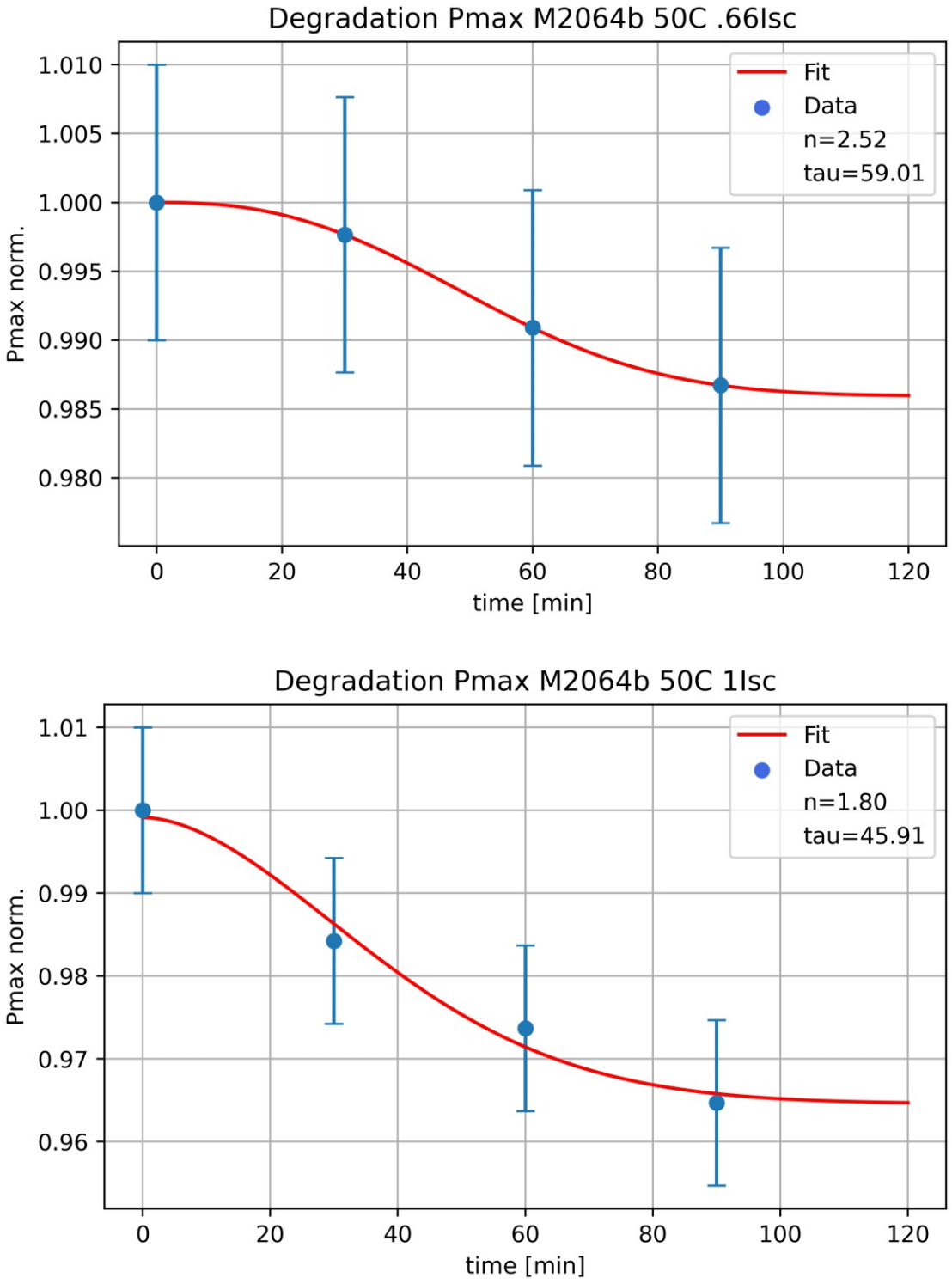

Figure A.23: Sample M2064b JMAK fits

B CIGS and c-Si data

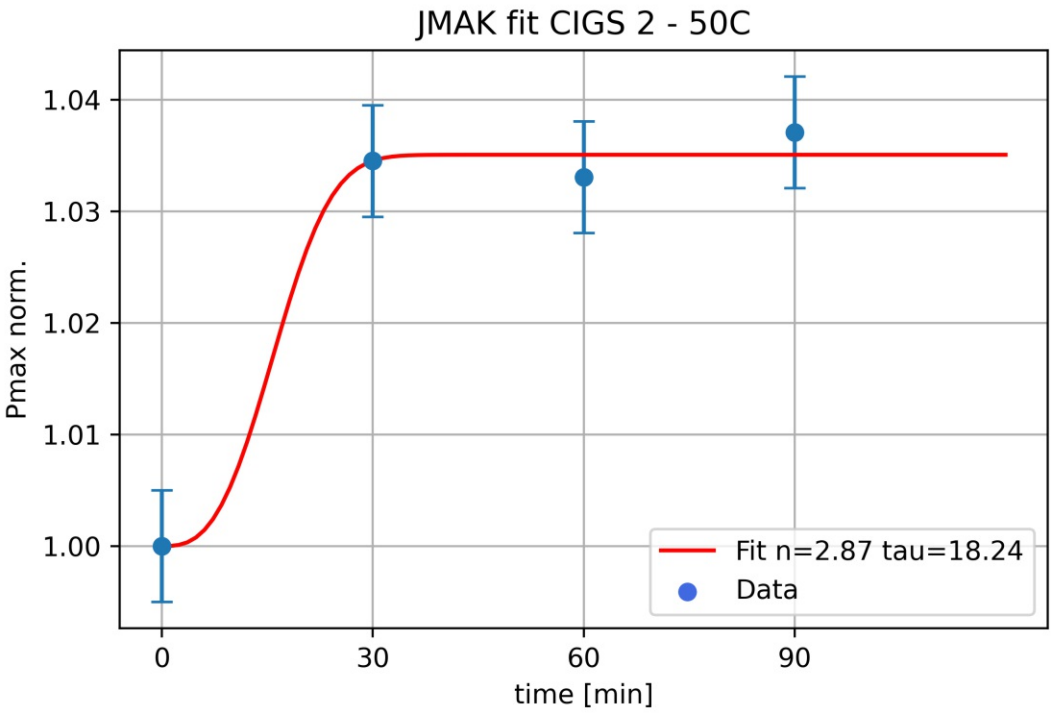

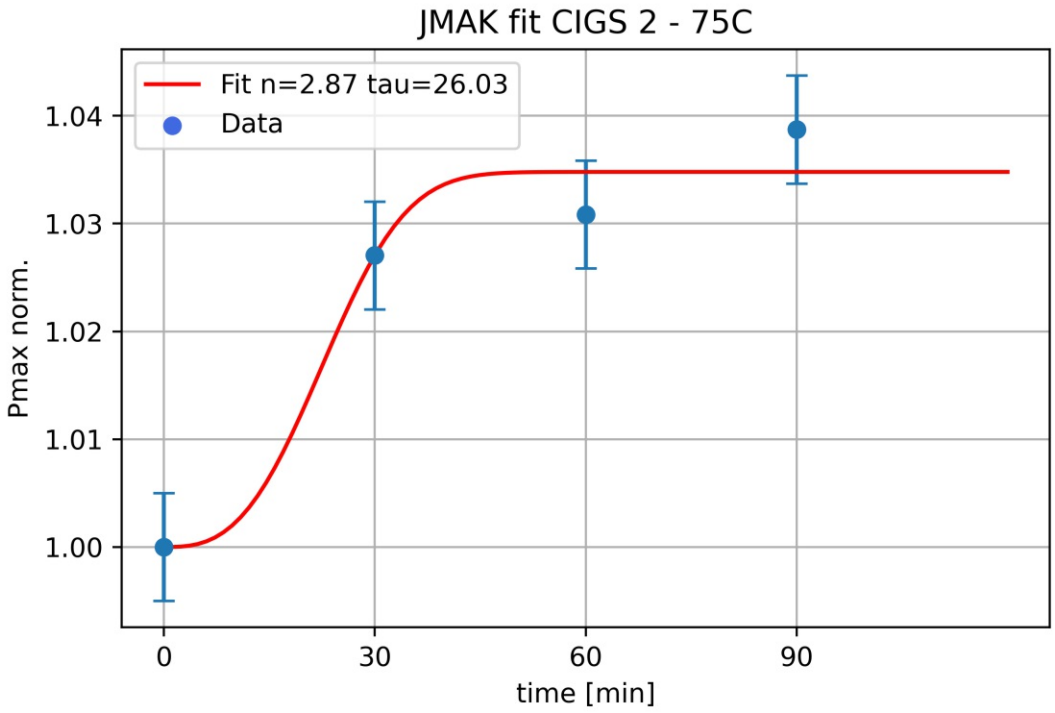

Figure B.1: Sample CIGS 2 JMAK fits

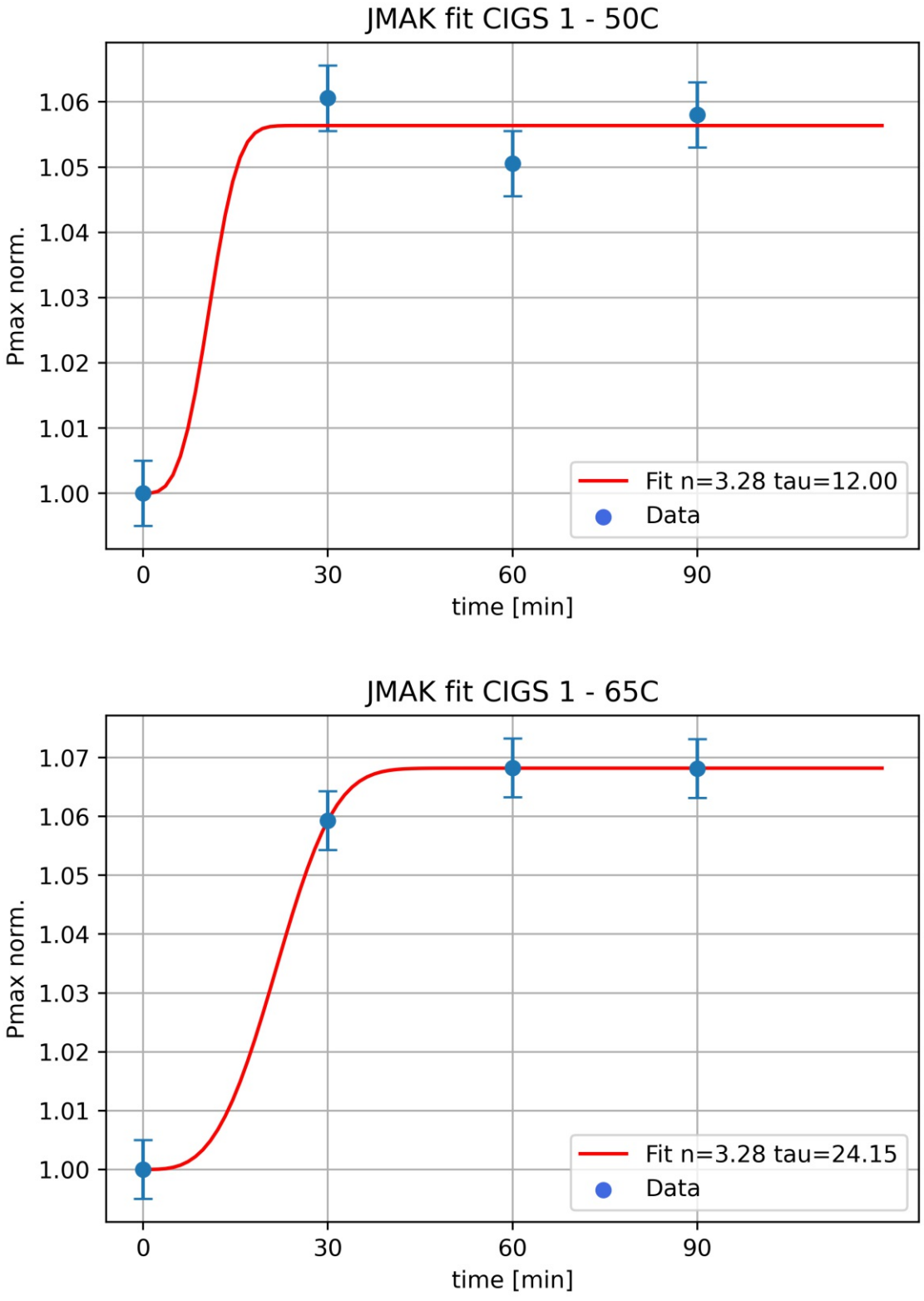

Figure B.2: Sample CIGS 1 JMAK fits 50°C, 65°C

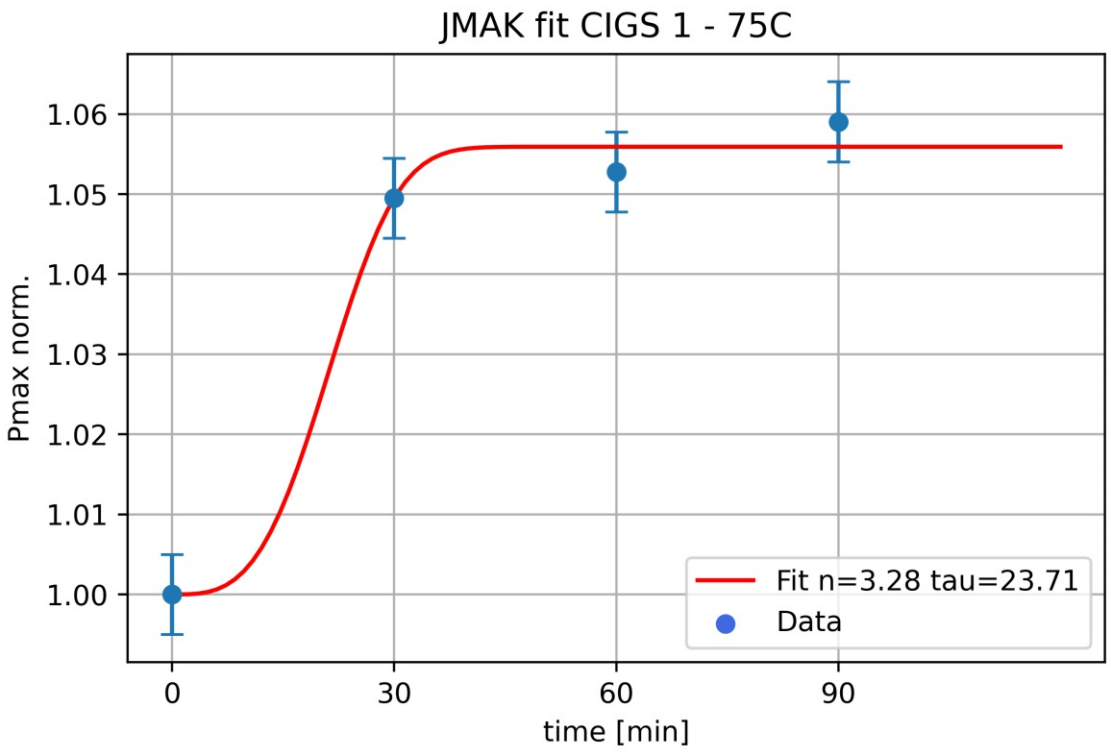

Figure B.3: Sample CIGS 1 JMAK fits 75°C